

Application Number: 45054
Plan Revision: December 2025



CLASS VI PERMIT APPLICATION NARRATIVE

LAC 43:XVII.3607.C and 40 CFR 146.82(a)

RIVER PARISH SEQUESTRATION PROJECT – RPN 1



December 2025

JOSEPH E. MIZERANY

Plan Revision Date: December 2025

TABLE OF CONTENTS

1. PROJECT BACKGROUND AND CONTACT INFORMATION.....	1
1.1 Project Background	1
1.2 Project Description and Location	1
1.3 Sources of CO ₂	2
1.4 Project Goals.....	3
1.5 Partners/Collaborators	3
1.6 Project Timeframe	3
1.7 Proposed Injection Mass/Volume and CO ₂ Sources	4
1.8 Waiver/Exemption.....	4
1.9 State Contact.....	4
2. SITE CHARACTERIZATION.....	5
2.1 Regional Geology, Hydrogeology, and Local Structural Geology [LAC 43:XVII.3607.C.1.b.i and 40 CFR 146.82(a)(3)(vi)].....	5
2.1.1 Regional Geology	5
2.1.2 Geologic History.....	6
2.1.3 Structural Geology	6
2.1.4 Regional Hydrogeology	7
2.2 Maps and Cross Sections of the AoR [LAC 43:XVII.3607.C.1 and LAC 43:XVII.3607.C.1.b.ii / 40 CFR 146.82(a)(2), 146.82(a)(3)(i)]	8
2.2.1 RPS Storage Site Map.....	8
2.2.2 Sources of Subsurface Data and Methodology	8
2.2.3 RPS Regional Structural Maps	11
2.2.4 RPS Regional Thickness Maps.....	11
2.2.5 Spatial Relationships.....	12
2.2.6 Lateral Continuity of Formations.....	13
2.3 Faults and Fractures [LAC 43:XVII.3607.C.1.b.iii and 40 CFR 146.82(a)(3)(ii)]	15
2.3.1 Regional Faulting.....	15
2.3.2 AoR Investigation	15
2.3.3 Regional Implications on Fluid Flow	20
2.3.4 Addressing Uncertainties	21
2.4 Injection and Confining Zone Details [LAC 43:XVII.3607.C.2.a and 40 CFR 146.82(a)(3)(iii)]	23
2.4.1 Depth, Aerial Extent, and Thickness	23
2.4.2 Porosity, Permeability, and Capillary Pressure.....	24
2.4.3 Mineralogy and Petrology.....	31

2.4.4	Storage Capacity, Injectivity, and Integrity	36
2.4.5	Additional Data Collection	37
2.5	Geomechanical and Petrophysical Information [LAC 43:XVII.3607.C.2.b and 40 CFR 146.82(a)(3)(iv)].....	38
2.5.1	Geomechanical and Petrophysical Characteristics of the Confining Zone.....	38
2.5.2	Average Rock Strength.....	38
2.5.3	Average Ductility.....	42
2.5.4	Fractures.....	43
2.5.5	In-situ Stress Field	43
2.5.6	Average Pore Pressure	45
2.5.7	Addressing Geomechanical Uncertainties	46
2.6	Seismic History [LAC 43:XVII.3607.C.2.c and 40 CFR 146.82(a)(3)(v)].....	46
2.6.1	Historical Seismicity Review.....	46
2.6.2	Seismic Sources	47
2.6.3	Seismic Risk.....	47
2.6.4	Seismicity Mitigation.....	48
2.7	Hydrologic and Hydrogeologic Information [LAC 43:XVII.3607.C.1.b.i and 40 CFR 146.82(a)(3)(vi), 146.82(a)(5)].....	48
2.7.1	Regional Hydrogeology	48
2.7.2	Mississippi River Alluvial Aquifer.....	48
2.7.3	Chicot Equivalent Aquifer System	49
2.7.4	Surface Water Bodies	51
2.7.5	USDW Water Chemistry	51
2.7.6	Injection Zone Water Chemistry.....	51
2.7.7	Additional Hydrologic Data Collection	52
2.8	Geochemistry [LAC 43:XVII.3607.C.2.e and 40 CFR 146.82(a)(6)].....	52
2.8.1	Geochemical Characterization Summary	52
2.8.2	Geochemical Modeling Setup.....	56
2.8.3	Geochemical Modeling Results and Discussion.....	62
2.9	Other Information (Including Surface Air and/or Soil Gas Data, if Applicable)	73
2.10	Site Suitability [LAC 43:XVII.3615 and 40 CFR 146.83].....	73
2.10.1	Distribution of Lithological Facies	73
2.10.2	Sealing Capacity and Integrity of the Confining Zone	74
2.10.3	Geochemical Reactions.....	75
2.10.4	Storage Capacity and Injectivity of the Injection Zone	76
2.10.5	Secondary Confinement.....	78

3.	AREA OF REVIEW AND CORRECTIVE ACTION	79
4.	FINANCIAL RESPONSIBILITY	80
5.	INJECTION WELL CONSTRUCTION	81
5.1	Introduction	81
5.2	Engineering Design	81
5.3	Construction Procedures [LAC 43:XVII.3607.C.2.k and 40 CFR 146.82(a)(12)]	82
5.4	Discussion of Injection Well Design	83
5.4.1	Drive Pipe	84
5.4.2	Surface Casing	84
5.4.3	Production Casing	85
5.4.4	Centralizers	86
5.4.5	Injection Tubing	87
5.4.6	Top Liner Packer and PBR Discussion	87
5.4.7	Subsurface Safety Valve	87
5.5	Testing and Logging During Drilling and Completion Operations	88
5.5.1	Coring Plan	88
5.5.2	Logging Plan	88
5.5.3	Formation Fluid Testing	88
5.5.4	Step-Rate Injectivity Test	88
5.6	Proposed Stimulation Program [LAC 43:XVII.3607.C.2.h and 40 CFR 146.82(a)(9)]	88
6.	PRE-OPERATIONAL LOGGING AND TESTING	89
7.	WELL OPERATION	90
7.1	Operational Procedures [LAC 43:XVII.3607.C.2.j and 40 CFR 146.82(a)(10)]	90
7.2	Proposed Carbon Dioxide Stream [LAC 43:XVII.3607.C.2.f.iii and 3607.C.2.f.iv, and 40 CFR 146.82(a)(7)(iii) and (iv)]	92
8.	TESTING AND MONITORING	94
9.	INJECTION WELL PLUGGING	95
10.	POST-INJECTION SITE CARE (PISC) AND SITE CLOSURE	96
11.	EMERGENCY AND REMEDIAL RESPONSE	97
12.	INJECTION DEPTH WAIVER AND AQUIFER EXEMPTION EXPANSION	98

13. OPTIONAL ADDITIONAL PROJECT INFORMATION [LAC 43:XVII Subpart 1-6 and 40 CFR 144.4]	99
14. OTHER INFORMATION	100
14.1 Environmental Justice Assessment.....	100
14.1.1 Analysis of Communities.....	100
14.1.2 Project Benefits and Impacts	100
14.2 Recordkeeping	102

FIGURES

- Figure 1.2-1: RPS Storage Fairways
- Figure 1.2-2: Map of the Area
- Figure 1.5-1: RPS Project Schedule
- Figure 1.5-2: RPS Project Storage Build-Up
- Figure 1.8-1: State Owned Lands in RPS Project Area Underlying LA-943 and LA-944
- Figure 1.8-2: State Owned Lands in RPS Project Area Underlying Grand Bayou
- Figure 2.1-1: Site Stratigraphic Column
- Figure 2.1-2: Paleogeographic Map
- Figure 2.1-3: Environment of Deposition Diagram
- Figure 2.1-4: Tectonic Map
- Figure 2.1-5: Regional Fault Map
- Figure 2.1-6: Gross Injection Zone Isopach
- Figure 2.1-7: Interpreted Faults in the Vicinity of RPS North Fairway
- Figure 2.1-8: Areal Extent of the Mississippi River Alluvial Aquifer and Chicot Equivalent Aquifer System
- Figure 2.2-1: Modeled CO₂ Plume Extents
- Figure 2.2-2: Area of Review Around RPN-1
- Figure 2.2-2b: Topographic Map of the Proposed Sequestration Site
- Figure 2.2-3: Map of the RPS Storage Site with Existing Wells and Seismic Data
- Figure 2.2-4: Map of Smoke Bend 3D Seismic Acquisition
- Figure 2.2-5: 3D Structural Framework
- Figure 2.2-6: Geobody Extraction
- Figure 2.2-7: 3D Geocellular Grid
- Figure 2.2-8: Depth Structure Map of the Top of the Upper Confining Zone

- Figure 2.2-9: Depth Structure Map of the Top of the Upper Injection Zone
Figure 2.2-10: Depth Structure Map of the Top of the Basal Confining Zone
Figure 2.2-11: Depth Structure Map of the Top of the 2nd Upper Confinement 1
Figure 2.2-12: Depth Structure Map of the Top of the 2nd Upper Confinement 2
Figure 2.2-13: North-South Regional Geology
Figure 2.2-14: East-West Regional Geology
Figure 2.2-15: North-South RPN Geology
Figure 2.2-16: East-West RPN Geology
Figure 2.2-17: Hydrogeologic Cross Section North to South
Figure 2.2-18: Hydrogeologic Cross Section West to East
Figure 2.2-19: Above Primary Confinement Gross Isopach
Figure 2.2-20: Primary Confinement Isopach
Figure 2.2-21: Secondary Upper Confining Layer 1 Isopach
Figure 2.2-22: Secondary Upper Confining Layer 2 Isopach
Figure 2.2-23: Basal Confining Layer
Figure 2.2-24: 3D Fault Map
Figure 2.2-25: Zoom Interpreted Faults in Vicinity of RPS North Fairway
Figure 2.2-26: Depth Structure Map of Base of the USDW
Figure 2.2-27: Injection Zone True Stratigraphic Thickness
Figure 2.2-28: Injection Zone True Vertical Thickness
Figure 2.2-29: Regional Geologic Model North-South
Figure 2.2-30: Regional Geologic Model West-East
Figure 2.2-31: Seismic Cross-Section North-South
Figure 2.2-32: Seismic Cross-Section West-East
Figure 2.3-1: Fault Slip Potential Example
Figure 2.4-1: Injection Zone Depth Structure Maps
Figure 2.4-2: Confining Zone Depth Structure Maps
Figure 2.4-3: Confining Zone True Vertical Thickness Maps
Figure 2.4-4: Confining Zone True Stratigraphic Thickness Maps
Figure 2.4-5: Petrophysical Model Output
Figure 2.4-6: Key Injection Zone Average Porosity Maps at RPN-1
Figure 2.4-7: Key Injection Zone Median Permeability Maps at RPN-1

- Figure 2.4-9: Key Confining Zone Average Porosity Maps at RPN-1
- Figure 2.4-10: Key Confining Zone Median Permeability Maps at RPN-1
- Figure 2.4-11: Mercury Injection Capillary Pressure from Core
- Figure 2.4-12: Mercury Injection Capillary Pressure from RSWC
- Figure 2.4-13: Pore Size Distribution from Core
- Figure 2.4-14: Pore Size Distribution from RSWC
- Figure 2.4-15: Injection Zone Net-to-Gross Maps
- Figure 2.4-16: Confining Zones Net-to-Gross Maps
- Figure 2.4-17: Palo Alto RPN-S #1 Cored Intervals
- Figure 2.4-18: Regional Core and Cutting Samples
- Figure 2.4-19: Injection Zone Sandstone Classification QFR Ternary Diagram
- Figure 2.5-1: Palo Alto RPN-S #1 Unconfined Compressive Stress
- Figure 2.5-2: Palo Alto RPN-S #1 Stress Field
- Figure 2.5-3: Palo Alto RPN-S #1 Fracture Gradient
- Figure 2.5-4: Depth Contour Map of Base of Pressure Transition Zone
- Figure 2.5-5: Bayou Sorrel Field Pressure Transition
- Figure 2.6-1: Historic Seismicity in the RPS Project Area
- Figure 2.6-2: Risk Assessment Characterizing Intensity of a Potential Earthquake
- Figure 2.6-3: Expected Number of Occurrences of Damaging Earthquake
- Figure 2.6-4: Modified Mercalli Intensity Scale
- Figure 2.7-1: Wells with Groundwater Chemistry Analyses
- Figure 2.7-2: Depth to Top of Mississippi River Alluvial Aquifer
- Figure 2.7-3: Recharge Area for Mississippi River Alluvial Aquifer
- Figure 2.7-4: Potentiometric Contour Map of the Mississippi River Alluvial Aquifer
- Figure 2.7-5: Primary Aquifers in Ascension Parish
- Figure 2.7-6: Depth to Top of Norco Aquifer
- Figure 2.7-7: Depth to Top of Gonzalez-New Orleans Aquifer
- Figure 2.7-8: Depth to Top of 1,200-Foot Sand Aquifer
- Figure 2.7-9: Recharge Area for Chicot Equivalent Aquifer System
- Figure 2.7-10: Potentiometric Contour Map of the Chicot Equivalent Aquifer System
- Figure 2.7-11: RPN-1 Groundwater USDW Sampling
- Figure 2.8-1: Injection Zone Formation Water Piper Diagrams

- Figure 2.8-2: Injection Zone Formation Water Stiff Diagrams
- Figure 2.8-3: Reaction Pathway Modeling-Confining Unit Mineral Masses
- Figure 2.8-4: Reaction Pathway Modeling- Confining Unit Porosity and Total Mineral Masses
- Figure 2.8-5: Reaction Pathway Modeling- Confining Unit Formation Water pH
- Figure 2.8-6: Reaction Pathway Modeling- Injection Zone (Sandy Lithology, Shallow Conditions) Mineral Masses
- Figure 2.8-7: Reaction Pathway Modeling- Injection Zone (Sandy Lithology, Shallow Conditions) Porosity and Mineral Mass
- Figure 2.8-8: Reaction Pathway Modeling- Injection Zone (Sandy Lithology, Shallow Conditions) Formation Water pH
- Figure 2.8-9: Reaction Pathway Modeling- Injection Zone (Shaley Lithology, Shallow Conditions) Mineral Masses
- Figure 2.8-10: Reaction Pathway Modeling- Injection Zone (Shaley Lithology, Shallow Conditions) Porosity and Mineral Mass
- Figure 2.8-11: Reaction Pathway Modeling- Injection Zone (Shaley Lithology, Shallow Conditions) Formation Water pH
- Figure 2.8-12: Reaction Pathway Modeling- Injection Zone (Sandy Lithology, Deep Conditions) Mineral Masses
- Figure 2.8-13: Reaction Pathway Modeling- Injection Zone (Sandy Lithology, Deep Conditions) Porosity and Mineral Mass
- Figure 2.8-14: Reaction Pathway Modeling- Injection Zone (Sandy Lithology, Deep Conditions) Formation Water pH
- Figure 2.8-15: Reaction Pathway Modeling- Injection Zone (Shaley Lithology, Deep Conditions) Mineral Masses
- Figure 2.8-16: Reaction Pathway Modeling- Injection Zone (Shaley Lithology, Deep Conditions) Porosity and Mineral Mass
- Figure 2.8-17: Reaction Pathway Modeling- Injection Zone (Shaley Lithology, Deep Conditions) Formation Water pH
- Figure 5.4-1: Modeled RPN-1-INJ Injection Profile
- Figure 7.1-1: Operation Completion Strategy Schematic
- Figure 14.1-1: Census Tracts Near RPS

TABLES

- Table 2.1-1: Well Inventory Summary
- Table 2.1-2: Fault Inventory Summary
- Table 2.2-1: Wireline Logging and Sampling Program for the Palo Alto RPN-S #1
- Table 2.2-2: 2D Seismic Lines for RPS Project Site Characterization
- Table 2.2-3: 3D Seismic Surveys for RPS Project Site Characterization
- Table 2.2-4: RP North Fairway Synthetic Well Ties
- Table 2.2-5: Wells and Formation Tops in GeoModel
- Table 2.2-6: Relative Horizontal Distance of Domes to RP North Injection Wells
- Table 2.2-7: Summary of Top of Injection to Lowermost USDW
- Table 2.2-8: Average Depth and Gross Thickness of the RPN-1 Injection Units
- Table 2.4-1: Average Depth and Gross Thickness of the RPN-1 Confining Units
- Table 2.4-2: Wells RPS Performed Petrophysical Analysis
- Table 2.4-3: Wells with Triple Combo Logs
- Table 2.4-4: Wells with Spontaneous Potential and Deep Resistivity Logs
- Table 2.4-5: Wells with Clipped Deep Resistivity Logs
- Table 2.4-6: Wells with Bulk Shifted Deep Resistivity Logs
- Table 2.4-7: Injection Zone Average Porosity and Permeability
- Table 2.4-8: Confining Zones Average Porosity and Permeability
- Table 2.4-9: Capillary Pressure Summary
- Table 2.4-10: Threshold Entry Pressure Testing Summary
- Table 2.4-11: Injection Zone Mineralogy
- Table 2.4-12: Principal Confining Unit Mineralogy
- Table 2.4-13: Quartz, Feldspar, and Rock Fragments
- Table 2.4-14: Gamero-Diaz Shale Classification
- Table 2.4-15: Mineralogy Table
- Table 2.5-1: MDT Pressure Samples
- Table 2.5-2: Mini Frac Summary
- Table 2.5-3: Palo Alto RPN-S 1 Wireline Derived RM Properties
- Table 2.5-4: Core Rock Mechanics
- Table 2.5-5: Calculated Average UCS and Brittleness Index of the Primary Confining Zone
- Table 2.6-1: Location, Depth, and Magnitude of Southeast Louisiana Seismic Events

- Table 2.7-1: Groundwater Sample Wells in Ascension Parish
- Table 2.7-2: Summary of Water-Quality Characteristics for Groundwater
- Table 2.7-3: Summary of Water Quality Data
- Table 2.7-4: Summary of Laboratory Analytical Results for Inorganics
- Table 2.7-5: Aqueous Geochemistry
- Table 2.7-6: RPN-1 Groundwater USDW Sampling
- Table 2.8-1: Mineralogy Model Input
- Table 2.8-2: Aqueous Model Input
- Table 2.8-3: Aqueous Model Input—Primary Confining Unit
- Table 2.8-4: Additional Model Input Considerations
- Table 2.8-5: Kinetic Sensitivity Results Summary
- Table 2.8-6: Equilibrium Model Aqueous Changes
- Table 2.8-7: Equilibrium Modeling Results—Primary Confining Unit Base Case
- Table 2.8-8: Equilibrium Modeling Results—Injection Zone Shallow Sand Base Case
- Table 2.8-9: Equilibrium Modeling Results—Injection Zone Shallow Shale Base Case
- Table 2.8-10: Equilibrium Modeling Results—Injection Zone Deep Sand Base Case
- Table 2.8-11: Equilibrium Modeling Results—Injection Zone Deep Shale Base Case
- Table 2.8-12: Equilibrium Modeling Results—Primary Confining Unit Sensitivity Case
- Table 2.8-13: Equilibrium Modeling Results—Injection Zone Shallow Sand Sensitivity Case
- Table 2.8-14: Equilibrium Modeling Results—Injection Zone Shallow Shale Sensitivity Case
- Table 2.8-15: Equilibrium Modeling Results—Injection Zone Deep Sand Sensitivity Case
- Table 2.8-16: Equilibrium Modeling Results—Injection Zone Deep Shale Sensitivity Case
- Table 7-1: Proposed Operational Procedures
- Table 7.1-1: Injection Pressure by Stage
- Table 7.1-2: Injection Intervals
- Table 7.1-3: Injection Ramp-Up Schedule for RPN-1-INJ
- Table 7.2-1: Summary of Minimum CO₂ Purity Requirements
- Table 7.2-2: CO₂ Streams Blended in the Promax Model
- Table 7.2-3: Mixed Gas Composition
- Table 13-1: Permits/Authorizations Required for the Class VI Injection Well
- Table 14.1-1: Demographic and DOE Burden Indicator Data for the Three Census Tracts

Application Number: 45054
Plan Revision: December 2025

APPENDICES

Appendix 2A: Structural Framework and Property Modeling

Appendix 2B: Fault Stability Assessment

Appendix 2D: Chemical Solids Data

Appendix 2E: RPN-1 USDW Groundwater Sampling Study

Appendix 2F: Grain Density Data

Appendix 2G: Predicted Geochemical Reactions Following Injectate Gas Interaction

Appendix 5A: Engineering Calculations – Cement Volume Details

ACRONYMS AND ABBREVIATIONS

2D	two-dimensional
3D	three-dimensional
AoR	Area of Review
BHP	bottomhole injection pressure
BRI	brittleness index
C&E	Louisiana Department of Conservation & Energy
CCS	carbon capture and storage
CO ₂	carbon dioxide
DOE	Department of Energy
EJ	Environmental Justice
EPA	Environmental Protection Agency
FSP	Fault Slip Potential
gm/cm ³	gram(s) per cubic centimeter
kg	kilogram(s)
lb/ft ³	pound(s) per cubic foot
LDENR	Louisiana Department of Energy and Natural Resources
LLNL	Lawrence Livermore National Laboratory
LSU	Louisiana State University
Marg. 'A'	Marginulina ascensionensis
mg/L	milligrams per liter
MMtpa	million metric tons per annum
MMt	million metric tons
NGVD 29	National Geodetic Vertical Datum of 1929
OD	outer diameter
PBR	polished bore receptacle
PISC	Post-Injection Site Care
psi	pound(s) per square inch
psig	pound(s) per square inch gauge
QC	quality control
RPCC	River Parishes Community College
RPS	River Parish Sequestration, LLC

Application Number: 45054
Plan Revision: December 2025

SONRIS	Strategic Online Natural Resource Information System
SP	spontaneous potential
TDS	total dissolved solids
TVDSS	true vertical depth sub sea
TVD	true vertical depth
TWT	two-way time
UIC	Underground Injection Control
UCS	unconfined compressive strength
USDW	underground source(s) of drinking water
USGS	United States Geological Survey
Vclay	clay volume

1. **PROJECT BACKGROUND AND CONTACT INFORMATION**

1.1 **Project Background**

This application is for an Underground Injection Control (UIC) Class VI Authorization to Construct for carbon dioxide (CO₂) injection well RPN-1-INJ, one of the seven injection wells in the River Parish Sequestration Project (RPS Project). The RPS Project includes aboveground facilities and CO₂ transportation infrastructure outside of the purview of the program. The application also includes the following attachments with additional detail, which are based on templates provided by the U.S. Environmental Protection Agency (EPA):

Attachment A	Summary of Requirements
Attachment B	Area of Review and Corrective Action Plan
Attachment C	Financial Responsibility Demonstration
Attachment D	Construction Details
Attachment E	Pre-Operational Well Testing Plan
Attachment F	Testing and Monitoring Plan (includes the Quality Assurance and Surveillance Plan)
Attachment G	Injection Well Plugging Plan
Attachment H	Post-Injection Site Care (PISC) and Site Closure Plan (includes Alternative PISC Demonstration)
Attachment I	Emergency and Remedial Response Plan
Attachment J	Stimulation Plan

1.2 **Project Description and Location**

The RPS Project includes seven Class VI injection wells, each capable of injecting 2 million metric tons per annum (MMtpa) of CO₂ for a total annual CO₂ injection capability of 14 MMtpa. When fully constructed, the RPS Project can store 380 million metric tons (MMt) of CO₂ utilizing seven Class VI wells.

The RPS Project is located on the west side of the Mississippi River near Donaldsonville, Louisiana, spread over approximately 30,000 acres of land (RPS Storage Site). The RPS Project includes two distinct storage fairways (storage sites) and the connecting pipelines:

- The RPS North Fairway is located near Donaldsonville, Louisiana, and includes five injection wells (RPN-1-INJ, RPN-2-INJ, RPN-3-INJ, RPN-4-INJ, and RPN-5-INJ).
- The RPS South Fairway Storage Site is located 5 miles south of the North Fairway near Napoleonville, Louisiana, and includes two injection wells (RPS-1-INJ and RPS-2-INJ).

Application Number: 45054
Plan Revision: December 2025

The RPS Project's major project components are depicted on **Figure 1.2-1**. This permit application is specific to RPN-1-INJ, the first injection well in the North Fairway. All the North Fairway wells are included in the simulation model to consider the influence of offset injection. However, the Area of Review (AoR) of this permit application is specific to RPN-1-INJ (**Figure 1.2-2**).

1.3 Sources of CO₂

RPS is developing a CO₂ storage hub in the Louisiana Chemical Corridor between Baton Rouge and New Orleans in Ascension, Assumption, and Iberville Parishes (RPS North Fairway). Currently, there are 15 MMtpa of CO₂ emissions within 10 miles of the RPS Storage Site and 60 MMtpa within 50 miles of the RPS Storage Sites from over 50 industrial emitters seeking to decarbonize their emissions. This industrial corridor is one of the most concentrated clusters of existing industrial emissions (CO₂ per square mile) in America. RPS's commercial model will provide these emitters and suppliers of CO₂ with a long-term, contracted CO₂ transportation and storage service. Under this service, RPS will receive the CO₂ in one of two ways:

1. The emitter or CO₂ source will deliver CO₂ to its plant gate, where RPS will receive and transport the CO₂ using planned pipeline infrastructure to the RPS Storage Site.
2. A supplier of CO₂ will deliver CO₂ that has been captured and processed at an emitter's facility into RPS's pipeline system.

Once at the RPS Storage Site, the CO₂ will be injected into saline reservoirs deep beneath the ground surface (~4,500 to ~12,000 feet in depth) for permanent geologic storage.

RPS signed a binding CO₂ Offtake and Storage Agreement (COSA) with ExxonMobil Low Carbon Solutions Onshore Storage LLC (ExxonMobil) whereby RPS is obligated to transport and sequester at least 850,000 metric tons and up to 4,000,000 metric tons of Captured CO₂ per year supplied by ExxonMobil.

In the North Fairway, injection wells RPN-1-INJ, RPN-2-INJ, and RPN-3-INJ are nearest to the expected CO₂ sources in the Geismar and Donaldsonville, Louisiana areas. The initial phase of CO₂ injection is planned for these three wells. RPN-4-INJ and RPN-5-INJ are farther from emissions sources, and these wells would be constructed and used when, and if, excess capacity beyond the initial three wells is needed. However, this anticipated order of injection could change based on the timing of emitter demand for injection capacity.

Similarly, the injection locations in the South Fairway, RPS-1-INJ and RPS-2-INJ, are well situated to provide a storage solution for CO₂ sources farther south along the Mississippi River corridor and provide additional injection capacity if RPS needs to commence more injection volumes simultaneously than the North Fairway can accommodate.

1.4 Project Goals

The goals of the RPS Project are to (1) provide industrial emitters with a timely, reliable, cost-competitive, and scalable CO₂ transportation and storage service; (2) minimize negative impacts to communities and environmental resources; and (3) generate positive impacts for communities in the project area. The RPS Project is ideally situated to achieve these objectives given the RPS Project's location, large-scale storage capacity, and proximity to existing CO₂ sources to minimize new-build CO₂ pipeline infrastructure.

1.5 Partners/Collaborators

In September 2024, RPS executed an Assistance Agreement with the Department of Energy for a grant available under the DOE's CarbonSAFE Program for Phase III projects (DE-FOA-0002711) (Phase III Grant). Grant funding under the CarbonSAFE program will accelerate characterization and development activities, including drilling an additional stratigraphic test well and conducting additional 3D (three-dimensional) seismic surveys.

In connection with the Phase III Grant, RPS is implementing a Community Benefits Plan, which includes the following:

- Community engagement that includes conducting small group meetings, larger community forums, and the establishment of a Community Advisory Panel (CAP) to provide input on the proposed project.
- Collaborating with the River Parishes Community College (RPCC) to provide input on the development of a curriculum to support careers in CCS and energy transition fields as well as supporting classroom education related to these fields.
- The development of a Community Benefits Fund. Under the proposal, RPS would pay into a Community Benefits Fund for each ton of CO₂ injected in the RPS North Fairway. The RPS Community Benefits Fund would in turn invest in projects to benefit local communities in the RPS North Fairway. RPS will establish an Advisory Panel to determine the best way to expend the funds to benefit the local communities.

In October 2024, RPS affiliate RPS Expansion, LLC was selected for a grant available under the DOE's CarbonSAFE Program for Phase II projects (DE-FOA-0002711) (Phase II Grant). If an Assistance Agreement in connection with this selection is finalized, the Phase II Grant will provide funding for supplemental 3D seismic surveys. In connection with the Phase II Grant, if awarded, RPS will implement a Community Benefits Plan in a similar manner to the Phase III grant.

1.6 Project Timeframe

RPS will construct and complete RPN-1-INJ to a Class VI standard. RPS will construct a pipeline from an interconnection point with ExxonMobil's CO₂ pipeline system to support the commencement of CO₂ injection into RPN-1-INJ in 2027. **Figure 1.5-1** depicts the RPS Project schedule.

Figure 1.5-2 shows the expected annual storage build-up for the RPS Project.

Application Number: 45054
Plan Revision: December 2025

1.7 Proposed Injection Mass/Volume and CO₂ Sources

The RPS Project in total proposes to inject 14 million MMtpa (approximately 725 million standard cubic feet per day) across all seven injection wells, and 380 MMt cumulatively (approximately 7.2 trillion standard cubic feet). RPN-1-INJ, the injection well that is the subject of this application, will be constructed to inject 2 MMtpa (103.6 million standard cubic feet per day on average) for 30 years, which would equate to 60 MMt cumulatively (approximately 1.1 trillion standard cubic feet).

As stated in **Section 1.3**, ExxonMobil will initially supply to RPS Captured CO₂.

1.8 Waiver/Exemption

RPS does not request an injection depth waiver or aquifer exemption.

1.9 State Contact

The RPS Project is in the State of Louisiana. The Louisiana UIC program is led by:

UIC Director
617 North Third Street, 8th Floor
Baton Rouge, Louisiana 70802
(225) 342-5569

The Louisiana UIC Program is administered by the Louisiana Department of Conservation & Energy (C&E). Prior to a departmental reorganization and renaming on October 1, 2025, the department was called the Louisiana Department of Natural Resources (LDENR). In this Application, references to C&E include references to the department prior to the renaming and reorganization.

There are no state parks, state wildlife management areas, or other state conservation lands within the RPS North Fairway. There are no tribal or territory lands located in the RPS North Fairway.

The State of Louisiana owns approximately 47 acres in the RPS North Fairway, including approximately 30 acres underlying the roadbeds of LA-943 and LA-944 in Ascension Parish (**Figure 1.8-1**) and approximately 17 acres underlying Grand Bayou in Iberville Parish (**Figure 1.8-2**).

2. SITE CHARACTERIZATION

The following sections provide documentation to fulfill the site characterization requirements of LAC 43:XVII.3607.C.1, LAC 43:XVII.3607.C.1.b, and LAC 43:XVII.3607.C.2.e / 40 CFR 146.82(a)(2), (3), (5), and (6).

2.1 Regional Geology, Hydrogeology, and Local Structural Geology [LAC 43:XVII.3607.C.1.b.i and 40 CFR 146.82(a)(3)(vi)]

The sub-sections below provide narrative descriptions of the regional geology, geologic history, structural geology, and regional hydrogeology relevant to the RPS Project, per the requirements of LAC 43:XVII.3607.C.1.b.i and 40 CFR 146.82(a)(3)(vi).

2.1.1 Regional Geology

The RPS Project targets a Miocene sand-rich sediment fairway in Southeast Louisiana for CO₂ sequestration. This fairway is sourced by the central and eastern axes of the ancestral Mississippi River and the ancestral Tennessee River.¹ The target storage complex consists of stacked successions of deltaic and fluvial sands deposited from the Lower Miocene through the early Pliocene interbedded with shale layers (**Figure 2.1-1**).²

The location of the RPS Project within the sediment fairway translates to excellent continuity of the major sand packages across the RPS Storage Site. The primary upper confining layer is a shale package in the basal Pliocene deposited during a regional transgression marked by the termination of *Buliminella* 1 foram.³ The basal confining layer for the storage complex is the Lower Miocene shale associated with the termination of the *Marginulina ascensionesis* (Marg. ‘A’) fauna and named internally as the Marg. ‘A’ shale. Two secondary confining layers, named internally as Second Upper Confining 1 (2nd_Upper_Conf_1) and Second Upper Confining 2 (2nd_Upper_Conf_2) provide an additional regional seal above the proposed injection zone.

The total injection interval sediment package from the base of the upper confining Pliocene shale to the top of the basal Marg. ‘A’ shale is approximately 6,000 feet thick with an average of 3,100 feet of net injectable sands interbedded with silts, clay, and mudstone within the North Fairway area. The primary confining unit is located approximately 3,850 feet below sea level and ranges in thickness from approximately 350 to greater than 1,000 feet across the RPS North Fairway. The basal confining unit is located approximately 10,500 feet below sea level and ranges in thickness from 150 to 300 feet across the RPS North Fairway. The reservoir and confining units are regionally continuous, as further discussed in **Section 2.2.6**.

¹ Combillas-Bigott, R.I., and Galloway, W.E., “Depositional history and genetic sequence stratigraphic framework of the middle Miocene depositional episode, South Louisiana,” *Gulf Coast Association of Geological Societies Transactions* vol. 52 (2002): pp. 139–150.

² Fillon, R. H., and Lawless, P. N., (2000), “Lower Miocene-Early Pliocene deposystems in the Gulf of Mexico: regional sequence relationships,” *Gulf Coast Association of Geological Societies Transactions* vol. L (2000).

³ Galloway, W. E. et al., “Cenozoic depositional history of the Gulf of Mexico basin,” *AAPG Bulletin* vol. 84, no. 11 (2000): pp. 1743–1774.

2.1.2 Geologic History

The Miocene Epoch was a period of global cooling that coincided with the initiation of permanent glaciation in Antarctica.⁴ The global cooling resulted in more than 50 miles of shoreline advancement during the Miocene in South Louisiana (**Figure 2.1-2**). During the Early Miocene, the RPS North Fairway was located in an offshore, deltaic environment, and, by the Early Pliocene, the RPS North Fairway was located in a terrestrial depositional environment.

Global temperature fluctuations during this time, associated with Milankovitch Cycles as well as other environmental mechanisms, led to cyclical sediment sequences of sand capped by clays deposited during flooding events.⁵ The flooding surfaces capping these depositional sequences are regionally extensive and serve as internal barriers to vertical flow (**Figure 2.1-3**). During the same period, rapid sedimentation and loading of the regionally extensive Jurassic Louann Salt also led to the emergence of the South Louisiana Salt Basin.⁶

The Lower Pliocene transgression was followed by a shift in sediment flux further to the west on the central Mississippi depositional axis, resulting in more condensed, fine-grained deposition in the RPS North Fairway.

The RPS North Fairway is situated in the South Louisiana Salt Basin on the northern edge of the Gulf of Mexico basin, as depicted by the northwestern Gulf of Mexico tectonic map (**Figure 2.1-4**). The Gulf of Mexico basin formed as part of Early-through-Middle Jurassic rifting during the breakup of the supercontinent Pangea and opening of the Gulf of Mexico.⁷ Crustal extension initiated along pre-existing sutures of accreted terrain from the Ouachita orogeny.

During the Callovian (Middle Jurassic), the crust attenuated sufficiently to subside and form a shallow sea. Climatic conditions and shallow, restricted sea water at this time resulted in evaporitic deposition of the Louann Salt. As extension continued, the basin rapidly deepened and clastic sedimentation ensued. This early evaporitic deposition set up the structural framework that would influence the Miocene deposition.

2.1.3 Structural Geology

The dominant faulting style in South Louisiana is eastward striking, southern dipping, normal faults (**Figure 2.1-5**). These faults initiated and propagated because of crustal subsidence and movement of the underlying Jurassic Louann Salt due to differential sediment loading. Maximum fault and salt movement was interpreted to initiate during the Marg. 'A' time in the Lower Miocene, as evidenced locally by the thicker Lower Miocene section north and northwest of the Napoleonville Dome (**Figure 2.1-6**). Additional details for wells used to construct structural grids and thickness maps are presented in **Table 2.1-1**.

⁴ Galloway et al., "Cenozoic depositional history," 2002.

⁵ Fillon and Lawless, "Lower Miocene-Early Pliocene," 2000.

⁶ Worrall, D. M., and Snelson, S., "Evolution of the northern Gulf of Mexico, with emphasis on Cenozoic growth faulting and the role of salt," in Bally, A. W., and Palmer, A. R., eds., *The Geology of North America- An overview: Boulder, Colorado*, volume A (1989): Geological Society of America.

⁷ Pindell, J. and Dewey, J.F., "Permo-Triassic reconstruction of western Pangea and the evolution of the Gulf of Mexico/Caribbean region," *Tectonics* vol. 1, no. 2 (1982): 179–211. DOI: 10.1029/TC001i002p00179.

Antithetic, down-to-the-north normal faults often dip into these main growth faults. Over time, the Louann Salt has migrated up into numerous salt diapirs, often migrating along regional faults, and in some cases migrating nearly to surface.

The formation of these diapirs has resulted in tensional and compressional faulting in radial patterns above the domes and normal faulting in various directions off the flanks of the domes. Syndepositional movement of both the regional faults and the salt diapirs has resulted in thickened sediment packages updip of the salt diapirs and downdip of the growth faults.

The RPS North Fairway sits within the northern portion of the Southern Louisiana Salt Basin, situated between four prominent salt domes and two regional normal fault systems. As shown in **Figure 2.1-5**, the closest regional faults to the RPS North Fairway are the Scott Fault, approximately 5 miles north of the RPS North Fairway,⁸ and the Vacherie Fault, which passes between the RPS North Fairway and RPS South Fairway (McLindon 2020).⁹ RPS has acquired commercially available 2D (two-dimensional) and 3D seismic surveys to map smaller faults in the immediate vicinity of the RPS North Fairway, which may be associated with the regional Scott and Vacherie faults.

RPS conducted the Smoke Bend seismic survey in Q2 2023 that provided additional 2D and 3D seismic coverage across the AoR and surrounding areas to refine the structural framework of the Geomodel and to map any faults in the northern parts of the RPS North Fairway that may not have been identified through previously licensed 2D survey lines. RPS's interpretation of the seismic data from the Smoke Bend survey informed the update of the Geomodel that is the basis of the revised reservoir simulations. Additional details on the identification of minor faults in the vicinity of the RPS North Fairway are provided in **Section 2.3.2**. The closest faults and salt domes to the RPS North Fairway are shown in **Figure 2.1-7** and summarized in **Table 2.1-2**.

2.1.4 Regional Hydrogeology

The RPS Project is in the southeastern Louisiana hydrogeologic system and collocated with two primary groundwater aquifers: The Mississippi River Alluvial Aquifer and the Chicot Equivalent Aquifer System. The areal extent of the Mississippi River Alluvial Aquifer and Chicot Equivalent Aquifer System is shown in **Figure 2.1-8**. The principal Chicot equivalent units include the Gramercy, Norco, Gonzalez-New Orleans, and “1200-Foot Sand” aquifers. Groundwater occurs throughout the multiple interbedded and interconnected alluvial and terrace deposits ranging in age from Holocene to Lower Pleistocene and Upper Pliocene. Deposits generally contain coarser material at the base and fine upward from pea- and cobble-sized gravel (granules 2-4 mm in size) to very fine sand and silt with interbedded clay units. The Gramercy aquifer, where present, overlies the Norco aquifer, which overlies the Gonzalez-New Orleans aquifer separated by a clay bed nearly 200 feet thick. The dip and general flow direction of the Chicot equivalent packages is to the south-southwest and the equivalent sands outcrop to the northeast near the northern edge of Livingston and St. Tammany Parishes.¹⁰ The AoR is located along the southeastern portion of the

⁸ Murray, G.E., *Geology of the Atlantic and Gulf Coastal Province of North America* (New York: Harper Brothers, 1961), p. 692.

⁹ McLindon Geosciences, “The Vacherie fault,” 2020, <https://www.mcgeo.me/blog/the-vacherie-fault>. January 31.

¹⁰ Tomaszewski, D.J., “Water-level surface in the Chicot equivalent aquifer system in southeastern Louisiana, 2009,” U.S. Geological Survey Scientific Investigations Map 3173 (2011), 2 pl.

Application Number: 45054
 Plan Revision: December 2025

Mississippi River Alluvial Aquifer and the southwestern portion of the Chicot Equivalent Aquifer System.

Detailed descriptions of the principal aquifers in the AoR are included in **Sections 2.7.2 and 2.7.3**, respectively.

2.2 Maps and Cross Sections of the AoR [LAC 43:XVII.3607.C.1 and LAC 43:XVII.3607.C.1.b.ii / 40 CFR 146.82(a)(2), 146.82(a)(3)(i)]

The following sub-sections introduce maps, cross sections, and other key figures and tables relevant to the RPS Project, as described in LAC 43:XVII.3607.C.1 and LAC 43:XVII.3607.C.1.b.ii /40 CFR 146.82(a)(2) and (3)(i).

2.2.1 RPS Storage Site Map

The 3D geologic model encompasses the five planned injection wells within the RPS North Fairway. The modeled CO₂ plume extent for injection wells RPN-1-INJ through RPN-5-INJ within the RPS North Fairway are shown in **Figure 2.2-1**. The AoR is the maximum extent of the modeled CO₂ plume and pressure front for RPN-1-INJ and is shown in **Figure 2.2-2**. A topographic map of the proposed sequestration site including the section, township and range is shown in **Figure 2.2-2b**.

2.2.2 Sources of Subsurface Data and Methodology

Subsurface structure mapping using seismic data and log data from newly drilled wells, existing wells, and oil field papers (Tyler 1965;¹¹ Hintz 1983;¹² Siegert 1983¹³) indicates regional consistency of sandstone and shale formations. RPS reviewed the following:

- Full suite of logs from RPS' recently drilled stratigraphic test well Palo Alto RPN-S #1. (**Table 2.2-1**)
- Raster log data obtained from the C&E Strategic Online Natural Resource Information System (SONRIS) on 200 existing oil and gas wells in a 360-square-mile area covering the RPS Storage Site (**Figure 2.2-3**).
- Type logs from field papers on the nearby La Pice, Delia, and Laurel Ridge fields (**Figure 2.2-3**).

¹¹ Tyler, C. D., "La Pice Field: ST. James Parish, Louisiana," *Oil and Gas Fields of Southeast Louisiana* vol. 1 (December 1965): pp. 105-109.

¹² Hintze, W. H., "Delia Field: Assumption Parish, Louisiana," *New Orleans Geological Society: Oil and Gas Fields of Southeast Louisiana* vol. 3 (April 1983): pp. 17-17E.

¹³ Siegert R. B., "Laurel Ridge Field: Iberville Parish, Louisiana," *New Orleans Geological Society: Oil and Gas Fields of Southeast Louisiana*, vol. 3 (April 1983): pp. 28-28G.

- Miocene sequence stratigraphic interpretations from the work of Galloway et al.,¹⁴ Fillon and Lawless,¹⁵ Wu and Galloway,¹⁶ and Combellas-Bigott and Galloway.^{17, 18}
- Salt occurrence and structure within the surrounding salt domes was assessed from the work of Ratigan and Hill,¹⁹ Cook,²⁰ and Thompson and Looff.²¹

2.2.2.1 *Reflection Seismic Data*

RPS licensed and interpreted the commercially available seismic data with coverage of the RPS Storage Site; this consists of 140.15 miles of 2D seismic lines (**Table 2.2-2**) and 36.73 square miles of 3D seismic data (**Table 2.2-3**) to characterize the subsurface structure, including presence of faults and fractures, and the local orientation and dip of bedding.

To supplement 3D seismic survey data coverage, RPS conducted the Smoke Bend 3D seismic survey (**Table 2.2-3**). **Figure 2.2-4** shows the boundary of the Smoke Bend 3D seismic survey that RPS conducted in Q2 2023.

2.2.2.2 *Subsurface Interpretation Methods*

The combination of core samples, well logs, and oil field publication data enabled RPS to develop a stratigraphic framework to constrain genetically related sediment packages based on the approximate age and depositional systems tract. Furthermore, by correlating the spontaneous potential (SP) and resistivity measurements from the 200+ raster log files to the biostratigraphic correlations published on “type” wells in field publications, RPS was able to generate detailed structure and thickness maps of the top and base of the primary confining unit and the base of the injection zone.

RPS used S&P Global’s Petra software package to interpret the stratigraphic formation tops and fault cuts on the well log data. Schlumberger’s (SLB) Petrel software was used to generate a synthetic seismogram for the Palo Alto RPN-S #1 stratigraphic test well (the only available complete data set with high confidence in the area) on the Smoke Bend 3D seismic survey. Twenty-four formation tops were tied to the seismic at the well location and initial two-way time (TWT) horizons were interpreted across the survey. Utilizing the established time depth relationship at Palo Alto RPN-S #1 well and Faust equation-based acoustic logs from resistivity, three additional wells were tied to the Smoke Bend survey and two wells were tied to the Romeville

¹⁴ Galloway et al., “Cenozoic depositional history,” 2002.

¹⁵ Fillon and Lawless, “Lower Miocene-Early Pliocene,” 2000.

¹⁶ Wu, X., and Galloway, W.E., “Upper Miocene depositional history of the central Gulf of Mexico basin,” *Gulf Coast Association of Geological Societies Transactions*, vol. 52 (2002): pp. 1,019–1,030.

¹⁷ Combellas-Bigott and Galloway, “Depositional history,” 2002.

¹⁸ Combellas-Bigott, R.I., and Galloway, W.E., “Depositional and structural evolution of the middle Miocene depositional episode, east-central Gulf of Mexico” *AAPG Bulletin*, vol. 90, no. 3 (2006): pp. 335–362.

¹⁹ Ratigan, J. L. and Kevin B. Hill, *Proximity of Class II and Class III Well Caverns to the Edge of the Napoleonville Salt Dome: Topical Report PB-0374*, PB Energy Storage Services, Inc. / Hill Geophysical, July 2013. Prepared for Bridgeline Holdings LP, CrossTex Energy Services, Dow Chemical, K/D/S Promix, Occidental Chemical, Pontchartrain Natural Gas System, and Texas Brine Company.

²⁰ Cook, C. E., “Darrow Salt Dome, Ascension Parish, Louisiana,” *Bulletin of the American Association of Petroleum Geologists*, vol. 22, no. 10, Oct. 1938: pp. 1,412–1,422.

²¹ Thompson, C. and Kurt Looff, “Quantification of Seismic Imaging Accuracy Using Reverse Time Migration at White Castle Salt Dome, Iberville Parish, Louisiana,” Solution Mining Research Institute Fall 2021 Technical Conference, 20–21 September 2021, Galveston, Texas, USA. Conference presentation.

North 3D seismic survey (**Table 2.2-4**). Twenty-four 3D TWT grids were generated for both surveys and connected using regional 2D lines. Faults were interpreted in time on available 2D and 3D seismic data. A 3D velocity model was generated using the TWT horizons and intersecting well tops (true vertical depth [TVD]) within the 3D seismic survey domains. Horizons and faults were converted to depth and verified at intersecting formation tops.

A 3D structural framework model was developed in Petrel integrating the depth horizons, fault planes, and formation tops described above, as well as fault cuts from wells that do not intersect the seismic. In total, 20 faults were interpreted on available well logs, 2D seismic data, and 3D seismic data within the RPS North Fairway model domain (**Figure 2.1-7**), though none transect the upper confining layer within an AoR. The structural framework consists of twenty-four comprehensive structural grids to assess the depth, areal extent, and thickness of the injection and confining zones. During model construction, all horizons were assumed to be conformable relative to each other in the stratigraphic framework. Well tops (**Table 2.2-5**) were used as the primary structural grid control, with seismic interpretation being globally adjusted to match the picks at each well. Salt bodies were delineated in the model with the depth and extent for the Napoleonville Dome and Darrow Dome constrained by the work of Ratigan and Hill,²² and Cook,²³ respectively. The sand and shale formations truncated against the salt bodies and were parameterized as no-flow boundaries. During the modeling process and quality control (QC) of the output structural grids, anomalous well picks were identified and excluded from the next model iteration. This process was useful in eliminating “wind-ups,” or areas where closely spaced wells have large differences in well top depths causing interpolated contour lines to cross without merit. In total, formation tops from 176 wells were used in the structural framework. The 3D model (**Figure 2.2-5**) consists of 12 shale prone intervals (confining layers), 11 sand-prone intervals where injections will be strategically staged on a well-by-well basis, and a fault framework comprised of 20 faults (described in **Section 2.3**).

During seismic interpretation of the Romeville North and Smoke Bend 3D seismic surveys, low impedance geobodies were identified in the upper confining layer. The geobodies were autopicked using an amplitude cut-off designed to limit the geobody extents to above background impedance contrast (**Figure 2.2-6**). For this approach, horizons were generated at the top and base of each geobody and depth converted for use in the geocellular model described below. Due to the lack of penetrations through identified geobodies, the low impedance signature is assumed to indicate sand-prone facies. Each geobody was assigned 30% porosity and 500 mD permeability. Additional details on how the geobodies were used for property distribution are provided in **Appendix 2A**.

A geocellular model (geologic model) was created on a 500-foot-by-500-foot (areal dimensions) grid using the structural framework zones as inputs and providing delineation in the vertical direction. Each zone was divided into N number of layers using the stratigraphic framework, with confining zones having fewer layers and injection zones having more so that each layer is <20 feet thick (**Figure 2.2-7**). A stair-step gridding technique was used for fault integration, which is appropriate for this relatively simple structural setting. Additional details on the grid settings and interpolation methods are provided in **Appendix 2A** and **Attachment B**.

²² Ratigan and Hill, *Proximity of Class II and Class III Well Caverns*, 2013.

²³ Cook, “Darrow Salt Dome, Ascension Parish, Louisiana,” 1938.

Out of an available 50 wells with petrophysical analysis (described in **Section 2.4.2**), 33 facies, porosity, and permeability logs were upscaled into the North Fairway geologic model. The 17 remaining wells will be utilized in the RPS Project South Fairway geologic model. Porosity used a simple arithmetic average while permeability utilized a more appropriate median average, with all leveraging a zone mapping technique to correct any surface mis-ties at the wells so that the upscaled log matched the corresponding cell in the 3D model. Upscaled log values were interpolated in 3D using a gaussian random function simulation. Interpolation parameters and methods are described in **Appendix 2A**. A separate discussion on interpolation of facies is provided in **Section 2.4.2.5**.

2.2.3 RPS Regional Structural Maps

Maps and cross sections of the AoR were generated using available compiled data as discussed in **Section 2.2.2**. This data was assembled to assess the feasibility of geologic sequestration and underground storage confinement. Structural maps and geologic cross sections were generated using the Petrel software platform. The geologic model used 2D and 3D seismic data and well logs from 176 wells in the Project Area.

The stratigraphic units within the AoR and respective type lithologies are initially presented in **Section 2.1.1**. The basic sequence of geologic units, including the Miocene sands of the injection zone, and the basal, primary, and secondary shale confining layers in the AoR, are shown in the stratigraphic column provided in **Figure 2.1-1**. Detailed depth structure maps were generated for top of the primary confining zone (**Figure 2.2-8**), top of injection zone (**Figure 2.2-9**), and top of basal confining layer (**Figure 2.2-10**). Depth structure maps for each of the two secondary confining layers are shown in **Figure 2.2-11** and **Figure 2.2-12**, respectively.

Regional geologic cross sections depict the generally uniform stratigraphic units of interest (**Figure 2.2-13** and **Figure 2.2-14**). The gross injection zone sand packages are confined below by the basal Marg “A” shale and above by the Lower Pliocene shale primary confining unit. Additionally, the individual injection zones are confined internally by cyclic flooding events. Geologic cross sections across the AoR are included as **Figure 2.2-15** and **Figure 2.2-16**. Additional structural sections depicting the structural model and stratigraphic framework are provided in **Section 2.2.6.1**.

Within the RPS North Fairway there are four underground sources of drinking water (USDWs). **Figures 2.2-17** and **2.2-18** show cross sectional views of the depth, thickness, and continuity of confining intervals and the four USDW formations across the Project Area. The lowermost USDW is separated from the proposed primary confining layer by over 2,700 feet true vertical depth subsea (TVDSS). The USDWs are further isolated from the proposed injection zones by the two secondary confining layers (see also: **Figure 2.2-11** and **Figure 2.2-12**). Further discussion of proximal USDWs is included in **Section 2.2.5** and regional USDW details are included in **Section 2.7**.

2.2.4 RPS Regional Thickness Maps

Regional thickness maps were generated using the Petrel software platform to display the thickness of the geologic zones of interest. The gross thickness of stratigraphic units between the base of the lowermost USDW and the top of the primary confining zone is shown in **Figure 2.2-19**. The

stratigraphic thicknesses of the primary and secondary upper confining zones are shown in **Figures 2.2-20, 2.2-21, and 2.2-22**. The stratigraphic thickness of the gross injection zone is shown in **Figure 2.1-6**. The stratigraphic thickness of the basal confining unit is shown in **Figure 2.2-23**. Detailed discussion of the injection and confining zones is included in **Section 2.4**.

2.2.5 Spatial Relationships

The sub-sections below describe the spatial relationships between the proposed project site and regional geologic structures and USDWs.

2.2.5.1 Proximity to Structures

The closest faults to RPN-1-INJ that penetrate the injection zone are normal faults associated with the Laurel Ridge field depicted at a regional scale in **Figure 2.1-5**, and at a local scale in **Figure 2.1-7, Figure 2.2-24, and Figure 2.2-25**. The location, orientation, and extent of these faults are described in **Table 2.1-2**.

The subbasin is bounded to the northwest by the White Castle Dome, northeast by the Darrow Dome, southwest by the Napoleonville Dome, and southeast by the La Pice Dome as depicted in **Figure 2.2-1**. The dome outlines depicted in **Figure 2.2-1** represent the approximate edge of structural perturbation associated with each dome, however the depth to and spatial occurrence of salt within each dome varies. Salt bodies within the Napoleonville, White Castle, and Darrow domes penetrate the injection and confining intervals with recorded top-of-salt at measured depths of approximately 645 feet, 2,313 feet, and 4,395 feet, respectively.^{24,25} The spatial occurrence of salt within the Napoleonville and Darrow Domes at the top of upper confinement, top of injection, and top of basal confinement are depicted in **Figure 2.2-8, Figure 2.2-9, and Figure 2.2-10** respectively. White Castle dome, and the associated salt body, delineated by Thompson and Looff,²⁶ occurs outside of the mapped and modeled area. Salt was not encountered in any wells above the deeper seated La Pice Dome uplift but is suspected to occur at depth as the region around the dome is associated with elevated temperature and salinity.²⁷ **Table 2.2-6** depicts the relative distance to the edge of and orientation of each dome relative to the RPN proposed injection sites. All faulting identified with RPS data has been catalogued in **Table 2.1-2**. (Note RPS does not have seismic data to delineate potential additional faulting above and directly adjacent to the salt bodies within each dome.)

2.2.5.2 Proximity to USDWs

To establish the base of the lowermost USDW for dynamic reservoir simulation and monitoring plan development, RPS used log data from the Palo Alto RPN-S #1 test well, raster log data, and USDW depths reported on C&E SONRIS to map the lowermost USDW in the RPS Storage Site.

²⁴ Bray, B., and Hanor, J., "Spatial variations in subsurface pore fluid properties in a portion of Southeast Louisiana: implications for fluid migration and solute transport," *Trans. Gulf Coast Association Geology Society* vol. 40 (1990): 53–64.

²⁵ Ratigan and Hill, Proximity of Class II and Class III Well Caverns, 2013.

²⁶ Thompson and Looff, "Quantification of Seismic Imaging Accuracy," 2021.

²⁷ Bray and Hanor, "Spatial variations," 1990.

Application Number: 45054
 Plan Revision: December 2025

RPS identified and interpreted the lowermost USDW in 41 wells with shallow SP and resistivity logs following C&E's interpretation criteria.²⁸

The C&E interpretation criteria relates resistivity log response to the EPA's defined formation water salinity threshold of 10,000 milligrams per liter of total dissolved solids (TDS). The mapping reveals that the base of the lowermost USDW ranges from 650–1,200 feet below sea level (**Figure 2.2-26**). The interval above primary confinement and beneath the base of the lowest USDW, ranges in thickness from approximately 2,000 to 4,000 feet across the region, consists of clay and mudstone deposits with intermittent sands. The depth of the lowermost USDW, thickness of the primary confinement, and thickness of the interval separating the base of the lowermost USDW from the top of primary confinement for each of the proposed RPN injection locations is summarized in **Table 2.2-7**. At each location, the base of the lowermost USDW occurs shallower than 1,005 feet TVDSS, and each is separated from the top of primary confinement by more 3,000 feet of shales with interbedded sands.

Within the 3,000+-foot-thick interval between the top of the primary confining layer and the base of the lowermost USDW, RPS has identified two distinct Pliocene secondary confining intervals as depicted in **Figure 2.1-1**, **Figure 2.2-17**, and **Figure 2.2-18**. These intervals, internally labeled as **2nd_Upper_Conf_1** and **2nd_Upper_Conf_2**, are interpreted as mudstones deposited in a floodplain setting during periods of increased aggradation. Chamberlain,²⁹ following the work of Kerr and Jirik,³⁰ described periods of sea level rise during the Pliocene resulting in increased aggradation and higher preservation of compartmentalizing muddy deposits.

The **2nd_Upper_Conf_1** ranges in depth from approximately 2,600 feet to 2,675 feet TVDSS (**Figure 2.2-10**) across the AoR, and the gross thickness increases from 270 feet to 440 feet (**Figure 2.2-21**) moving southwest across the AoR.

The **2nd_Upper_Conf_2** ranges in depth from approximately 1,590 feet to 1,730 feet TVDSS (**Figure 2.2-11**) across the AoR, and the gross thickness ranges from 295 feet to 330 feet (**Figure 2.2-22**) within the AoR.

2.2.6 Lateral Continuity of Formations

The sub-sections below document the lateral extent of the proposed injection and confining formations in the vicinity of the RPS Storage Site.

2.2.6.1 Injection zones

Subsurface mapping (described in **Section 2.2.2.2**) concluded that the injection zone sand packages are continuous across the RPS North Fairway. Variations occur in the thickness and extent of each sand package, caused by variations in local accommodation space, bed thickness, depositional environment, and by processes such as stacking and erosion. Summary details of

²⁸ Office of Conservation: Injection and Mining Division, "USDW Search," http://www.dnr.louisiana.gov/assets/OC/im_div/uic_workshop/2_PRES_USDW.pdf

²⁹ Chamberlain, E. L., "Depositional environments of Upper Miocene through Pleistocene siliciclastic sediments, Baton Rouge aquifer system, southeastern Louisiana," (Master's thesis, Louisiana State University, 2012), 4062.

³⁰ Kerr, D. R., and Jirik, L. A., "Fluvial architecture and reservoir compartmentalization in the Oligocene Middle Frio formation, south Texas." *Gulf Coast Association of Geological Societies, Transactions* vol. 40 (1990): pp. 373–380.

depth and true stratigraphic thickness for each sand package in the vicinity of the AoR are provided in **Table 2.2-8** and described further in **Section 2.4.1**. Sand packages were constrained by identifying cyclic deposition patterns and mapping regional flooding events. RPS collected 428 feet of whole core from the proposed injection zones and 31 feet of whole core from the internal baffles at its Palo Alto RPN-S #1 stratigraphic test well location, to help with detailed characterization of these layers. Thickness maps of these depositional packages, shown in **Figure 2.2-27** and **Figure 2.2-28**, confirm the continuity of the injection packages across the RPN-1-INJ AoR. Vertical and lateral distribution of sand packages are depicted by north-south (**Figure 2.2-15**) and east-west (**Figure 2.2-16**) cross sections through the AoR. At a regional scale, vertical and lateral distribution of sand packages are depicted by north-south (**Figure 2.2-29**) and west-east (**Figure 2.2-30**) cross sections across the RPS North Fairway. Additional details for the wells depicted on these cross sections are provided in **Table 2.1-1**.

Seismic survey data depicted in **Figure 2.2-3**, indicate overall continuity of the sand packages that exceed the minimum resolution of the respective seismic line. Synthetic seismic well ties were performed on six wells, listed in **Table 2.2-4**, to aid in correlating the line-specific reflectivity to the stratigraphy. The Palo Alto RPN-S #1 well tie is provided in **Appendix 2A**. Variability in the vintage and fold of each seismic line constrains the thickness of the sand and shale layers detected and the quality associated with the signal-to-noise ratio. Two seismic sections from the recently acquired 3D Smoke Bend survey indicate sand/shale package continuity on a localized scale at the AoR (**Figures 2.2-31** and **2.2-32**).

The proposed storage site is not trapped by any of the nearby geologic features; however, the domes and faults have influenced sediment deposition and reservoir fluid properties. Syndepositional growth occurred along the Napoleonville Dome during the Miocene, resulting in a thickened sediment wedge toward the dome as evidenced by the thickness in **Figure 2.1-6**. RPS's proposed injection well locations are intentionally distanced from the domes to limit the domes' faulting influence on the CO₂ plume migration. Additionally, the presence of salt within the domes serves as a no-flow boundary and has been delineated and captured as such within the reservoir model.

2.2.6.2 Confining zones

Deposition of the primary (Pliocene shale), basal (Marg 'A' shale) and internal confining units, was initiated during regional/global flooding events, lending to lateral continuity across the entire RPS North Fairway. As with the reservoir sands, local variations in accommodation space and variations in the occurrence and continuity of individual sand beds drive both trends and localized fluctuations in the thickness of each layer. Following the flooding event during the Lower Pliocene, aggradational, low sediment flux deposition is interpreted to occur resulting in a thick mud rich unit. Subsurface mapping (described in **Section 2.2.2**) concluded that the confining zone packages are continuous across the RPS North Fairway. RPS collected 147 feet of whole core from the upper confining layer, approximately 68 feet of whole core from internal confining units and 40 feet of whole core from the lower confining layer at its Palo Alto RPN-S #1 stratigraphic test well location, to help with detailed characterization of these layers.

2.3 Faults and Fractures [LAC 43:XVII.3607.C.1.b.iii and 40 CFR 146.82(a)(3)(ii)]

2.3.1 Regional Faulting

Regional fault systems identified in Louisiana occur in two broad groups in the northwestern and southern parts of the state, as depicted in **Figure 2.1-5**.³¹ The faults in the southern part of the state, from the Tepetate-Baton Rouge Fault Zone to the Gulf of Mexico, are characterized as growth faults—normal faults that are active during sedimentary deposition, which are distinguished by differential thickening of sediments on the downthrown block and increasing displacement with depth. Recent research using LiDAR and other methods has identified fault-line scarps associated with many of these faults, indicating that they intersect the ground surface and are active within the late Quaternary.³² Recency and magnitude of displacement appear to increase to the south, and significant twentieth century subsidence and land loss in coastal Louisiana has been attributed to movement along the southernmost fault systems.³³ Although many of the regional faults in Southern Louisiana may be considered to be active (to have slipped within the Holocene epoch, or the last 11,700 years), most of their recent motion appears to be accommodated by aseismic creep, as earthquakes in Louisiana are infrequent and of relatively low magnitude.³⁴

Faulting in the vicinity of the RPS North Fairway correlates with the regional Scott Fault to the north and Vacherie Fault to the south of the AoR (**Figure 2.1-5**). Local faulting consists of multiple down-to-the-south normal faults, splays, and at least one antithetic fault that set up the Laurel Ridge field (**Figure 2.1-7**). Most of the faulting in the vicinity of the RPS North Fairway is interpreted to terminate beneath the primary upper confining zone of the Lower Pliocene Shale, although the interpreted main segment of the Scott Fault (F-RPN-05) is interpreted to penetrate the confining zone to the northwest of the RPS storage complex. Within the model domain but outside the AoR, F-RPN-05 is interpreted to intersect the Lower Pliocene Sandstone but not the primary upper confining layer or top of the injection zone, as described in **Table 2.1-2** and shown in **Figure 2.1-6**. From the Smoke Bend seismic survey (conducted in Q2 2023; **Figure 2.2-4**), F-RPN-05 is interpreted to terminate in the Lower Pliocene Sand.

2.3.2 AoR Investigation

Subsurface mapping was conducted using 2D and 3D seismic data and wireline well log data (**Figure 2.2-3**), as discussed in **Section 2.2.2**, to assess and delineate faulting and fracturing across the RPS North Fairway.

Faulting in the vicinity of the RPN-1 AoR consists of normal faults (**Figure 2.1-7**). Four of the identified faults intersect the surface projection of the AoR. None of the faults penetrate the

³¹ McCulloh, R. P., and Heinrich, P.V., “Surface faults of the south Louisiana growth-fault province,” *Recent Advances in North American Paleoseismology and Neotectonics East of the Rockies*, vol. 493 (2012): pp. 37–51.

³² McCulloh and Heinrich, “Surface faults,” 2012.

³³ Gagliano, S.M., Kemp, E.B., Wicker, K.M., and K.S. Wiltenmuth, “Active Geological Faults and Land Change In Southeastern Louisiana: A Study of the Contribution of Faulting to Relative Subsidence Rates, Land Loss, and Resulting Effects on Flood Control, Navigation, Hurricane Protection and Coastal Restoration Projects,” U.S. Army Corps of Engineers Contract No. DACW 29-00-C-0034 (July 2003).

³⁴ Stevenson, D. A., and R. P. McCulloh, “Earthquakes in Louisiana,” *Louisiana Geological Survey Public Information Series* no. 7 (2001).

primary upper confining zone and only one (Fault F-RPN-11) intersects an injection zone within the surface projection of the AoR.

One fault has a vertical upper extent within the surface projection of the AoR within an injection zone:

- Fault F-RPN-11 spans the width of the AoR below the basal confining layer and extends vertically into the injection zone, terminating within the Camerina Sand.

One fault has a vertical upper extent within the surface projection of the AoR but below the basal confining unit:

- Fault F-RPN-15 dips to the southwest beneath the projection of the AoR and terminates below the basal confining layer.

Two faults have vertical upper extents outside the surface projection of the AoR but intersect the surface projection of the AoR below the basal confining unit:

- Fault F-RPN-12 intersects the western portion of the AoR below the basal confining layer and extends vertically into Camerina Sand outside of the AoR, terminating within the Camerina Sand.
- Fault F-RPN-13 dips from southwest to northeast and intersects the western margin of the AoR projection below the basal confining layer. F-RPN-13 terminates below the basal confining zone.

As detailed in **Table 2.1-2**, RPS has identified faults that do not intersect the surface projection of the AoR. Seven faults in the vicinity of the AoR that penetrate the basal confining layer (F-RPN-03, F-RPN-05, F-RPN-08, F-RPN-10, F-RPN-16, F-RPN-17, and F-RPN-19), with three faults penetrating the primary upper confining layer (F-RPN-01, F-RPN-04, and F-RPN-09) outside of the AoR. Additionally, RPS has identified four faults within the injection zone strata (F-RPN-02, F-RPN-06, F-RPN-07, and F-RPN-20), one fault within the overburden (F-RPN-18), and one fault is confined to the underlying strata below the basal confining unit (F-RPN-14) in the vicinity of the AoR.

The conclusion that there are no known or suspected faults extending through the injection zone and upper confining zone within the AoR has been validated following interpretation results of the Smoke Bend 3D seismic survey displayed in **Figure 2.2-4**. RPS integrated the interpretations from the Smoke Bend 3D Seismic Survey into the geologic model.

Resistivity micro image logs were recorded and 646 feet of whole core was retrieved from the Palo Alto RPN-S #1 stratigraphic well to inform the extent of fracturing within the primary upper confining zone, the injection zone, and the basal confining zone.

Image Log Interpretation

The SLB Quanta Geo Image log (Image Log) was collected from 2,809 to 11,364 feet MD, spanning from above the primary upper confining zone through to the basal confining zone. Manually interpreted dipset classifications include those related to bedding (bed boundary, cross

bedding, scour surface), deformed bedding, conductive fractures (continuous, non-continuous, and part resistive), resistive fractures (continuous and non-continuous), and minor faults.

Core Description

Core description and fracture interpretation (Core Interpretation) was conducted over the entire 646 feet of core by Core Laboratories to capture type, and orientation of sediment discontinuities. A variety of discontinuities were identified in the core description including those related to bedding (general bedding, shale on sand contact), scour/erosional contacts, injectites, slickensides, deformation bands, closed natural fractures, calcite/dolomite filled fractures, micro-faults, coring induced fractures, and handling fractures/poker chips. These were often associated with different fracture types, including fracture with slickensides, shear fracture with slickensides, normal shear fracture, en-echelon fracture, extension fracture, deformation bands, clastic injectite, desiccation cracks, and coring induced fracture.

Upper Confining Zone

Within the upper confining zone, four fractures were identified via the Image Log over 526 feet including a conductive part resistive fracture at 4,375.5 feet MD, a resistive continuous fracture at 4,414.5 feet MD, a conductive non-continuous fracture at 4,507.5 feet MD, and a resistive non-continuous fracture at 4,561.5 feet MD. The conductive part resistive fracture dips approximately 80 degrees, the conductive non-continuous fracture dips approximately 38 degrees, and the resistive non-continuous fracture dips approximately 50 degrees to the northeast. The resistive non-continuous fracture dips approximately 50 degrees to the northwest. With a total of 4 fractures over the entire 526-foot interval, the measured average fracture density within the primary upper confining zone is approximately 0.007 fractures/linear foot.

In the Core Interpretation, nine different discontinuities were logged over 147.03 feet of retrieved core within the upper confining zone. These include discontinuities related to bedding/bedding contacts, injectites, slickensides (often associated with fractures/shear fractures) and deformation bands. Coring induced fractures and handling fractures/poker chips were also noted.

Slickensides occur within deposits with mottled/contorted bedding and fractured/contorted bedding, occasionally with faulted internal contacts. Approximately 80 slickenside markers were observed within the upper confining layer, 14 of which were faulting internal contacts. Slickenside surfaces are interpreted to be permeability barriers result from slumping, and compaction. The dip for slickensides ranges from approximately 10 degrees up to 80 degrees with varying dip directions. Deformation bands typically have dips of approximately 60 to 85 degrees at various directions.

Observed fracturing in the upper confining zone is limited in quantity and spatial extent. There are no observed mode 1 fractures (opening mode, tensile fractures) within the cores of the upper confining zone. The observed shear fractures and deformation bands are all interpreted to be closed. These fractures are not interpreted to present a migration risk.

The confining zone, consisting of smectite-rich clays, is interpreted to lack the “brittleness” necessary for fracture dilatancy as described by Ingram and Urai.³⁵ Confining zone brittleness is further discussed in **Section 2.5.3.**

Injection Zone

Within the injection zone there were a total of 41 fractures/minor faults identified on the Image Log over the 6,344-foot interval including two conductive continuous fractures, 17 conductive non-continuous fractures, two conductive part resistive fractures, 13 minor faults, three resistive continuous fractures, and four resistive non-continuous fractures.

Conductive continuous fractures occur between 7,579 and 7,580.5 feet MD, with dips of approximately 50 and 68 degrees to the northwest. Seventeen conductive non-continuous fractures were observed throughout the injection zone. Isolated fractures occur at approximately 4,910 feet MD and 6,211 feet MD with dips of approximately 65 to 70 degrees to the west-southwest, 6,487 feet MD with a dip of approximately 80 degrees to the southeast, 6,929 feet MD with a dip of approximately 68 degrees to the south, 7,579 feet MD with a dip of approximately 40 degrees to the west-northwest, 9,449 feet MD with a dip of approximately 61 degrees to the northwest, 10,972.5 feet MD with a dip of approximately 45 degrees to the east-southeast, 10,973.5 feet MD with a dip of approximately 65 degrees to the north-northwest, 10,979.5 feet MD with a dip of approximately 50 to 53 degrees to the west-northwest, and at approximately 10,993 feet MD with a dip of approximately 70 degrees to the southeast. A pair of fractures occur at 8,083 feet MD with dips of approximately 40 and 50 degrees to the south. Between 11,134 and 11,136.5 feet MD five southwesterly dipping fractures occur with dips from approximately 35 to 70 degrees. Conductive part resistive fractures occur at 5,862.5 feet MD with a dip of approximately 60 degrees to the south-southwest and at 5,990.5 feet MD with a dip of approximately 45 degrees to the north.

Minor faults occur throughout the injection zone as solitary faults or in groups. Solitary minor faults occur at approximately 5,971.5 feet MD with a dip of approximately 50 degrees to the west-northwest, 7,092.5 feet MD with a dip of approximately 50 degrees to the south, and 10,827.5 feet MD with a dip of approximately 32 degrees to the east southeast. Between approximately 6,668 and 6,669.5 feet MD a pair of west dipping minor faults occur with dips of approximately 50 to 55 degrees. From approximately 8,853.5 to 8,856.5 feet MD a cluster of six minor faults occur as either south-southeast dipping faults with approximate dips of 50 to 55 degrees, and north-northwest dipping faults with approximate dips of 30 and 35 degrees. At 10,881.5 to 10,882 feet MD there is a pair of north dipping minor faults with dips between approximately 35 and 42 degrees. Resistive continuous fractures were observed at 6,053.5 feet MD with a dip of approximately 38 to 40 degrees to the west-northwest, 11,152 feet MD with a dip of approximately 35 degrees to the northwest, and 11,169.5 with a dip of approximately 40 degrees to the north-northwest. Resistive non-continuous fractures occur at 6,632 feet MD with a dip of approximately 45 degrees to the south-southwest, 6,665 feet MD with a dip of approximately 55 to 60 degrees to the west, 9,449 feet MD with a dip of approximately 60 degrees to the southeast, and at 11,195 feet MD with a dip of approximately 40 degrees to the east.

³⁵ Ingram, G.W. and Urai, J.L., “Top-seal leakage through faults and fractures: the role of mudrock properties,” in *Muds and Mudstones: Physical and Fluid Flow Properties*, eds. Aplin, A. C., Fleet, A. J., Macquaker, J. H. S., Geological Society, London, Special Publications, 158 (1999): 125–135.

Application Number: 45054
Plan Revision: December 2025

With a total of 41 fractures/ minor faults over the 6,344-foot interval, the measured average fracture density within the injection zone is approximately 0.006 fractures/linear foot.

In the Core Interpretation, nine different types of discontinuities were noted within the 458.61 feet of cored injection zone (inclusive of internal confinement). These discontinuities include scour/erosional contacts, injectites, deformation bands, slickensides, closed natural fractures, a micro-fault, coring induced fractures, and handling fractures. Scour/erosional contacts are common within cross bedded, trough cross bedded, and slumped/contorted sandstone deposits, dipping from approximately 0 to 20 degrees at various directions. Injectites have dips ranging from approximately 60 to 80 degrees to the northeast, east, south, and northwest.

Deformation bands are limited to a thinly bedded silty/sandy shale and sandstone interval, from approximately 9,806 to 9,812.4 feet MD, with dips of approximately 70 to 85 degrees to the northwest, north, and southeast. Slickensides are less common compared to the upper confining interval and occur in conjunction with shear fractures or fractures, with dips of approximately 20 to 30 degrees to the west, east, and north.

Closed natural fractures were identified within slightly calcareous silty shale in two distinct populations, those associated with normal shear fractures, from 8,345.6 to 8,346 feet MD, with dips from approximately 20 to 30 degrees to the northwest and northeast, and those associated with en echelon fractures, from approximately 10,491 to 10,501 feet MD, with approximately 60 to 80 degree dips to the north and west. A single, closed micro-fault was logged at 9,828.8 feet MD, with a dip of approximately 80 degrees to the west.

Observed fracturing within the injection and internal confining zones is spatially limited and predominantly healed. Of the 41 fractures/minor faults, only 2 fractures were interpreted to be conductive continuous fractures. This means that the fractures have maintained shape and are not mineralized over. These fractures have the greatest potential to enhance fluid flow. RPS interpreted 17 fractures as conductive non-continuous fractures, meaning they had fluid within them but were damaged and not extensive. These fractures, interpreted as damaged, are much less likely to have any lateral or vertical continuity to them. Thus, these 17 fractures negligibly enhance permeability. Two additional fractures were characterized as conductive part-resistive, implying that mineralization has partially occluded these fractures. These fractures also are interpreted to lack lateral or vertical continuity necessary to enhance flow. Therefore, RPS concludes that a single-porosity model is appropriate to model fluid flow in this system as the low fracture density, ~0.006 fracture/linear foot, coupled with the largely discontinuous and disconnected nature of these observed fractures will not enhance fluid flow at the model scale.

Lower Confining Zone

There were a total of five fractures identified on the Image Log from 11,196.5 to 11,360.5 feet MD within the lower confining zone, including three conductive non-continuous fractures, one resistive continuous fracture and a resistive non-continuous fracture. Conductive continuous fractures occur between 11,271.5 and 11,273 feet MD, with dips from approximately 45 to 55 degrees to the north-northwest and approximately 38 degrees to the north-northeast. The resistive non-continuous fracture occurs at 11,273.5 feet MD and has a dip of approximately 65 degrees to the east. The resistive continuous fracture occurs at 11,327.5 feet MD and dips at approximately 58 degrees to

the south-southwest. Over the 164-foot interval, the measured average fracture density within the lower confining unit is 0.03 fractures/linear foot.

Within the cored interval of the basal confining zone (40.15 feet), four types of discontinuities were identified: calcite/dolomite filled fractures, slickensides, coring induced fractures, and handling fractures/poker chips. In total, 11 slickensides, and 9 calcite/dolomite filled fractures were observed translating to approximately 0.5 naturally occurring fractures per linear foot. The slickensides are interpreted as healed shear fractures, typically short, and low-angled.

Calcite/dolomite filled fractures are predominantly associated with extension fractures within slightly calcareous silty shale, with fracture dips as low as <10 degrees to the northeast but more commonly between approximately 40 and 80 degrees to the west, northwest, and southwest. A single calcite/dolomite filled en echelon fracture occurs in a thin calcareous sandstone interbed, with a dip of approximately 65 degrees to the south. Slickensides, associated with shear fractures and rare faulted internal contacts, dip from approximately 20 to 60 degrees to the north, northeast, southeast, west and northwest.

RPS concludes the risk of vertical fracture communication across the lower confining interval is very low due to the sparse frequency, length, orientation, and cementation of the observed fractures.

2.3.3 Regional Implications on Fluid Flow

While RPS interprets there are no faults or fracture zones within the AoR that transect the upper confining zone, evidence exists in the area that faulting can serve both as conduits and as barriers to fluid flow. Surrounding oil fields including Laurel Ridge, Samstown, Darrow, La Pice, Delia, and Napoleonville (**Figure 2.1-7**) produce from Miocene sands but are interpreted to have been sourced by pre-Miocene source rocks. The hydrocarbons are interpreted to have migrated along faults from the source rocks into the Miocene reservoirs. Electromagnetic surveys conducted along the surface traces of growth faults in Southern Louisiana also indicate that they may be sealing or non-sealing, and in the lower Mississippi Delta vents or cones that seep water, gas, and mud, have been observed along active faults.³⁶ Style and orientation of faulting relative to the local (or regional) stress field may play a role in fault transmissibility.

Radial tensile faulting, observed above the salt domes, also acts as a conduit for vertical fluid migration as noted in Bray and Hanor³⁷ based on the altered temperature and fluid compositions more than 1,000 feet above the top of the salt intrusions. Fault movement in the region is interpreted to have occurred in stages and, as suggested at the Darrow and La Pice Dome, the degree of fault transmissibility may have been altered over time. Faulting also acts as a barrier to flow in the area as oil and gas accumulations associated with Laurel Ridge, Samstown, and La Pice fields are compartmentalized and trapped by faulting.

Figure 2.2-25 and **Table 2.1-2** show the lateral distance from the edge of the closest AoR to the faults identified in the vicinity of the RPS North Fairway. Based on available well picks and 2D and 3D seismic data, only one of the twenty identified faults, F-RPN-05, is interpreted to penetrate

³⁶ Gagliano et al., “Active Geological Faults,” 2003.

³⁷ Bray and Hanor, “Spatial variations,” 1990.

the top of the injection zone but does not intersect the primary upper confining layer. F-RPN-05 is interpreted to be a south-dipping normal fault, with an approximate strike of 080° , lateral length of 26,500 feet, and maximum throw of 350 feet. Because the estimated maximum throw of F-RPN-05 is less than the interpreted minimum thickness of the primary upper confining layer along its length (approximately 650 feet true stratigraphic thickness), F-RPN-05 is not interpreted to create a conduit for fluid flow by juxtaposition of permeable layers. Thus, F-RPN-05 would not be anticipated to compromise the sealing capacity of the primary upper confining layer, even if CO_2 from RPN-1-INJ were to migrate beyond the modelled AoR boundary and intersect the fault plane.

F-RPN-11 is interpreted to intersect the surface projection of the RPN-1 AoR, extending into and terminating within the injection zone in the Camerina sand. F-RPN-12 is interpreted to intersect the surface projection of the RPN-1 AoR of the RPN-1 AoR below the basal confining unit, extending into and terminating within the Camerina sand approximately 0.12 miles northwest and upgradient of the surface projection of the AoR. F-RPN-11 and F-RPN-12 are assumed to be sealed within the lower confining layer due to the fault orientation and abundance of clay, as discussed further in **Section 2.4.3**. F-RPN-11 is not interpreted to perturb the permeability in the injection zone due to the lack of throw at the tip of the fault and the highly permeable, unconsolidated nature of the sands. RPS does not anticipate these faults impacting the predicted migration of the CO_2 plume within the reservoir. Similarly, the plume would not be expected to migrate down the fault due to the lack of permeability along the fault in the lower confining layer, the buoyancy of CO_2 , and the high permeability of the Camerina sand. An assessment of the fault stability of these and other surrounding faults is discussed below in **Section 2.3.4.1**.

The interpreted geometries and kinematics of each of the 20 faults identified in the vicinity of the RPS North Fairway are detailed in **Table 2.1-2**. Due to the limited nature of available seismic and well log data, estimations of extents, orientations, and offsets are approximate. Geometric fault interpretations have been revisited and revised with the Smoke Bend 3D seismic survey.

2.3.4 Addressing Uncertainties

RPS conducted the Smoke Bend seismic survey to assess the uncertainty regarding the degree of faulting within and around the AoR (see survey boundary in **Figure 2.2-4**). The seismic survey results are integrated into the geologic interpretations and model. RPS collected 645.79 feet of core, resistivity micro imager, bulk density and dipole sonic log data to characterize the frequency, connectedness, and nature of fracturing along with the stress conditions around the storage site. See data collection table (**Table 2.2-1**).

Faulting detected in the Smoke Bend survey, including the lateral and vertical extent of the fault(s), have been mapped, the fault throw calculated, and fault juxtaposition analysis performed to assess the potential fluid migration. Various seismic attributes such as curvature and discontinuity volumes have been interrogated to assess and characterize the probability of fracturing within the AoR. Additionally, the data was integrated to assess fault stability.

2.3.4.1 Fault Stability Assessment

No faults were identified extending through the injection zone and upper confining zone within the AoR. RPS does not anticipate planned injection rates and volumes for the RPS storage complex to increase slip risk on surrounding faults located outside of the AoR. However, to confirm no

Application Number: 45054
Plan Revision: December 2025

impact, RPS contracted geomechanical specialists, TechLimit, to conduct deterministic assessment of fault-slip potential. Stress parameters for the fault slip potential modeling were derived from the sonic and density logs, images logs, and core analyses collected from the Palo Alto RPN-S #1 stratigraphic test well, summarized in detail in **Section 2.5**. All work was performed utilizing TechLimit's proprietary Toolbox software.

TechLimit quality controlled the log data, SLB mechanical earth model (MEM), fracture populations, and fault and horizon surfaces prior to conducting the analysis. The 1D MEM was used to populate a 3D volume containing the fault geometries to apply stress and strength for geomechanical analysis. The mechanical properties from the Palo Alto RPN-S #1 were upscaled and propagated laterally, guided by the geologic model horizons across the entire model, as this is the only well in the area with the requisite dataset. Stress conditions were extracted across fault surfaces and reactivation risk was calculated in 3D. 2D reactivation risk maps were calculated for key horizons representing the shallow (Lower Pliocene shale and sand), middle (Lower Cris I shale and sand), and deep (Camerina shale and sand) portions of the storage complex, and polar plots were generated at these key horizons to consider other structural permeability elements including fractures.

The risk of reactivation of pre-existing faults and fractures is measured as distance from failure (delta pressure) on a Mohr diagram, as depicted in **Figure 2.3-1**. In this diagram, the Mohr circle represents the effective far-field stress conditions. As pore pressure increases, in the case of injection, the effective minimum horizontal effective stress will decrease. This in a sense increases the size of the Mohr circle and moves the circle closer to the failure envelope. The change in pressure, the delta pressure required to create a Mohr circle that intersects the "Existing Fault Failure Envelope", represents the pressure increase required to achieve "critical stress" conditions along a "critically oriented fault". Critical stress orientation represents the orientation of a fault or fracture relative to maximum horizontal stress ($S_{H\max}$) such that the effective stress ratio on the fault is maximized. As conservative assumptions, fault cohesion was set to 0 psi and the equivalent friction angle to intact rock at the corresponding depth was utilized. Additionally, the change in pressure required to have the Mohr circle intersect the "Intact Rock Failure Envelope" represents the minimum stress required to create a new fault or fracture. Low delta pressure represents a high/susceptibility for failure, and high delta pressure represents a low risk/susceptibility for failure.

The lowest observed delta pressure predicted in the model is no less than 800 psi, and the stated cases in presentation (Lower Pliocene, Lower Cris I, and Camerina) all exceed 1,100 psi. As stated above, these predicted delta pressures are considered very conservative due to the assumption of zero cohesion and the likelihood of slip along the fault at these pressures would be quite low. For comparison, in RPS's reservoir model the greatest delta pressure resulting from RPS's injection operation is 650 psi (at the wellbore) in the Amph B Sand, which is substantially below the lowest predicted delta pressure in the fault slip potential model.

Furthermore, investigation of the risk maps shows that the modeling predicts a higher required delta pressure for the majority of the surface along each fault plane. The modeling results, inclusive of the reactivation risk maps, Mohr circle diagrams and stereonets (pole plots) for each horizon are provided in **Appendix 2B**.

2.4 Injection and Confining Zone Details [LAC 43:XVII.3607.C.2.a and 40 CFR 146.82(a)(3)(iii)]

2.4.1 Depth, Aerial Extent, and Thickness

The injection and confining zones within the AoR are comprised of Miocene to Pliocene sandstones, mudstones, and claystones. At the injection site, the stratigraphic sequence of sedimentary units consists of intermingled saline reservoirs and shale layers underlain by a basal confinement. The depth, areal extent, and thickness of the injection and confining zones have been evaluated based on available well logs from 200+ wells across the region and seismic survey data (**Figure 2.2-3**), which were used to develop RPS's 3D Geomodel.

RPS acquired seismic data in the Smoke Bend survey and licensed and interpreted commercially available seismic data with coverage of the RPS Storage Site. This data was interpreted following the methods described in **Section 2.2.2** to characterize the subsurface structure, including presence of faults and fractures and the local orientation and dip of bedding.

RPS utilized the licensed seismic survey data, in conjunction with other referenced data, to determine the extent, depth, thickness, and lithology of the injection and confining zones and subsequently construct the 3D geologic model. Wireline log data from offset wells were used to determine the petrophysical properties of the injection and confining zones, as discussed in **Section 2.4.1.2**.

Following additional seismic surveys that RPS conducted over the AoR and core analysis from the Palo Alto RPN-S #1 stratigraphic test well, the petrophysical properties and the lateral extent, depth, thickness, and continuity of the pertinent injection and confining units were updated in the 3D Geomodel. RPS reran the reservoir simulations as detailed in the AoR and Corrective Action Plan.

2.4.1.1 *Injection Zone*

As discussed in **Section 2.2.6**, the injection and confining zones are broadly continuous across the entire region, and the injection zones extend well beyond the AoR. The depth, thickness, and areal extent statistics for the injection zones for RPN-1-INJ were extracted directly from RPS's 3D Geomodel. Structural maps of the gross injection zone are provided in **Figure 2.2-9**, **Figure 2.2-10**, and **Figure 2.1-6**.

The gross injection interval for RPN-1-INJ, totaling approximately 5,430 feet vertical thickness, has been subdivided into gross sand and shale packages based on regional depositional episodes and bounded by interpreted flooding surfaces. In total, the injection zone contains 11 sand packages and 10 shale packages. Summary details of depth and true stratigraphic thickness for each sand package in the vicinity of the AoR (the areal domain shown in **Figures 2.2-27** and **2.4-1**) are described in **Table 2.2-8**. The 10 inter-injection zone shale packages will be summarized below with the confining system.

Structure maps depicting the depth and dip orientation of each sand package within the AoR are compiled in **Figure 2.4-1**. The structural dip across the sand packages is consistently to the south/southwest, with subtle variations in orientation, likely driven by syndepositional salt withdrawal into the Napoleonville Dome. Subtle dip orientation variations are most likely attributed to spatial fluctuations in sedimentation during the filling of the subbasin. Structural dip

varies from approximately 3–8 degrees with the dip shallowing in the younger sand packages as the subbasin filled. The dip orientation to the south/southwest will cause the CO₂ plume to migrate updip to the north/northeast. However, the impact of the dip in some areas can be offset by property variation, such as permeability and porosity of the injection zone, which may cause the CO₂ plume to move in other directions resulting in a more circular plume geometry compared to an elongated shape.

The spatial variability in true vertical thickness and true stratigraphic thickness of each injection unit across the AoR are displayed in **Figure 2.2-27** and **Figure 2.2-28**, respectively. Within the RPS North Fairway, the sediment thickness increases to the southwest towards the Napoleonville Dome. Within the AoR, fluctuations in sediment thickness vary layer to layer caused by paleo-source direction and paleo-accommodation space at the time of deposition, as well as differential compaction related variability in net sand.

2.4.1.2 *Confining Zone*

As discussed in **Section 2.2.6**, the primary upper and basal confining zones are broadly continuous across the entire region. Both the primary upper and lower confining units are continuous over the entire AoR and beyond. The depth, thickness, and areal extent statistics of the primary upper and basal confining zones for RPN-1-INJ were extracted directly from RPS's 3D Geomodel. Structural maps of the primary upper and basal confining zones are provided in **Figure 2.2-8**, **Figure 2.2-10**, **Figure 2.2-20**, and **Figure 2.2-23**.

Five internal shale packages were identified and mapped to understand the network of internal baffles that will aid in staged injection. The packages are continuous across the AoR and beyond. The depth and thickness of the confining units in the vicinity of the AoR, including the primary upper and basal confining units, secondary upper confining units, and inter-reservoir baffles interpreted to seal and compartmentalize the injection interval at RPN-1-INJ, are summarized in **Table 2.4-1**. The structure, true vertical thickness, and true stratigraphic thickness maps for each of the identified confining layers are assembled in **Figure 2.4-2**, **Figure 2.4-3**, and **Figure 2.4-4**, respectively.

RPS updated the 3D Geomodel with results from the Palo Alto RPN-S #1 stratigraphic test well and the Smoke Bend 3D seismic survey conducted in Q2 2023. RPS recovered 19 whole cores from 13 different intervals, a total of 646 ft of whole core, across the injection and confining zones in the Palo Alto RPN-S #1 stratigraphic test well. These results are provided in **Appendix 2**.

2.4.2 **Porosity, Permeability, and Capillary Pressure**

2.4.2.1 *Petrophysical Methods*

RPS contracted geoscience consulting firm, Core Geologic, to conduct petrophysical modeling utilizing 50 wells proximal to the RPS Storage Site, shown in **Figure 2.2-1**, and listed in **Table 2.4-2**, with at least Spontaneous Potential (SP) and Deep Resistivity (RESD) logs. This well set provided the best available data quality and azimuthal coverage surrounding the RPS project area. A core to log calibration was performed with the extensive core and well log data collected in the Palo Alto RPN-S #1 to generate a core calibrated model (**Figure 2.4-5**). This core calibrated model was applied to 12 additional wells with triple combo logs, listed in **Table 2.4-3**, to calculate total porosity (PHIT), effective porosity (PHIE), air permeability (Kair), water saturation (SW), a mineral model, total organic carbon (TOC) and volume clay (Vclay) curves for each well. RPS

then utilized multi-linear regression (MLR) to extrapolate the core calibrated model to the remaining 37 wells with SP and RESD listed in **Table 2.4-4**. The output curves for the regression were PHIT, PHIE, Kair, gamma ray (GR), and Vclay. A supervised facies analysis was conducted on all 50 wells to characterize spatial and vertical lithologic variability. RPS utilized the resulting curves from this study as inputs to the 3D heterogeneous geologic model, as described in **Section 2.2.2.2**.

The petrophysical modeling was conducted utilizing Geoactive's Interactive Petrophysics software. All probabilistic, clustering, and regression methods were conducted utilizing built-in modules within Interactive Petrophysics. The full suite of tops, listed in **Table 2.2-5**, were supplied to enable layer-based refinement.

Core to Log Calibration

The core to log calibration utilized 149 discrete depth measurements (sample points) of porosity and air permeability collected via routine core analysis on sandstone lithologies, and 65 sample points of NMR porosity and liquid permeability measurements collected via tight rock analysis protocol for the shale and mudstone lithologies. 100 X-ray diffraction (XRD) sample points were utilized to quantitatively constrain the mineralogy. Effective porosities were determined by Core Laboratories for these points leveraging the clay percentages provided in the XRD.

The core calibrated geologic model for the Palo Alto RPN-S #1 well (**Figure 2.4-5**) was established by creating relationships for TOC, Vclay, a mineral model with fluid analysis, and a permeability model.

TOC

The TOC and empirical heavy mineral volume curves were calculated in weight percent (wt%) via density regression and Passey's Delta Log R method³⁸ (Passey, et al, 1990) utilizing Interactive Petrophysics' TOC module. The density regression consisted of 16 different built-in density relationships. Passey's method was applied to the compressional slowness (DT), bulk density (RHOB), and neutron porosity (NPHI) curves and then a weighted average of the three was selected. The average of the density regressions was selected as most appropriate for the sands and the weighted average of the Passey method was selected for the shales. The empirical heavy mineral volume was derived by multiplying the final TOC curve by 0.4. This relationship assumes pyrite to be the dominant heavy mineral and relies on a strong geochemical relationship between TOC and the precipitation of pyrite. Pyrite content from the core XRD analysis was used to constrain this factor. The TOC and heavy minerals curves were subsequently applied as inputs to the mineral model.

Vclay min

The clay volume analysis was performed through calculation of multiple clay volume curves from common clay indicators. GR, resistivity, neutron, and density logs were utilized in the assessment and curves were generated through the establishment of clean and 100% clay endpoints for both Neutron-Density cross plot and based on a linear GR trend. These endpoints were constrained by the XRD mineralogy described above. In the case of the linear GR method, layer by layer

³⁸ Passey, Q.R., Creaney, S., Kulla, J.B., Moretti, F.J., and Stroud, J.D. "A practical model for organic richness from porosity and resistivity logs." *AAPG Bulletin* vol. 74, no. 12 (1990): pp. 1,777–1,1794.

adjustments to the end members were performed to achieve an optimum fit. The final Clay volume was selected based on the minimum Vclay encountered for all of the methods. The final Vclay curve (Vclay-min) was subsequently applied as an input to the mineral model.

Mineral Model

Upon completion of the TOC and Vclay analysis, a probabilistic mineral model was developed to aid in prediction of bulk mineral composition, porosity, and fluid parameters. As mentioned above, the TOC and Vclay_min were input into the model along with the GR, shallow resistivity (RESS), RESD, RHOB, NPHI, and photo electric factor (PEF). Additionally, the SLB combinable magnetic resonance (CMR) nuclear tool was incorporated into the model to further constrain the porosity (PHIT & PHIE). The mineral composition outputs consisted of kerogen (Vker), clay (Vclay), quartz (Vquartz), carbonate (Vlime), pyrite (Vpyrite), oil (Voil), water (Vwater). These values were calibrated against the XRD core data, and qualitatively sense-checked against the SLB Lithoscanner – elemental capture spectroscopy log. The confidence level for each input curve was adjusted to optimize the correlation with the control data. The model predicted both effective and total porosity, guided by the CMR log along with the routine and tight rock core analyses. However, the petrophysical model overpredicted effective porosity in the tight rocks relative to the values provided in the core analysis. Though RPS understands the core data to have lower measured effective porosity, the wireline-determined effective porosities were used in the model as a conservative approach. The fluid parameter outputs consisted of effective water saturation, total water saturation, bound water saturation, irreducible water saturation, bulk volume water, bulk volume water flushed. Water saturation, S_w was solved for following the Archie Method,

$$S_w = [(a/\Phi^m) * (R_w/R_t)]^{(1/n)}$$

where R_t , observed bulk resistivity, Φ is observed porosity, R_w , formation water resistivity, was set to 0.06; a , a constant, was set to 1; m , the cementation factor, was set to 1.9 in the shale layers and 2.0 in the sand layers; and n , the saturation exponent, was also set to 1.9 in the shale layers and 2.0 in the sand layers.

Permeability

Permeability analysis was performed following a variety of established methods including: Wyllie-Rose, Timur-Coates (KTIM), Exponential, Jenkis & Lucia, Morris Biggs, and Schlumberger Dole Research (KSDR). Each method was applied utilizing the above specified Archie parameters, the CMR data along with the porosity curve from the mineral model and compared against the core permeabilities described above. The Timur-Coates and Schlumberger Dole Research methodologies matched the RCA air sandstone permeabilities best, however all methodologies overestimated the core measured permeability values in the mudstones significantly, even after converting brine permeability to air permeability. Consequently, RPS utilizes two different curves for modeling permeabilities in the sand prone layers and shale prone layers as no method would honor core permeabilities in both rock types simultaneously.

The Timur Coates permeability equation utilizing CMR data is:

$$K_{TIM_CMR} = a_1 * (10^4) * \left(\frac{\phi_{FF}}{\phi_{BF}}\right)^{b_1} * (\phi_{CMR})^{c_1}$$

Where $a_1 = 1$, $b_1=2$, $c_1=4$, ϕ_{FF} = free fluid porosity, ϕ_{BF} = bound fluid porosity, and ϕ_{CMR} is the CMR measured total porosity.

The Schlumberger Dole Research permeability equation utilizing CMR data is:

$$K_{SDR_CMR} = a_2 * (T_{2,log})^{b_2} * (\phi_{CMR})^{c_2}$$

where $a_2 = 4$, $b_2=2$, $c_2=4$, T_2 is the relaxation time in milliseconds, and ϕ_{CMR} is the CMR measured total porosity.

To address the discrepancy observed between the core permeability measurements in the shale/mudstone layers with the KTIM prediction, the KTIM curve was decreased by a power of 10. This adjustment, while still overestimating the core permeability values, was a closer fit to the core data when converted to Kair. The KSDR curve was selected to continue in the analysis for the reservoir intervals, and the modified KTIM curve was selected to continue in the analysis for the confining layers.

Multi-Linear Regression Analysis

A Multi-linear regression (MLR) workflow was utilized, compensating for the limited log set for 37 of the 50 wells, to predict Vclay, porosity and permeability logs from the core calibrated model. The Interactive Petrophysics' MLR module utilized a least squares methodology with training curves from the pilot and 12 triple combo wells, and 3-4 input curves from each target well to predict the desired logs.

In preparation to run the MLR process on the remaining 37 wells in the study, SP logs were first normalized via a 2-point log normalization method to standardize all variations in the SP response, ensuring any differences in tool response did not unjustly impact formation interpretation. The normalized SP curves (SPn) were then utilized along with RESD to predict GR logs. The logs, compared with the 12-well training set, achieved an R-squared value of 0.72.

Following the generation of GR curves (GR_MLR) for each well, supervised cluster analysis was performed on all 50 wells utilizing the GR (or GR_MLR), RESD, and SPn logs to generate electrical facies logs. The clustering analysis was performed with the Interactive Petrophysics cluster module following the k-means method. Clustering was tested for 2 through 9 clusters before deciding on 5 clusters. In each cluster iteration, the cluster spread was evaluated along with the mean and standard deviation for each of the three input logs to assess the appropriate number of divisions. The resulting facies logs from this analysis were used as an input into subsequent MLRs.

The MLR process was then utilized to predict Vclay, PHIT, and PHIE curves for each of the wells. GR, RESD, SPn, and facies logs were used for the prediction of each curve along with the respective training curves. The resulting model R-squared values for the Vclay, PHIT, and PHIE curves are 0.75, 0.78, and 0.89 respectively, when compared back to the training set. Three wells did not have an SP curve to utilize in the regression analysis and thus an alternate model was developed from the remaining available inputs. The resulting alternate model R-squared values for the Vclay, PHIT, and PHIE curves are 0.74, 0.71, and 0.87 respectively. As discussed above, two separate permeability models were generated to account for the sand prone and shale prone

intervals. Both models were separately trained in the MLR to produce KTIMn, and KSDR curves for each of the wells.

Data Considerations

Many of the wells utilized in this study were drilled between 1954 and 1986 when drilling and logging practices were far less advanced than present day. These older wells were drilled with less sophisticated drilling muds and at much less conservative rates of penetration, as the target objective was much deeper. The smectite-rich clay mineralogy, low UCS sediments, water-based fluids, and aggressive drilling practices resulted in very challenging hole conditions for logging the non-primary objective hole section. Large washouts, greater than the tools depth of investigation warranted consideration in the interpretation of the logs. Additionally, the vintage of these logs means that most were not originally available digitally and thus the potential for variable digitization quality exists.

Inspection of the output MLR curves revealed permeability anomalies in 8 wells, listed in **Table 2.4-5**. Close inspection revealed that anomalous high spikes in permeability were being artificially created by unrealistically low RESD values. These values corresponded to digitizing issues on old log data. To limit these values from biasing the MLR and from being mapped into the geologic model, a floor resistivity of 0.1 was set for these digitized curves and the permeability regressions were re-run. Additionally, 6 wells, listed in **Table 2.4-6** were observed to have anomalously low permeability ranges relative to surrounding wells for comparative SP responses. Further investigation revealed that the resistivity range was off for these wells for corresponding SP response as compared to offset wells. To adjust for this discrepancy in SP response, a 50% reduction in resistivity value was applied, so that the resistivity response was in line with offset wells. This adjustment enabled spatial lithologic variability to be captured without unrealistically biasing the model.

2.4.2.2 Injection Zone Porosity and Permeability

Injection zone porosity and permeability were estimated petrophysically based on the method described above, then statistically kriged in the 3D geologic model. The average porosity and +/- one standard deviation to the mean was extracted for each injection unit from the model within the AoR (**Table 2.4-7**). Average values ranged from 24.5% to 28%, with clean sand porosity exceeding 30% in the shallower formations. Within the larger model domain, injection zone porosities ranged from 23% to 26.5%, with clean sand porosity exceeding 35%. Drivers for the variability in porosity include environment of deposition and compaction. Key parameters affected by environment of deposition include grain size, sorting, grain shape, clay content, and net-to-gross variations laterally and vertically. Spatial variability in porosity for each injection unit is depicted in **Figure 2.4-6**.

Permeability-porosity relationships for the sand intervals were established as described in **Section 2.4.2**. Median permeability was derived from the model and ranged from 50 mD to 365 mD for each sand package in the AoR, with clean sand packages exceeding 1 darcy (**Table 2.4-7**). Spatial variability in permeability for each sand package is depicted in **Figure 2.4-7**.

As further discussed in Attachment B, RPS measured the drainage and imbibition relative permeability on six composite samples taken from the injection sand intervals at Palo Alto RPN-S #1. In all cases, Brooks-Corey function was fit to each dataset. Three sets of curves, each

representative of low, mid, and high permeability values (500, 1,500, and 5,000 mD) were utilized in the model.

The first relative permeability test was conducted at Core Lab starting with drainage relative permeability cycle followed by the imbibition cycle. Due to high sample brine permeability of 2.8 darcy and high mobility ratio between CO₂ and brine, a minimum water saturation of 70% was achieved during the drainage cycle. The imbibition cycle was started at this high-water saturation. The resulting relative permeability curves from these measurements only cover the high-water saturation range. The sample was desaturated using the Porous Plate method to determine its theoretical minimum water saturation. Effective gas permeability was measured at the minimum water saturation which was later utilized to calibrate the Corey model to fit the relative permeability measurements. Core Lab followed the procedure proposed by Lun et al.³⁹ to upscale the relative permeability measurements. However, the upscaling process did not result in extending the curves to low water saturations due to a sharp decline in water permeability and minimal increase in gas permeability near 70% water saturation.

The next three composite samples, with brine permeability values ranging between 5 and 12 darcies, were sent to Intertek for relative permeability measurements due to test equipment availability. Due to the limited range of saturations observed from the first test, RPS instructed the lab to first desaturate the samples using the Porous Plate method, conduct the imbibition cycle, and then conduct the drainage cycle. This procedure seemed to help the measurements to cover a larger range of water saturations. The Corey model was fit to the measurements. Intertek performed two additional Steady-State relative permeability measurements on samples with brine permeability values of 7 and 92 mD to assess flow behavior for lower quality reservoir within the project area.

2.4.2.3 Confining Zone Porosity and Permeability

Confining zone porosity and permeability values were estimated based on the methods described in **Section 2.4.2.1** and interpolated in the 3D geologic model (**Section 2.2.2**). The average modeled porosity and +/- one standard deviation to the mean was extracted for each confining unit from the model in the AoR (**Table 2.4-8**). The primary upper confining zone averages 22.5% and the primary basal confining zone averages 18%. Within the larger model domain, the estimated effective porosity of the primary upper confining zone averages 18%, and the basal confining zone averages 15%. As discussed in **Section 2.4.2.2**, the petrophysically derived effective porosity curves over the core derived effective porosities estimated but were utilized for model construction to remain conservative. Median permeability values from the modeled confining zones range from 0.0007 mD to 0.01 mD within the AoR. Drivers for the variability in porosity and permeability include environment of deposition, and compaction. Key parameters affected by environment of deposition include clay content, sand and silt content, and net-to-gross variations laterally and vertically. Spatial variability in porosity and permeability for each confining layer is depicted in **Figure 2.4-9** and **Figure 2.4-10** respectively.

³⁹ L. S. Lun et al. "Developing consistent relative permeability and capillary pressure models for reservoir simulation of CCS projects", Society of Petroleum Engineers SPE-216722-MS, ADIPEC (2023)

2.4.2.4 Capillary Pressure

Capillary pressure measurements provide information on the distribution of pore throat size and how fluids occupy the pore space under the balance of buoyancy and capillary forces. That information is critical to understanding how CO₂ penetrates the injection zone and the ability of the confining zone to impede leakage.

To evaluate threshold pressures for CO₂ injection and likely CO₂ column heights in confining zones, RPS conducted capillary pressure measurements on 57 samples (26 samples from cores and 31 samples from rotary sidewall cores) collected from the Palo Alto RPN-S #1 stratigraphic test well. Of the collected samples, three were from the Pliocene overburden, seven were from the upper (principal) confining zone (including four shale/siltstone samples and three argillaceous sandstone samples), 44 were from the injection zone (including 20 sandstone samples and 24 shale/siltstone samples from internal reservoir confining units), and three were from the lower confining zone (**Table 2.4-9**). Samples of the shale/siltstone lithology (34 total from confining zones and from the internal reservoir confining units) were analyzed using high pressure mercury injection, whereas the sandy material samples (23 total, of which 20 from the injection unit and three from the upper confining unit) were analyzed using advanced overburden mercury injection which allowed for sample analysis under the net confining stresses mimicking those of the in-situ conditions. In addition, seven samples from the confining units were subjected to the threshold entry pressure (TEP) testing under conditions mimicking those in situ (CO₂ displacing brine under appropriate confining stress) to evaluate CO₂ threshold entry pressures and CO₂ column heights (**Table 2.4-10**). Capillary pressures are based on analysis of the above data from the Palo Alto RPN-S #1 stratigraphic test well, .

Plots of the mercury/air capillary pressure curves of the samples from cores and from rotary sidewall cores are presented in **Figures 2.4-11 and 2.4-12**. The mercury/air capillary pressure curves of sandstone samples from the injection zone (gray lines in both figures) and sample from the various confining zones (upper, lower, and internal/within injection zone) exhibit distinct entry pressures and curve shapes (**Figures 2.4-11 and 2.4-12**). Mercury entry pressures vary in the 1 to 5 pounds per square inch absolute (psia) range for the injection zone sandstones and generally within the 100 to 10,000 psia range for the various confining units, with lower values corresponding to higher-permeability samples (**Table 2.4-9**). Several of the sandier samples from the confining units have lower mercury entry pressures (in the 10 to 100 psi range) and higher permeabilities.

It is generally expected that higher permeability rocks will contain larger pores and that the non-wetting fluid (mercury in laboratory conditions) can enter at lower injection pressures. Pore throat radius (r) can be computed from capillary pressure as:

$$r = \frac{2\sigma \cos(\theta)}{P_c};$$

where P_c is the capillary pressure at any non-wetting phase saturation, while σ and θ are the interfacial tension and contact angle of wetting and non-wetting phase (mercury/air in laboratory conditions), respectively. Empirical pore throat size distributions were computed from each available capillary pressure curve using the following assumptions:

$$\sigma_{Hg/Air} = 485 \text{ dyne/centimeter}$$

$$\theta_{Hg/Air} = 140 \text{ degrees}$$

The largest pore throats within the injection zone sandstones vary in size between 20 and 100 micrometers, with the median pore sizes mostly within the 10 to 30 micrometer range (**Figures 2.4-13 and 2.4-14 and Table 2.4-9**). The largest pore sizes are smaller than 19 μm for the confining unit samples; however, the pore sizes in the confining unit samples exhibit a much greater variability (generally from 0.001 to 10 micrometers), with median values between 0.002 and 0.5 micrometers (**Figures 2.4-13 and 2.4-14 and Table 2.4-9**). Pore throat size generally increases with permeability across different lithologic units (**Table 2.4-9**).

The mercury/air laboratory system entry pressures were corrected for cation exchange capacity and water salinity (using XRD and formation water data presented in **Sections 2.4.3 and 2.7.6**) and converted to gas/water and CO₂/brine systems under laboratory and reservoir conditions using various assumptions for the interfacial tension and contact angle (**Table 2.4-9**). As with the mercury/air system, the calculated entry pressures for other systems are higher in the confining unit samples and are inversely proportional to the permeability (**Table 2.4-9**).

For the TEP testing of shales from confining units, the samples were maintained at equivalent reservoir net confining stress, reservoir pressure, and temperature, and synthetic formation brine was injected to saturate the sample and estimate its permeability to brine (**Table 2.4-10**). Following that, supercritical CO₂ was applied to displace the brine at several incrementally increasing differential pressures, with samples allowed to equilibrate for a minimum of 48 hours at each pressure. The measured CO₂ threshold pressures varied from 400 psi to >1,000 psi, resulting in calculated CO₂ column heights in confining zones of 2,566 ft to >8,248 ft (**Table 2.4-10**).

2.4.2.5 Net-to-Gross

To better understand the distribution of sand in each zone within the 3D geologic model domain, a net-to-gross ratio was generated from the facies logs (see **Section 2.4.2.1**). Five facies were assigned to 50 wells, 33 of which were used in the North Fairway geologic model. Facies ranged from 1 (clean sand) to 5 (shale), with 2, 3, and 4 representing mixed facies scaled between the two end members. Facies logs were upscaled into the geologic model using a midpoint pick averaging method. Upscaled logs were interpolated throughout the geologic model using a sequential indicator simulation, an appropriate method for qualitative descriptors. For each injection and confining zone, model cells from group 1 and 2 were summed vertically and divided by the total thickness of the zone to provide a net to gross ratio. Maps depicting the spatial distribution of net-to-gross for the injection and confining zones are assembled in **Figure 2.4-15** and **Figure 2.4-16**, respectively.

2.4.3 Mineralogy and Petrology

The primary dataset supporting mineralogic and petrologic characterization consists of XRD analyses and point-counted thin section analyses performed on core materials collected from the Palo Alto RPN-S #1 stratigraphic test well depicted in **Figure 2.4-17**. This dataset is supplemented by the petrographic evaluation of 31 conventional core samples using scanning electron microscopy (SEM)—23 samples from conventional SEM and 8 samples from argon ion-milled

SEM analysis (**Appendix 2D**). Additional core and cutting data used in regional understanding is depicted in **Figure 2.4-18**.

A total of 75 samples of the injection zone formation and 16 samples of the confining zone were analyzed by XRD, along with three samples of the Pliocene overburden and six samples of the lower confining unit. Of those samples, 67 were collected from the conventional cores and 33 were from the rotary sidewall cores. Minerals such as quartz, potassium feldspar, plagioclase, calcite, dolomite, siderite, pyrite, and total clay were quantified as percentages (complete XRD data are included in **Appendix 2D**). The XRD clay mineralogy data were further broken down into weight percentages of smectite, illite/smectite mixed phase (with an estimated percentage of smectite), illite/mica, kaolinite, and chlorite.

A total of 48 samples of the injection zone formation and 7 samples of the confining zone were analyzed by point-counting of thin sections, along with four samples of the lower confining unit, all collected from the conventional core (complete point-count analytical data are included in **Appendix 2D**). The point-count analytical data quantified a larger number of mineral categories in the matrix and framework grains, including replacement minerals and authigenic minerals, but did not distinguish between the reactive clay phases such as smectite and illite. The point-count data also included percentages of pore types and rock fragments. For the purposes of comparison to the XRD data and providing solid phase inputs to the geochemical modeling, the point-count analytical data were grouped into similar mineral categories as those reported in the XRD data, the composition percentages were normalized to exclude the non-mineral phases (rock fragments, porosity, etc.), and the relative percentages of smectite and illite from XRD were used to calculate the relative amounts of these phases within the undifferentiated clays from the point-count data. The reported mineral compositions from both XRD and point-counting analysis were averaged (weighted for the number of samples) to provide geochemical modeling inputs for the injection zone (sandy and shale-dominated mineralogies) and for the confining zone (**Tables 2.4-11 and 2.4-12**). This procedure is explained in greater detail in **Section 2.8**.

2.4.3.1 Injection Zone Mineralogy and Petrology

Based on the core descriptions from the Palo Alto RPN-S #1 stratigraphic test well, the injection zone sandstones primarily consist of tan to medium brown, medium grained, well sorted, cross-bedded sand, such as that at depths of approximately 6,350 ft or 7,560 ft, typical of distributary channel depositional environments found in fluvio-deltaic settings. The grain sizes are variable, however, sometimes with noted interbeds of silty shale, fine- to coarse-grained sand, and conglomerate ranging in bed thickness from several inches to several feet (e.g., from 5,450 to 5,480 ft). Finer-grained sandstones associated with conglomerate beds often exhibit flaser cross-bedding and are overturned, whereas the finer-grained beds associated with the base of channel deposits often contain numerous fossil fragments. Lower part of the injection zone (depth greater than 9,100 ft) tends to contain finer-grained, well sorted sands in medium- to thick-bedded or amalgamated bed assemblages, cross-bedded to flaser cross-bedded, with organic matter and fossil fragments commonly localized along laminae or disseminated within locally contorted sand beds. Only occasional sandstone beds are noted as carbonate cemented (e.g., 3% of the interval from 9782.0 to 9791.7 ft). The shale-dominated portions of the injection zone, such as those from 9,800 to 9,840 ft and from 10,470 to 10,500 ft, are comprised of medium to light gray, mostly thin- to thick-bedded silty shale, occasionally calcareous or sideritic, interbedded with thin-bedded to laminated fine-grained sands and bioturbated, argillaceous sands.

Sandstone petrology is typically classified based on the ratio of common detrital components – quartz, feldspar, and lithic (rock) fragments, referred to as a Q:F:R ratio. This ratio forms the basis of sandstone petrologic interpretation by indicating the relative proportion of common clastic components. The injection zone sandstones are classified predominantly as subarkose sandstones, although numerous samples were found to be sublitharenite and quartzarenite sandstones, and a small number of samples were found to be litharenite and feldspathic litharenite sandstones (**Figure 2.4-19**). Injection zone formation samples contained an average thin section point-count measurement Q:F:R ratio of 85:7:8 (**Table 2.4-13**, normalized to exclude all other minerals). Although the majority of samples plot as subarkose sandstones, the samples from Palo Alto RPN-S-1 display some degree of petrologic heterogeneity.

Within the injection zone formation, two subsets of samples were distinguished based on their mineralogic profile – those with dominantly sandy mineralogy (less than 50 weight percent [%] clays) and those dominated by shale (50% or greater of clay minerals). The sandy mineralogy dataset consisted of 67 XRD samples and 43 point-count samples, covering most of the vertical interval of the injection zone. The shale-dominated mineralogy dataset consisted of eight XRD samples and five point-count samples, found at various depths throughout the injection zone.

A review of the XRD data indicated that the sandy samples of the injection zone consisted mostly of quartz (ranging from 40 to 90%), potassium feldspar (1 to 9%), plagioclase (1 to 11%), and clays (total of 1 to 49%). Several samples, from depths mostly greater than 9,800 ft, contained up to approximately 5% calcite, whereas dolomite, siderite, and pyrite were sporadically noted throughout the entire vertical range at low quantities, often below 2% (except for a sample from 10,175 ft with 31% dolomite). Within the clay portion, smectite and illite comprised more than half of the mass (and often greater than 70% of the total clay mass), whereas the rest of the clay mass was comprised of kaolinite and minor amounts of chlorite. Point-count data from the sandy portion of the injection zone (normalized to exclude rock fragments and pore spaces) were consistent with the XRD data, except for a slightly larger percentage of quartz relative to the clay minerals. Also, a greater amount of calcite (up to approximately 20%) was reported in the point-count data from the intervals already noted in XRD data (several samples deeper than 9,800 ft), possibly due to the greater ability to detect various calcitic phases, such as in fossils and grain coatings.

Mineral composition of the shale-dominated samples of the injection zone was similar to the composition of the sandy samples, except for the lower percentages of quartz and higher percentages of total clay in the shale-dominated samples, especially in the point-count data. The average percentage of quartz in the shale-dominated samples was reported as 30% (XRD) and 22% (point counts), whereas it was as high as 77% (XRD) and 81% (point counts) in the sandy samples. In turn, total clays comprised on average 59% (XRD) to 70% (point counts) of mass in the shale-dominated samples, but that percentage fell to 13% (XRD) and 6% (point counts) in the sandy samples.

Injection zone dataset from the SEM petrographic evaluation consists of 23 samples from sandstone beds and four samples from siltstone/silty shale beds. The analysis of SEM images from sandstone beds confirmed the observations from core descriptions/analysis, XRD, and point-count analysis, indicating that the framework grains consist primarily of quartz (most common), plagioclase, potassium feldspar, and rock fragments, the intergranular pores are common (10 to

20%) to abundant (>20%) and well interconnected, and pore-filling and grain-coating constituents/cements are trace (<1%) to minor (1 to 5%) in abundance (**Appendix 2D**). Quartz grains occasionally appear frosty due to cements and the most common pore-filling and grain-coating constituents include quartz overgrowths, detrital clay matrix, and authigenic kaolinite. In the siltstone beds, the grain framework primarily consists of quartz, lesser plagioclase and potassium feldspar grains, and occasional titanium-rich grains, authigenic siderite, and calcite. The intergranular space in siltstone beds is mostly filled with detrital clay matrix and authigenic kaolinite, locally concentrated authigenic pyrite and iron oxide, and clay-size grains of quartz, plagioclase, potassium feldspar, authigenic siderite, and calcite dispersed in the matrix.

2.4.3.2 Confining Zone Mineralogy and Petrology

Based on the core descriptions from the Palo Alto RPN-S #1 stratigraphic test well, the confining zone consists primarily of oxidized, red to dark gray, mottled to contorted, mud cracked, silty shale and dark to medium gray, silty to sandy shale. These shales comprise 52% to 76% of the recovered core intervals and often occur in bedding sequences thicker than 10 ft. The shales are interbedded with medium gray to dark olive, medium-bedded, rotted, bioturbated, very fine-grained sandstones and siltstones, or with medium light gray to olive, thin-bedded, ripple cross-laminated to slumped, burrowed, fine-grained sandstones, and rarely, with thin (<2 ft) sequences of conglomerate or paraconglomerate. The noted lithologies are interpreted as representative of the following depositional environments: lagoons, tidal mud flats, crevasse splays, washovers, and tidal creeks.

Mudstone petrology is often classified based on the ratio of mineralogical components – quartz/feldspar, carbonates, and clays. This ratio accounts for the primary minerals that frequently comprise mudstones. The average composition of the principal confining unit is classified as a clay-rich siliceous mudstone based on the classification scheme of Gamero-Diaz et al.⁴⁰ The average quartz/feldspar-carbonate-clay ratio for principal confining unit samples from the sampled interval of Palo Alto RPN-S-1 is 60-3-37 (**Table 2.4-14**, normalized to exclude all other minerals).

A review of the XRD data indicated that the samples of the confining zone consisted of approximately 30 to 60% quartz (52% average), 20 to 65% total clay (35% average), 3 to 6 % potassium feldspar, 5 to 10% plagioclase, and several other minerals (calcite, dolomite, siderite, and pyrite) that were sporadically detected at low percentages (mostly below 1.5%). One sample, from depth of 4,434 ft, contained approximately 10% calcite and 3.5% siderite. Within the clay mineral portion, smectite and illite comprised more than 80% of the mass, whereas the rest of the clay mass was comprised of kaolinite and minor amounts of chlorite. Point-counting data from the confining zone (normalized to exclude rock fragments and pore spaces) were consistent with the XRD data, except for a smaller percentage reported for quartz (41%) and a greater percentage reported for the total clay minerals (40%). Also, a greater amount of calcite (approximately 26%) was reported in the point-count data from the same sample already noted in XRD data (4,434 ft), possibly due to the greater ability to detect various calcitic phases.

Confining zone dataset from the SEM petrographic evaluation consists of three samples of the primary confining unit siltstone/silty shale beds. The grain framework primarily consists of quartz, lesser plagioclase, potassium feldspar, and mica grains, and rare titanium-rich grains, zircon, and

⁴⁰ Gamero-Diaz, H., Miller, C., and Lewis, R., 2012, sCore: a classification scheme for organic mudstones based on bulk mineralogy: AAPG Search and Discovery Article 40951.

chlorite. Open intergranular pores are rare and two of the samples appear bioturbated. The intergranular space is mostly filled with clay and clay-size particles of quartz and feldspars, with authigenic iron oxide formed in rare intragranular and moldic pores.

2.4.3.3 *Regional Comparison*

For comparison to the site-specific data and to provide a regional/lateral continuity context, thin sections from analogous Miocene sandstones and shale in the Mississippi Delta were evaluated, as described by Watson in a dissertation submitted in 1965.⁴¹ The analogue samples were taken from Continental Navarre No. A-1 (Well No. 1/ “Navarre #1”) well depicted in **Figure 2.4-18**. While the “Navarre #1” core samples were extracted approximately 77 miles to the west of and deeper than the RPS target storage interval, the samples were extracted from the equivalent Miocene section, and RPS interprets the minerals to be sourced from the same provenance.

Quartz, carbonaceous fragments, feldspar (unspecified), clays (unspecified), mica, chlorite, tourmaline, glauconite, and zircon were noted in the thin section descriptions and were quantified using petrographic point-counting. The relative mineral abundance for each sample, in percent of composition, is depicted in **Table 2.4-15**. The composition percentages were normalized to exclude the addition of nonmineral phases (rock fragments, porosity, etc.). Confining layer mineralogy was inferred from a single analogous Miocene shale thin section description (thin section #9 in **Table 2.4-15**). Cuttings descriptions from the following wells support the mineralogic characterizations: Stanolind Oil and Gas Company Dugas and Leblanc No. 1 (Well No. 4 in **Figure 2.4-18**) and Humble Oil and Refining Company Federal Land Bank No. 1 (Well No. 9 in **Figure 2.4-18**).

Within both wells, sand grain size varied from siltstone and very-fine grained sandstone to coarse and pebble-sized, particularly in the shallower, fluvial environment. Sands, shales, and clays alternate with periodic shell layers and with coal layers in the middle and upper portion of the injection zone. Marls and calcareous streaks were noted predominantly deeper in the Middle and Lower Miocene sediments. Sediment colors noted included buff, white, red-brown, grey, olive grey, and olive green. The sediment descriptions indicate the presence of minerals including silica, calcite, glauconite, bentonite, and iron rich minerals.

Descriptions of cuttings, thin section analysis results, and Watson’s associated interpretation are consistent with the results from Palo Alto RPN-S #1 stratigraphic test well. They are also consistent with RPS’s assessment of an overall prograding shoreline from a neritic to alluvial and floodplain environments of deposition (EOD’s) through the Miocene, with fluctuations in sand and shale driven by fluctuations in sea level and accommodation space. Watson concluded that mineral distributions were laterally continuous across the study area within each lithosome; therefore, RPS believes the mineralogic data from Palo Alto RPN-S #1 are applicable to the RPN-1-INJ site.

2.4.3.4 *Compatibility with CO₂ Injection Stream*

The mineralogy of the injection and confining zones are interpreted to be compatible with the anticipated CO₂ injection stream (reference stream discussed in detail in **Section 7.1**). Quartz, the

⁴¹ Watson, Stuart T., "Petrography and Lithostratigraphy of Some South Louisiana Subsurface Tertiary Rocks," (PhD diss., Louisiana State University, 1965), LSU Historical Dissertations and Theses. 1059. https://digitalcommons.lsu.edu/gradschool_disstheses/1059

dominant mineral within the reservoir and confining units, is traditionally considered to be geochemically inert and unreactive with the CO₂ injection stream. Additional minerals that comprise significant fractions of the relevant units include feldspars, clays, and carbonates. These minerals have the potential to react (precipitate/dissolve) in response to changes in reservoir formation water chemistry due to gas injection. The degree of mineral reactivity within the confining and reservoir systems were evaluated using two types of geochemical modeling approaches: 1) thermodynamic equilibrium modeling, and 2) kinetic reaction pathway modeling. Equilibrium modeling yields predicted mineral mass changes resulting from gas injection that are associated with holistic thermodynamic equilibrium (unconstrained by mineral reaction kinetics), whereas kinetic reaction pathway modeling provides an assessment of predicted reaction progress and associated mineral mass/porosity changes within a defined period of time. Details of the geochemical modeling setup/inputs and a discussion of modeling results are provided in **Section 2.8**.

Geochemical compatibility modeling results support the assumption that the reservoir and confining units are chemically compatible with CO₂ injection. Geochemical modeling efforts were completed using a variety of input conditions intended to reflect the influence of variable mineralogy as well as a range of pressure/temperature conditions associated with current reservoir conditions and anticipated maximum variation due to the physical injection process. Equilibrium modeling results predicted net mineral mass increases due to mineral precipitation for both the confining unit and the reservoir unit. Predicted mineral mass increases within the confining unit provide additional assurance that the confining unit will successfully function as a barrier to upward migration of fluids. Predicted mineral mass increases within the reservoir unit have the potential to decrease total porosity and influence injection conditions; however, kinetic reaction pathway modeling completed over an 80-year period following gas injection resulted in predicted total porosity increases of less than 0.1% (porosity units).

Total mineral mass increases predicted by equilibrium modeling are driven overwhelmingly by quartz precipitation. The kinetics of quartz precipitation are comparatively slow, resulting in minimal predicted impact to total mineral mass change and total porosity change over operationally relevant periods of time. The limited impact to total mineral mass and total porosity predicted by kinetic modeling suggests that the confining and reservoir units are compatible with the CO₂ injection.

A discussion of specific predicted geochemical reactions given the mineralogical makeup of the injection and confining zones follows in **Section 2.8**.

2.4.4 Storage Capacity, Injectivity, and Integrity

As described in detail in **Section 2.10**, The storage capacity of the RPS storage complex was evaluated using a methodology modified from the DOE method developed by Goodman et al.⁴² Storage capacity calculations were performed using the total modeled pore volume of sand-prone intervals (injection zones) within the five AoRs of the RPS North Fairway, and volumetric displacement efficiency values published by Goodman. Tenth and ninetieth percentile (P10 and

⁴² Goodman, A. et al. "U.S. DOE methodology for the development of geologic storage potential for carbon dioxide at the national and regional scale," *International Journal of Greenhouse Gas Control*, vol. 5 (2011): 952–965

P90) estimates of storage capacity were calculated based on P10 and P90 values for volumetric storage efficiency. Using this method, the total volumetric storage capacity of the RPS Project is estimated at P10—512 MMt; and P90—1,247 MMt. Each of the estimated storage capacity values is greater than the proposed injection volume for the RPS North Fairway of 260 MMt of CO₂ using five injection wells.

The storage capacity variability within the AoR will impact carbon dioxide storage capacity in terms of total pore space available for storage. In the RPS North Fairway, where gross thickness is greater, the reservoir will have more pore space for CO₂ storage. Where gross thickness is smaller, the reservoir will have less pore space for CO₂ storage. However, variability is relatively low in the thickness of the AoR. The variability in thickness and porosity of the AoR are considered and accounted for in the reservoir model, the results of which are summarized in the AoR and Corrective Action Plan.

The injectivity index of RPN-1-INJ is calculated from the simulation model assuming the current reservoir conditions and the perforation schedule. The calculated injectivity index of the wells ranges between 0.2 and 1 MM standard cubic feet (scf)/day/psi. The high porosity and permeability of the sands provides the injectivity needed to meet the proposed injection rates. However, RPS will conduct an injectivity test before injection starts to confirm the design volume can be injected into the formation without exceeding 90% of the formation's fracture pressure.

The primary upper confining layer has sufficient integrity with regards to fluid transport based on its thickness, permeability, ductility, and continuity across the entirety of the AoR and beyond. As described in **Section 2.4.1**, the primary upper confining layer has an average stratigraphic thickness of 670 feet in the vicinity of the AoR, and a minimum thickness of 580 feet. The permeability of the primary upper confining unit is assumed to be low (modeled median value of 0.001 mD), which, in combination with its thickness, makes it an effective barrier to fluid flow. Although the estimated unconfined compressive strength is low (average ~1,253 to 1,769 psi across the AoR; **Section 2.5.2**), high clay contents (particularly of smectite, kaolinite, and montmorillonite) contribute to formation ductility. Calculated brittleness index (BRI) values for the primary confining zone are <2, indicating that it is ductile and cannot maintain open fractures (**Section 2.5.3**). This is supported by the lack of mode 1 fracturing observed in the Palo Alto test well (see **Section 2.3.2**). Fractures are therefore expected to have negligible influence on the sealing capacity of the primary upper confining unit. Data collected as part of the Smoke Bend Survey and Palo Alto RPN-S #1 stratigraphic test well confirms the sealing capacity of the primary upper and lower confining units.

Given the large thickness of the primary upper and lower confining unit, including at the minimum thicknesses, the variability in thickness of the confining layers is not anticipated to affect carbon dioxide confinement. The existence of redundant confining units (both secondary upper confining layers and inter-reservoir baffles) bolsters this conclusion.

2.4.5 Additional Data Collection

As described in the Pre-Operational Testing Plan, before the commencement of injection, RPS will conduct an injectivity test and collect and analyze wireline log data and whole cores from the RPN-1-INJ injection well location. RPS will then update the geologic model and rerun the reservoir model and, if needed, update the AoR based on core analysis from the injection well location.

RPS drilled a stratigraphic test well, the Palo Alto RPN-S #1, in Q2 2023 to address data gaps. The data collection program included wireline logging and sampling, detailed in **Table 2.2-1**, and 646 feet of 4-inch-diameter core as depicted in **Figure 2.4-17**. The coring program recovered approximately 248 feet of shale across the upper, lower, and internal confining layers, and approximately 398 feet of sand across 9 different sand layers.

The resulting cores and wireline log data provided direct measurements of key characteristics of the injection zone and confining zone, including mineralogy and petrology, key model parameters (porosity, permeability, pore pressure, capillary entry pressure, relative permeability, and capillary pressure curves), geomechanical and petrophysical information, fluid samples, and geochemical data. The cores were subsampled to roughly 3-foot increments where the elemental and mineralogic composition were quantitatively and qualitatively characterized with X-ray diffraction, X-ray fluorescence, scanning electron microscopy, and thin section analyses. These measurements were correlated to the wireline logs including the elemental capture spectroscopy tool to achieve a refined understanding of the elemental distribution.

2.5 Geomechanical and Petrophysical Information [LAC 43:XVII.3607.C.2.b and 40 CFR 146.82(a)(3)(iv)]

2.5.1 Geomechanical and Petrophysical Characteristics of the Confining Zone

RPS collected extensive wireline log and core data at the Palo Alto RPN-S #1 stratigraphic test well to characterize the geomechanical properties of the confining and injection zones. The wireline dataset for the evaluation consisted of compressional sonic, shear sonic, bulk density, and resistivity micro-imager. Additionally, SLB's MDT tool was run to collect 13 pressure samples (**Table 2.5-1**), and to conduct a mini-frac test (**Table 2.5-2**). SLB integrated the elastic log data, pressure data, and the mini frac to generate a calibrated 1D mechanical earth model (MEM).

Utilizing the 646' of whole core, rock mechanics tests were conducted (or attempted) at 19 depths intervals (RM testing intervals) to evaluate the mechanical properties of the primary and internal confining intervals as well as some of the proposed injection intervals. The testing regimen consisted of: triaxial unconfined compressive strength (Triax), Biot's coefficient determination, Brazil tensile strength, fracture toughness, and uniaxial pore volume compressibility (UPVC) tests.

Additionally, RPS utilized compressional velocity logs from two proximal wells, the Roy V Comeaux et al. #1 (C&E Serial Number 204755), and the Savoie Industries Inc. #1 (C&E Serial Number 178472) to further assess the strength and ductility of the injection and confining zones around the RPS Project Area.

2.5.2 Average Rock Strength

RPS characterized the rock strength of the confining and injection formations in both confined and unconfined conditions. The unconfined compressive strength (UCS) was calculated for the entire

8.5 inch hole section of the Palo Alto well by SLB from the compressional sonic log data via the McNally⁴³ equation.

$$UCS = 1200e^{-0.036\Delta t}$$

SLB then calibrated the UCS model to align with the shear failures captured in the wellbore stability model. **Figure 2.5-1** displays the calculated UCS with depth for the Palo Alto test well. The unconfined compressive strength (UCS) of the confining zone was also approximated using two other sonic log-based relationships from the literature to gain insight to the potential variability in rock strength. The additional relationships used were that of Ingram and Urai⁴⁴

$$\log UCS = -6.36 + 2.45\log (0.86V_p - 1172)$$

and following the relationship for unconsolidated Gulf Coast sediments from Zoback⁴⁵

$$UCS = 1.4138 * 10^7 \Delta t^{-3}$$

where V_p is compressional velocity, and Δt is slowness or $1/V_p$.

Table 2.5-3 displays the estimated UCS variability with depth from the 1D MEM.

Triax tests were conducted at Core Laboratories on a series of core plugs for each of 19 distinct RM testing intervals to assess the strength at unconfined and 3 confining stress conditions. Additionally, UCS were also estimated via Mohr-Coulomb failure envelopes, constructed from the confining pressure and compressive strength sets from each RM testing interval. The triaxial compressive test results are summarized in **Table 2.5-4**. The Mohr-Coulomb envelope consistently predicted higher UCS than the individual compressive tests. Due to plug sampling challenges for RM testing interval #19, the requisite number of plugs were not available to perform the standard triaxial compressive strength tests. Instead, a multi-stage triaxial compressive strength test was conducted on one plug and the UCS was derived via the resulting Mohr-Coulomb envelope.

Within the upper confining interval, the average wireline derived UCS ranges from 1,263 to 1,769 psi. Whereas the laboratory observed UCS ranged from 1,253 to 1,432 psi, and the confined strength at near reservoir conditions ranges from 4,282 to 5,101 psi, for RM testing intervals 1-3.

Within the lower confining interval, the average wireline derived UCS ranges from 1,845 to 2,983 psi, and 7,283 psi for the Mohr-Coulomb UCS at RM testing interval #19. Note that the Mohr-Coulomb estimated UCS is consistently higher than standard UCS tests so RPS considers this UCS for the lower confining zone higher than actual. Due to the nature of the multi-stage test, the sample was not taken to failure until approximately 1.5 times the anticipated confining stress. Under these conditions a compressive strength of 14,556 psi was achieved. The scale compressive strength was then estimated to be approximate 12,133 psi at the anticipated confining pressure.

The average wireline derived UCS for the internal confining intervals ranges from 1,366 to 5,232 psi. RM testing interval #14, in the Operc Shale (baffle) exhibited a UCS of 3,865 psi, and a

⁴³ McNally, G. H. N., "Estimation of coal measures rock strength using sonic and neutron logs," *Geoexploration* vol. 24 (1987): pp. 381–395.

⁴⁴ Ingram and Urai, "Top-seal leakage," 1999.

⁴⁵ Zoback, M.D., *Reservoir Geomechanics* (New York, Cambridge University Press, 2007).

Application Number: 45054
 Plan Revision: December 2025

confined strength of 11,677 psi at a net confining pressure of 3,449 psi. RM testing interval #10, a local shale baffle within the Cib Op sand interval, exhibited a UCS of 4,778 psi, and a confined strength of 9,132 psi at a net confining pressure of 2,560 psi.

Injection Intervals

The average wireline derived UCS ranged from 1,150 to 4,499 psi. Laboratory strength testing was conducted in the Camerina, Operc, Rob L, Amph B, Cib Op, Lwr Cris I, Tex W, 1st Upr Miocene and Top Miocene sands. The laboratory measured UCS ranges from 58 to 1,298 psi, and compressive strengths at approximate reservoir net confining stress ranges from 3,925 to 14,201 psi.

In addition to the compressive strength, RPS utilized the core and elastic logs to evaluate mechanical properties important to fracturing including: Poisson's ratio, Young's modulus, tensile strength, and compressibility.

Poisson's ratio describes the lateral or transverse strain of a rock for an applied longitudinal or axial strain. Poisson's ratio is inversely related to the ability of the rock to fracture where 0.5 indicates there is no volume change of the material, whereas values less than 0.25 are increasingly more likely to fracture.

Static Poisson's ratio measurements were obtained from both the Triax and UPVC tests and are summarized in **Table 2.5-4**. The UPVC tests were only able to be conducted on the reservoir samples but are interpreted to be the more reliable measurements. The UPVC derived Poisson's ratio is an "Effective Poisson's ratio" where the horizontal stress coefficient, K_0 , is measured when the pore pressure of the sample is depleted, thereby effectively increasing overburden as lateral strain is maintained. Effective Poisson's ratio is then calculated by:

$$\nu_E = \frac{K_0}{(1 + K_0)}$$

Poisson's ratio measurements were reported from Triax testing at 17 of 19 RM testing intervals, with RM intervals #12 and #15 indicating highly unreliable measurements were obtained during testing.

SLB estimated dynamic Poisson's ratio utilizing compressional slowness (DTC), and shear slowness (DTS) following:

$$\nu = \frac{\frac{1}{2} * \left(\frac{DTS}{DTC}\right)^2 - 1}{\left(\frac{DTS}{DTC}\right)^2 - 1}$$

Dynamic Poisson's ratio values ranged from 0.27 to 0.38 with an average of 0.34 for the upper confining layer, 0.28 to 0.39 with an average of 0.37 for the lower confining layer, from 0.22 to 0.42 with an average of 0.36 in the internal confining units, and from 0.13 to 0.42 with an average of 0.33 in the injection intervals.

The dynamic Poisson's ratio measurements are frequency dependent with differences between lab and wellbore acoustic measurements driven by wavelength differences. Longer wavelength

measurements from wireline sonic logs will obtain more average property measurements and are interpreted to be more appropriate for reservoir investigations. Core based static Poisson's ratio measurements are more difficult to accurately measure, with uncertainty at 25% or higher, as cited by McPhee et al.⁴⁶ Additionally, the measurements are more localized in property identification, and are susceptible to microscopic imperfections.

Young's modulus (E), defined as applied uniaxial stress divided by normal strain, describes the stiffness of a rock and is proportional to the rock's ability to hold open a tensile fracture. Young's modulus was assessed both statically via Triax tests and dynamically, utilizing DTC, DTS, and RHOB logs. The static tests, summarized in **Table 2.5-4**, range from 0.35×10^6 to 0.5×10^6 psi in the upper confining interval, 1.33×10^6 psi in the lower confining unit, 0.98×10^6 to 1.06×10^6 psi in the internal confining units, and from 0.06×10^6 to 1.34×10^6 psi in across the injection interval.

SLB estimated dynamic Young's modulus (E_{dyn}) following:

$$E_{dyn} = 2G(1 + \nu)$$

Where G, shear modulus is derived from:

$$G = \frac{\rho_b}{DTS^2} * \alpha$$

Where ρ_b , bulk density equal to RHOB, and α , coefficient equal to 1.34×10^{10} . Dynamic Young's modulus is converted to static Young's modulus (E_{sta}) with:

$$E_{sta} = 0.032 * E_{dyn}^{1.632}$$

E_{sta} in the MEM ranges from 0.03×10^6 to 0.3×10^6 psi with an average of 0.11×10^6 psi in the upper confining interval, 0.15×10^6 to 1.04×10^6 psi with an average of 0.27×10^6 psi in the lower confining interval, 0.06×10^6 to 0.77×10^6 psi with an average of 0.26×10^6 psi, and 0.08×10^6 to 2.3×10^6 psi with an average of 0.31×10^6 psi in the injection interval.

Dynamically derived Young's modulus measurements, much like Poisson's ratio described above, are frequency dependent wireline-based measurements and will sample a larger interval than discrete core points, however the core and wireline converted E_{sta} measurements exhibit good agreement.

Generally, E is higher in the shale layers than the sands due to the unconsolidated nature of the sands, but the overall modulus value increases with depth due to compacting and increased cementation.

Tensile strength

RPS assessed the tensile strength of the confining, and injection zones where the cores were competent enough, with the Brazil Tensile strength methodology. The testing, conducted on 5 RM

⁴⁶ McPhee, C., Reed, J., Zubizarreta, I., "Core analysis: A best practice guide," *Developments in Petroleum Science* vol. 64 (2015).

testing intervals in the confining intervals and 3 in the injection intervals, is summarized in summarized in **Table 2.5-4**.

Based on the laboratory and wireline determined unconfined, confined, and tensile strength values RPS concludes that the upper confining unit possesses more than adequate strength to resist fracturing from the proposed injection and associated reservoir pressure increase.

2.5.3 Average Ductility

A key to successful sealing formations is a lack of open fractures that would enable vertical fluid migration connecting permeable beds below and above the impermeable layers. Natural fracturing, resulting from tectonic deformation, will vary in size, frequency, and level of openness depending on the mineralogic properties of the formation. Formations with high ductility tend to have lower compressive strength and can deform prior to fracturing. Ingram and Urai⁴⁷ define mudrocks as ductile if they deform without dilatancy and associated development of fracture permeability. Conversely, highly brittle formations tend to have higher compressive strength and are more likely to fracture and maintain open fractures, particularly if the fractures are oriented parallel to maximum horizontal stress ($S_{H\max}$). Formations with high clay content, particularly smectite, kaolinite, and montmorillonite, will tend to behave more ductilely and are consistent with competent sealing formations.

XRD analysis from the Palo Alto RPN-S #1 stratigraphic test well, described in **Section 2.4.3.2**, confirms a majority of clays within the confining system are smectite, and smectite-dominant mixed layer clays.

RPS evaluated the ductility of the primary confining layer through calculation of a BRI following the methodology of Ingram and Urai⁴⁸ and Dobson and Houseworth.⁴⁹ The brittleness index, BRI, is the log- unconfined compressive strength of a normally consolidated rock UCS_{NC} as

$$BRI = \frac{UCS}{UCS_{NC}}$$

$$UCS_{NC} = 0.5\sigma_{NC}$$

$$\sigma_{NC} = \rho_b g D - p_{hs}$$

$$p_{hs} = \rho_w g D$$

where σ_{NC} is the effective stress under normal compaction, ρ_b , is bulk density, g is acceleration due to gravity, D is depth, and p_{hs} is hydrostatic pressure.⁵⁰ σ_{NC} was estimated assuming bulk density = 2.1 gm/cm³, g = 9.8 meters/second², and p_{hs} = 0.457 psi/foot. The assumed bulk density for these computations was derived from the geometric mean of the overburden for the Palo Alto RPN-S #1 RHOB log. The pore pressure gradient was taken from the average of the Palo Alto

⁴⁷ Ingram and Urai, "Top-seal leakage," 1999.

⁴⁸ Ingram and Urai, "Top-seal leakage," 1999.

⁴⁹ Dobson, P. and Houseworth, J., *Inventory of shale formations in the US including geologic, hydrologic, and mechanical characteristics*, 2013, Fuel Cycle Research & Development, FCRD-UFD-2014-000513 LBNL-6633E.

⁵⁰ Dobson and Houseworth, "Inventory of shale formations," 2013.

RPN-S #1 pore pressure samples summarized in (**Table 2.5-1**). UCS was calculated as described in **Section 2.5.2**, following the relationship described by Ingram and Urai.

Following their method, Ingram and Urai concluded that $BRI < 2$ was characterized as ductile rocks that would not maintain open fractures.

Average brittleness values for the Pliocene shale are summarized in **Table 2.5-5**. The calculated brittleness values indicate the primary upper confining layer is ductile and resistant to dilatancy.

This analysis is supported by the nature and limited frequency of fracturing in the upper confining zone identified in the core and image log interpretations, described in **Section 2.3.2**. No open fractures were observed in the upper confining zone cores and the limited deformation catalogued was closed slickenside and deformation band shear features. Only four fractures were identified via the Image Log, with only 1 and a half fractures interpreted to be conductive.

2.5.4 Fractures

Minimal, isolated fracturing was observed in the Palo Alto RPN-S #1 well, as described in **Section 2.3.2**, confirming RPS's assessment that the injection and confining formations are resistant to natural fracturing. Additionally, no apparent lineaments or fracture zones were interpreted in curvature and discontinuity attribute volumes of the Smoke Bend 3D survey, suggesting that insufficient deformation exists within the AoR to focus and connect the very limited fracturing.

While observed natural fracturing was limited, RPS still conducted fracture toughness experiments to assess the critical stress intensity factor necessary to propagate existing mode 1 natural fractures at various points within the confining system. Tests were conducted on 3 samples within the Lower Pliocene shale, 1 sample in the Operc shale, and 1 sample in the Marg 'A' shale summarized in **Table 2.5-4**. The laboratory derived toughness values increase with depth most likely associated with increasing compaction and UCS. These results represent the minimum force necessary at a fracture tip to initiate further growth of existing fractures. RPS considers these values to be a conservative assessment since the tests were conducted at unconfined conditions, and the confining stresses at depth are anticipated to increase the toughness considerably.

2.5.5 In-situ Stress Field

Literature review and available seismic data (**Figure 2.2-3**) show that the RPS North Fairway sits in a normal faulting stress regime as defined by Anderson.⁵¹ In this environment, the greatest principal stress orientation, S_1 , is the vertical stress, S_V , the intermediate principal stress orientation, S_2 , is the maximum horizontal stress, S_{Hmax} , and the least principal stress orientation, S_3 , is the minimum horizontal stress, S_{hmin} . The stress of S_V is derived from the weight of the overburden, which can be determined by the equation,

$$S_V = \int_0^z \rho(z)gdz,$$

⁵¹ Anderson, E. M. (1951), *The dynamics of faulting and dike formation with application to Britain* (Edinburgh: Oliver and Boyd, 1951), 2nd Edition, 133147.

Application Number: 45054
Plan Revision: December 2025

where the sediment density ρ , can be integrated from surface to the depth of the target depth, can be multiplied by g = acceleration due to gravity, and z = depth.^{52, 53} $S_{h\min}$, is estimated following Eaton's method,⁵⁴

$$S_{h\min} = \left(\frac{\nu}{1-\nu} \right) (S_V - P_P) + P_P,$$

Where ν is Poisson's ratio, and P_P , is pore pressure. SLB calculated the S_V , and $S_{h\min}$ at the Palo Alto RPN-S #1 as part of the 1D MEM following the above-described methods where the density was integrated from surface and production section RHOB logs, the Poisson's ratio, ν , was determined calculated utilizing compressional slowness (DTC) and shear slowness (DTS) logs, and the pore pressure was calculated with a 0.457 psi/ft gradient as calibrated by the MDT pressure samples in **Table 2.5-1**.

$$\nu = \frac{\frac{1}{2} * \left(\frac{DTS}{DTC} \right)^2 - 1}{\left(\frac{DTS}{DTC} \right)^2 - 1}$$

The horizontal stress was calibrated with the fracture reopening pressure obtained from MDT mini-frac test, displayed in **Table 2.5-2**.

Based on the 1D MEM, the associated fracture pressure in the upper confining unit at the Palo Alto RPN-S #1 ranges from approximately 3,354 to 4,002 psi, translating to a fracture gradient range of 0.71 to 0.85 psi/ft, with a geometric mean of 0.80 psi/ft. This fracture pressure range enables RPS to inject at the desired injection rates and pressures without risk of fracturing the confining unit.

$S_{H\max}$, is more difficult to estimate but is constrained on the high side by S_V and on the low side by $S_{h\min}$. Investigation of the Palo Alto RPN-S #1 dipole sonic log revealed negligible separation between the fast and slow horizontal shear slowness directions suggesting minimal stress anisotropy, at least the borehole scale. Additionally, no borehole breakouts or drilling induced fractures were observed on the Image Log for $S_{H\max}$ calibration. SLB estimated $S_{H\max}$ via the poroelastic equation:

$$S_{H\max} = \frac{\nu}{1-\nu} S_V - \frac{\nu}{1-\nu} \alpha P_P + \alpha P_P + \frac{E}{1-\nu^2} \varepsilon_H + \frac{\nu E}{1-\nu^2} \varepsilon_h$$

Where α , is Biot's coefficient, E , is Youngs's modulus, ε_H , is the horizontal strain in the $S_{H\max}$ direction, and ε_h , is the horizontal strain in the $S_{h\min}$ direction. The strain terms were calibrated with the breakdown pressure observed during the mini frac (**Table 2.5-2**). The principal stress components of the MEM are displayed in **Figure 2.5-2**.

Figure 2.5-2 displays the calculated S_V , $S_{h\min}$, and pore pressure as a function of depth for the RPN project area. The area between the pore pressure line and the $S_{h\min}$ line in **Figure 2.5-2**

⁵² Zoback, Reservoir Geomechanics, 2007.

⁵³ Fjaer, E., Holt, R. et al. 2008. *Petroleum Related Rock Mechanics* (Amsterdam: Elsevier, 2008).

⁵⁴ Eaton, B. A., "Fracture gradient prediction and its application in oilfield operations," *Journal of Petroleum Technology*, vol. 246 (1969): 1353–1360.

represents the safe injection window, where the reservoir pressure is not sufficiently elevated to open or induce fracturing in the confining unit. RPS will manage rate and volume within the reservoir to not exceed 90 % of the $S_{h\min}$ at the corresponding depths within the reservoir. The corresponding fracture gradient with depth at the Palo Alto RPN-S #1 is depicted in **Figure 2.5-3**. Current simulations have assumed a fracture gradient of 0.67 psi/ft at the injection intervals.

The World Stress Map Project, as highlighted by papers such as Tingay et al.⁵⁵ and Lund-Snee and Zoback,⁵⁶ indicates that the regional $S_{h\max}$ orients parallel to the Gulf Coast margin, roughly East-West in the RPS North Fairway. These observations are consistent with the orientation of regional faulting. However, local perturbations to the stress field may exist, influenced by nearby faulting and localized changes in-bed dip azimuth. Yassir and Zerwer⁵⁷ document local variations in $S_{h\max}$ parallel to bathymetric strike in a study of borehole breakout observations, just south of the RPS North Fairway, in the northern Gulf of Mexico. Based on these observations, the present-day azimuth of $S_{h\max}$ at the AoR may be closer to 121 degrees. No apparent stress indicators were observed in the dataset to confirm or modify the local $S_{h\max}$ direction.

The estimated stress field for the confining zone is consistent with the proposed injection pressures. The orientation, magnitude, and level of stress anisotropy will impact the likelihood of slip on any faulting within the region and are accounted for in fault slip potential modeling as discussed in **Section 2.3.5**.

RPS will confirm the stress field during well construction with additional logging at the RPN-1-INJ injection well site.

2.5.6 Average Pore Pressure

The pore pressure for the upper confining layer and the entire injection interval is hydrostatically pressured. RPS demonstrated this by measuring an average pore pressure gradient of 0.457 psi/ft with the SLB MDT pressure sampling tool in the Palo Alto RPN-S #1 stratigraphic test well (**Table 2.5-1**).

Prior to measuring pore pressure directly, RPS inferred pore pressure based on literature review. An investigation by Nelson⁵⁸ of pore pressure transition across oil fields in South Louisiana indicates that the transition to overpressured formations would occur around 10,000 feet below sea level in the RPS North Fairway, which would be in the lowest portion of the injection interval (**Figure 2.5-4**). However, the datapoints used in the Nelson investigation were relatively sparse in the vicinity of the RPS North Fairway, increasing the uncertainty in the actual depth of pore

⁵⁵ Tingay, M., Müller, B., Reinecker, J. & Heidbach, O., “State and origin of the present-day stress field in sedimentary basins: New results from the World Stress Map Project,” 41st U.S. Symposium on Rock Mechanics, Golden Rocks (2006): p. 14, Published Plenary Paper ARMA/USRMS 06-1049.

⁵⁶ Lund Snee, J.-E. and M.D. Zoback, “Multiscale variations of the crustal stress field throughout North America,” *Nature Communications*, 11:1951 (2020). <https://doi.org/10.1038/s41467-020-15841-5>, www.nature.com/naturecommunications

⁵⁷ Yassir, N. A., Zerwer, A., “Stress Regimes in the Gulf Coast, Offshore Louisiana: Data from Well-Bore Breakout Analysis,” *AAPG Bulletin* vol. 81, no. 2 (1997): pp. 293–307. doi: <https://doi.org/10.1306/522B4311-1727-11D7-8645000102C1865D>

⁵⁸ Nelson, P.H., “Overpressure and hydrocarbon accumulations in Tertiary strata, gulf coast of Louisiana,” *Search and Discovery* (2012), article #41000.

pressure transition. The nearest field used by Nelson in the study, Bayou Sorrel field, indicates the pressure transition occurs at a depth of approximately 11,500 feet within the Anahuac shale, which is beneath the RPS basal confining unit (**Figure 2.5-5**).

Investigation of surrounding mud weights and drilling records, along with the work of Bray and Hanor,⁵⁹ concur that the entire reservoir and confining complex are hydrostatically pressured (**Figure 2.5-5**). Based on the hydrostatic pressure gradient of 0.457 psi/feet, the average pore pressure for the Lower Pliocene shale within the AoR is approximately 1,965 psi.

2.5.7 Addressing Geomechanical Uncertainties

Prior to providing the data acquired during site characterization activities, a degree of uncertainty existed in the geomechanical evaluation of the RPN-1-INJ confining system, because nearby third-party core and image logs were not available for analysis. RPS addressed these data gaps and reduced uncertainty through comprehensive data acquisition and testing at the Palo Alto RPN-S #1 stratigraphic test well described in **Section 2.3.4**.

Dipole sonic and density logs enabled the calculation of the dynamic Young's, shear, and bulk moduli across the confining units. Triaxial compression tests were performed at 19 distinct RM testing intervals within the injection and confining layers to determine the associated static moduli and the static to dynamic relationships for the moduli. These triaxial tests also yielded UCS measurements and Poisson's ratio at varying axial strain. Strength, compressibility, and ductility of the injection and confining layers have also been characterized through tests including uniaxial compressibility, fracture toughness, and Brazilian strength test.

RPS used the dipole sonic log, resistivity micro imager, and core to further characterize the occurrence, frequency, orientation, and cementation level of all fractures encountered in the borehole, described in **Section 2.3.2**.

Upon authorization to construct, RPS will also collect the same logging suite and collect additional core, pressure, fluid, and stress tests at the RPN-1-INJ injection well location to supplement the geomechanical assessment.

2.6 Seismic History [LAC 43:XVII.3607.C.2.c and 40 CFR 146.82(a)(3)(v)]

2.6.1 Historical Seismicity Review

RPS reviewed the United States Geologic Survey (USGS) earthquake catalogue and South Louisiana seismicity literature to collect information on historic seismicity for the RPS North Fairway. The USGS catalogue was queried for all earthquakes magnitude 0 and greater within the corner points Latitude 29.200, 31.015, Longitude -92.681, -89.506 from years 1800 to present. The seismicity review concluded that the RPS North Fairway exhibits a low level of seismic activity, with 11 seismic events (**Table 2.6-1**) of record between 1843 and 2023. The nearest event to the AoR was an estimated magnitude 4.2 on October 19, 1930, near Paincourtville (**Figure 2.6-1**). The exact event location is not well constrained because the closest seismometers to the 1930 earthquake, located at Loyola University in New Orleans and Spring Hill College in Mobile,

⁵⁹ Bray and Hanor, "Spatial variations," 1990.

Alabama, were not functioning during the quake, hence preventing an accurate location from being obtained.⁶⁰

2.6.2 Seismic Sources

Although there are numerous regional faults in Southern Louisiana (**Figure 2.1-5**), many of which are potentially active,⁶¹ slip on these faults is accommodated by aseismic creep and they are not known seismic sources.⁶² None of the 11 historic earthquake events described in **Section 2.6.1** have been definitively attributed to any of the mapped regional fault systems.⁶³ In addition, none of the mapped regional faults in Louisiana are included in the USGS Quaternary Fault and Fold Database – a national database of faults with demonstrated geologic evidence of seismic deformation occurring in the last 1.6 million years. The closest fault to the RPS North Fairway in the USGS database is the Meers Fault in Southwest Oklahoma, approximately 500 miles to the northwest.⁶⁴

Although they are not known to be seismic sources, the closest regional faults to the RPS North Fairway are described in **Table 2.1-2**.

2.6.3 Seismic Risk

No seismic sources have been identified within the RPN1 AoR. The most likely sources for naturally occurring seismic slip are along the regional normal faults depicted in **Figure 2.1-5** resulting from accumulation of differential stress or associated with shifting stresses above the nearby salt domes. RPS conducted a fault stability assessment on the surrounding faults, described in **Section 2.3.4.1**, confirming the low risk of seismicity in the AoR and great project area.

A 2018 USGS long-term national risk assessment (**Figure 2.6-2**) characterized South Louisiana as having a 2% chance of a Modified Mercalli Intensity level IV (light) earthquake within the next 50 years. RPS interprets this level of shaking to be insufficient to compromise the confining unit or any of the proposed transportation or storage infrastructure.

A USGS probabilistic assessment of earthquake occurrence indicates the South Louisiana will experience <2 damaging earthquakes in the next 10,000 years (**Figure 2.6-3**). Damaging refers to a Modified Mercalli Intensity level VI (strong). This low-risk assessment, coupled with lack of faulting within the AoR, yields a very low risk of seismic-related failure of the confining zone. Furthermore, if an earthquake were to occur within the AoR, the anticipated fault slip for a magnitude 4.2 event would be less than 1 foot, which is significantly less than the thickness of the primary confining layer. The ductile behavior of the primary confining layer, as discussed in **Section 2.5.3**, suggests any fracturing associated with an earthquake would quickly heal.

⁶⁰ Stevenson, D. A., and R. P. McCulloh, Earthquakes in Louisiana, *Louisiana Geological Survey Public Information Series No. 7* (2001).

⁶¹ McCulloh and Heinrich, “Surface faults,” 2012.

⁶² Stevenson and McCulloh, “Earthquakes in Louisiana,” 2001.

⁶³ Stevenson and McCulloh, “Earthquakes in Louisiana,” 2001.

⁶⁴ Crone, A.J., compiler, “Fault number 1031b, Meers fault, southeastern section,” in Quaternary fault and fold database of the United States: U.S. Geological Survey website (1994), <https://earthquakes.usgs.gov/hazards/qfaults>, accessed 04/11/2023 12:25 PM.

The Modified Mercalli Intensity is provided in **Figure 2.6-4**.

2.6.4 Seismicity Mitigation

While the chance of occurrence and associated impact to the region and confining interval are minimal, RPS believes that it is prudent to monitor for seismic activity and address the current limited seismic station coverage in South Louisiana. RPS's proposed induced seismic monitoring plan in **Section 9** of the Testing and Monitoring Plan details proposed monitoring station locations.

2.7 Hydrologic and Hydrogeologic Information [LAC 43:XVII.3607.C.1.b.i and 40 CFR 146.82(a)(3)(vi), 146.82(a)(5)]

2.7.1 Regional Hydrogeology

As described in **Section 2.1.4**, the AoR is located in the southeastern Louisiana hydrogeologic system along the southeastern portion of the Mississippi River Alluvial Aquifer and the southwestern portion of the Chicot Equivalent Aquifer System. Regional and site-specific hydrologic and hydrogeologic characterization was conducted through review of literature, interpretation of available shallow wireline log data, and interrogation of publicly available water chemistry data. The United States Geologic Survey "Water Resource Assessments," performed for Ascension,⁶⁵ Assumption,⁶⁶ Iberville,⁶⁷ and St James Parishes,⁶⁸ provided regional characterization of the spatial distribution, thickness, and composition of the USDWs within each respective parish. **Figure 2.2-2** shows identified existing water wells within the AoR. Wells with shallow (<1,000 feet measured depth) SP and deep resistivity logs were analyzed to determine the top of each aquifer and the base of the lowermost USDW (**Figure 2.2-26**). Methodology for determining the base of USDW is discussed in **Section 2.2.5.2**.

Additionally, groundwater chemistry analytical data, reported by the Louisiana Department of Environmental Quality, show 7 wells screened in USDWs that are located in Ascension Parish, approximately 4 miles north-northeast of the AoR (**Figure 2.7-1**). Detailed discussion of available groundwater chemistry data from USDWs is included in **Section 2.7.5**. Fluid samples were also collected from the Miocene injection units at the Palo Alto RPN-S #1 stratigraphic test well in June 2023, the results of which are reported in **Section 2.7.6**.

2.7.2 Mississippi River Alluvial Aquifer

The Mississippi River Alluvial Aquifer, the primary source of freshwater within the region, comprises paleo river deposits which lie beneath and adjacent to the Mississippi River and continue southward from the river source and eventually merge with the lowland aquifer system

⁶⁵ Griffith, J.M., and Fendick, R.B., "Water resources of Ascension Parish, Louisiana," U.S. Geological Survey Fact Sheet 2009-3063 (2009): 4 p. (Revised September 2011).

⁶⁶ Prakken, L.B., and Lovelace, J.K., "Water resources of Assumption Parish, Louisiana," U.S. Geological Survey Fact Sheet 2013-3061 (2013): 6 p., <https://pubs.usgs.gov/fs/2013/3061/>.

⁶⁷ Lindaman, M.A., and White, V.E., "Water resources of Iberville Parish, Louisiana," U.S. Geological Survey Fact Sheet 2021-3014 (2021), 6 p., <https://doi.org/10.3133/fs20213014>.

⁶⁸ White, V.E., and Prakken, L.B., "Water resources of St. James Parish, Louisiana," U.S. Geological Survey Fact Sheet 2015-3038 (2015), 6 p., <https://dx.doi.org/10.3133/fs20153038>.

near the Gulf of Mexico. The Mississippi River alluvial deposits exist in eastern Iberville Parish, western Ascension Parish, and nearly all of Assumption and St. James Parishes.

According to Griffith and Fendick, the aquifer deposits range in depth from approximately surface level to 250 feet below National Geodetic Vertical Datum of 1929 (NGVD 29) within Ascension Parish and are arranged into two hydrogeologic units. The upper confining unit composed of clay, silt, and fine sand obstructs flow of water to the lower unit composed of gravel and coarse sand. The confining unit average thickness is 20-30 feet with a maximum thickness of 60 feet. The total aquifer ranges in thickness from 25 feet to over 150 feet. Within the AoR, the top of the Mississippi River Alluvial Aquifer ranges from approximately 80 to 120 feet TVDSS (**Figure 2.7-2**).

According to Griffith and Fendick, water levels within the aquifer are roughly 12 feet above NGVD 29 but can fluctuate 10-15 feet seasonally. Reported yield from wells range from 10 to over 2,800 gallons per minute across Ascension,⁶⁹ Assumption,⁷⁰ Iberville,⁷¹ and St James Parishes.⁷²

Recharge sources for the aquifer include surface rainwater and the Mississippi River, as the aquifer is interpreted to be hydraulically connected.⁷³ Stuart et al.⁷⁴ indicate the recharge area for the aquifer is along the present day Mississippi River and extends west locally across southern Ascension, Iberville, and northern Assumption Parishes (**Figure 2.7-3**). The general direction of groundwater flow in the aquifer is south-southeast as indicated by the potentiometric map in **Figure 2.7-4**. Locally, the flow direction may be altered away from the Mississippi River due to seasonal fluctuations in river height.

2.7.3 Chicot Equivalent Aquifer System

In the Southeastern Louisiana hydrogeologic system, the aquifers equivalent to the Chicot aquifer system of southwestern Louisiana have been given individual aquifer names.⁷⁵ The aquifers which comprise the Chicot Equivalent Aquifer System are described below.

2.7.3.1 Gramercy Aquifer

The Pleistocene Gramercy aquifer is located primarily in St. James Parish, with the freshwater limits confined to the northeastern half of the parish.⁷⁶ According to Dial and Kilburn, the aquifer fines upward from a gravel and coarse sand in the lower and middle sections to fine sand at the top. The aquifer is thin or nonexistent in the northwestern areas of St. James Parish, as well as adjacent portions of Ascension, northeastern Assumption, and southern Iberville Parishes,

⁶⁹ Griffith, and Fendick, "Water resources of Ascension," 2009 (revised September 2011).

⁷⁰ Prakken and Lovelace, "Water resources of Assumption," 2013.

⁷¹ Lindaman and White, "Water resources of Iberville, 2021.

⁷² White and Prakken, "Water resources of St. James," 2015.

⁷³ Tomaszewski, D. J., *Ground-Water Resources Along the Lower Mississippi River, Southeastern Louisiana*. Water Resources Technical Report No. 69 (2003), U.S. Geological Survey and Louisiana Department of Transportation and Development.

⁷⁴ Stuart, C. G., Knochenmus, D., and McGee, B. D., *Guide to Louisiana's Ground-Water Resources*. U.S. Geological Survey Water-Resources Investigations Report 94-4085 (1994).

⁷⁵ Stuart et al., *Guide to Louisiana's Ground-water Resources*, 1994.

⁷⁶ Dial, D.C., and Kilburn, Chabot, *Ground-water resources of the Gramercy area, Louisiana*, Louisiana Department of Transportation and Development, Office of Public Works Water Resources Technical Report no. 24 (1980), 39 p.

potentially due to truncation by Mississippi River alluvium, according to the cited U.S. Geological Survey “Water Resource Assessments” by Griffith and Fendick, Prakken and Lovelace, and White and Prakken. The Gramercy formation is not interpreted to exist within the AoR.

2.7.3.2 *Norco Aquifer*

The Pleistocene Norco aquifer is the shallowest Chicot Equivalent aquifer of the Ascension Parish region and is predominantly freshwater except in the southwest portion of the Parish west of the Mississippi River.⁷⁷

Tomaszewski⁷⁸ describes the aquifer as containing fine to coarse sand and perhaps fine gravel. In northern Assumption Parish, the Norco contains only saltwater and is confined from the overlying Mississippi River Alluvial Aquifer by a 10-50-foot thick clay bed.⁷⁹ The Norco appears to transition to a saline reservoir in southern Ascension Parish (Figure 2.7-5). Across Ascension Parish, the top of the Norco is between 300 and 400 feet below NGVD 29. Norco aquifer thickness is generally 20 to 170 feet, but increases up to 250 feet near the Mississippi River. Within the AoR, subsurface mapping indicates the top of the Norco ranges from approximately 300 to 340 feet TVDSS (Figure 2.7-6).

Over 600 wells are screened in the Norco Aquifer and provide groundwater for domestic, public supply, irrigation, and industrial purposes. The freshwater contained in the aquifer has been classified as moderately hard due to the concentration of CaCO₃ according to Griffith and Fendick.

2.7.3.3 *Gonzalez-New Orleans Aquifer*

The Gonzalez-New Orleans Aquifer (Holocene-Upper Pleistocene) extends from approximately 400 to 600 feet below NGVD 29 across Ascension Parish and ranges from 150 to 300 feet thick. Griffith and Fendick report that aquifer deposits consist of very fine to medium-grained sand. Within the AoR, the top of the Gonzales-New Orleans aquifer ranges from approximately 480 to 530 feet TVDSS (Figure 2.7-7).

Over 2,500 wells have been screened in the Gonzalez-New Orleans Aquifer and provide groundwater for domestic, public supply, irrigation, and industrial purposes. The aquifer contains freshwater in the northern section of Ascension Parish while the freshwater overlies saltwater in the central section, as shown in Figure 2.7-4.⁸⁰ Freshwater samples of the aquifer are classified as soft due to the concentration of CaCO₃. Within the AoR, the aquifer is interpreted to be saline.

2.7.3.4 *1200-foot Sand Aquifer*

The Pleistocene 1200-foot sand aquifer is described as fine to medium sand by Tomaszewski. The aquifer is interpreted by Tomaszewski and Stuart et al.⁸¹ as completely saline and is not targeted for water usage within Ascension Parish. However, following the resistivity criteria discussed in Section 2.2.5.2, the 1200-foot sand is classified as an USDW in the project area. Within the AoR, the top of the 1,200-foot sand ranges from approximately 770 to 790 feet TVDSS (Figure 2.7-8).

⁷⁷ Griffith and Fendick, “Water resources of Ascension,” 2009 (revised September 2011).

⁷⁸ Tomaszewski, Ground-Water Resources, 2003.

⁷⁹ Prakken and Lovelace, “Water resources of Assumption,” 2021.

⁸⁰ Griffith and Fendick, “Water resources of Ascension,” 2009 (revised September 2011).

⁸¹ Stuart et al., Guide to Louisiana’s Ground-water Resources, 1994.

2.7.3.5 Recharge and Flow

Primary recharge of the Chicot Equivalent Aquifer System occurs in the northern part of the aquifer system along the Louisiana-Mississippi State line (**Figure 2.7-9**). Primary recharge of the aquifer system functions as rainfall, leakage from surficial sands, or leakage from underlying aquifers.^{82, 83}

The Chicot Equivalent Aquifer sands dip to the south and generally flow south-southwest as shown in **Figure 2.7-10**.

2.7.4 Surface Water Bodies

One natural surface waterbody, McCall Bayou, is located within the AoR. McCall Bayou is a small stream that drains agricultural fields in the area. McCall Bayou flows east and joins the Mississippi River less than two miles east of the AoR. Other surface waterbodies in the AoR are man-made canals that have been created to drain agricultural fields. Bayou Lafourche is southeast of the AoR boundary and flows from Donaldsonville to the Gulf of Mexico.

The Mississippi River and Bayou Lafourche are the primary sources of fresh surface water in the RPS North Fairway.⁸⁴

2.7.5 USDW Water Chemistry

USDW water chemistry data were obtained for seven wells, described in **Table 2.7-1**, approximately 4 miles northeast of the AoR (**Figure 2.7-1**). The samples were collected between April and June of 2021 from the Norco and Gonzales-New Orleans aquifers, as inferred by the respective well depths. Additionally, a regional summary of the statistical variations in water quality for Ascension Parish is provided in **Table 2.7-2**.⁸⁵

Water samples from each of the seven wells were analyzed for water quality (**Table 2.7-3**) and inorganic concentrations (**Table 2.7-4**). All wells exhibited slightly alkaline waters with pH ranging from 7.48 to 8.51. TDS ranged from 238 to 1,612.5 milligrams per liter (mg/L), chloride concentrations ranged from 7.5 to 632 mg/L, and sulfate concentrations ranged from <1 to 4.7 mg/L. Inorganic metals measured for each well were within the accepted drinking water limits. Barium, iron, and copper were detected at concentrations below their respective Drinking Water Limits (**Table 2.7-4**). Iron concentrations appear the highest in the Mississippi River Alluvial Aquifer, with medium concentrations of 18,000 micrograms per liter reported within Ascension Parish (**Table 2.7-2**).

2.7.6 Injection Zone Water Chemistry

Aqueous chemistry samples were collected from eight different depths within Miocene sandstones of the injection formation at the and eight samples were collected from the Palo Alto RPN-S #1 stratigraphic test well in June 2023 and analyzed for general water quality parameters (such as

⁸² Stuart et al., Guide to Louisiana's Ground-water Resources, 1994.

⁸³ Tomaszewski, "Water-level surface," 2011.

⁸⁴ Griffith and Fendick, "Water resources of Ascension," 2009 (revised September 2011).

⁸⁵ Griffith and Fendick, "Water resources of Ascension," 2009 (revised September 2011).

cations, anions, TDS, and pH) and trace metals. The results of these analyses are summarized in **Table 2.7-5**.

Samples from eight depths of the injection formation exhibited slightly acidic waters with pH ranging from 6.2 to 6.9. TDS was remarkably consistent, ranging from 134,400 to 141,500 milligrams per liter (mg/L), and predominantly consisted of chloride (concentrations ranged from 80,910 to 85,960 mg/L) and sodium (concentrations ranged from 48,940 to 51,820 mg/L). Calcium and magnesium concentrations were reported at approximately 2,800 and 1,000 mg/L, respectively, with the rest of the major cations and anions reported at concentrations mostly below 300 mg/L. Concentrations of inorganic metals, such as barium and strontium, did not exhibit much variability, with barium concentrations close to 100 mg/L and those of strontium close to 105 mg/L. Iron and manganese were consistently detected and ranged in concentrations from 3.6 to 19 mg/L and 0.55 and 1.1 mg/L, respectively. Additional discussion of formation water chemistry pertaining to geochemical modeling and expected geochemical interactions is provided in **Section 2.8**.

2.7.7 Additional Hydrologic Data Collection

RPS collected supplemental data for further hydrologic characterization in and around the AoR. RPS conducted a survey with landowners to obtain updated well status and sampling permission for the wells identified in **Table 2.7-6** and depicted in **Figure 2.7-11**. Where landowners provided permission to sample and wells were confirmed to be active and could be located, RPS conducted baseline sampling so that all available aquifers are sampled with azimuthal coverage around the AoR. Baseline geochemical characterization included at a minimum: dissolved CO₂, chloride (mg/L), total dissolved solids (mg/L), pH, alkalinity, specific gravity, and temperature of the fluid sample when specific gravity was measured. The process and results of this additional sampling is provided in **Appendix 2E**. Additionally, following receipt of authorization to construct and prior to authorization to inject, RPS will drill and sample three water sampling wells (RPN-1-WS1, RPN-1-WS2, and RPN-1-WS3) depicted in **Figure 2.2-2**. These wells selected for additional sampling are screened within relevant USDWs (strategically located between the RPN-1-INJ injection well and primary USDWs in population areas) and target information gaps in the existing dataset. In addition, wireline logs and fluid samples will be collected at the RPN-1-INJ injection well location.

2.8 Geochemistry [LAC 43:XVII.3607.C.2.e and 40 CFR 146.82(a)(6)]

2.8.1 Geochemical Characterization Summary

2.8.1.1 Mineralogy/Petrology

Geological characterization of the injection and confining systems are discussed in **Section 2.4**. Mineralogy and petrology of both the injection zone and the principal confining unit are discussed in detail in **Section 2.4**. An expanded discussion is provided in this section pertaining specifically to geochemical compatibility modeling efforts.

Rock core samples were collected from Palo Alto RPN-S #1 stratigraphic test well to evaluate solid phase geochemistry/mineralogy of the injection system and to inform solid-phase components of geochemical compatibility modeling. Samples were collected for analyses of mineralogy via XRD, petrographic thin section point-counting, analysis of bulk geochemistry via

X-ray fluorescence (XRF), and petrographic assessment using SEM analysis of argon ion-milled polished thin sections with backscattered electron imaging (BSE). The laboratory analytical reports for these analyses are included as **Appendix 2D**. Of these solid-phase analyses, only XRD and petrographic point-counting datasets were used to inform the solid-phase inputs for geochemical modeling.

A total of 23 point-count/XRD samples (seven point-count samples and 16 XRD samples) were analyzed from the principal confining unit, and a total of 123 point-count/XRD samples (48 point-count samples and 75 XRD samples) were analyzed from the injection zone. All samples were collected from the same stratigraphic test well (Palo Alto RPN-S #1); therefore, the mineralogical dataset cannot fully account for spatial variability in lithology, mineralogy, and geochemistry. However, the total number of mineralogical samples comprising the mineralogical dataset and geochemical model inputs is sizeable and is, therefore, able to address the depth variability. The dataset involved in geochemical modeling efforts spans a depth range of 4,421 ft MD (measured depth) at the shallowest sampling location within the principal confining unit through 11,032 ft MD at the deepest sampling location. Although samples were not collected at a regularly repeated interval, the dataset involved in geochemical modeling efforts consists of a total of 146 mineralogical samples over a vertical interval of 6,611 ft, which were collected from distinct lithologies and depth intervals over the entirety of the principal confining unit and the injection zone.

Principal Confining Unit

Mineral identification results for principal confining unit samples are provided in **Table 2.4-12**. Thin section point-count results presented in **Table 2.4-12** have been normalized to remove observed components of rock fragments and trace minerals. These components are included in the analytical reports provided in **Appendix 2D**.

Despite differences between the two datasets comprising the solid-phase geochemical model input, general trends within the injection zone XRD and point-count data are similar⁸⁶. Average mineral abundances determined from XRD and point-counting analyses are provided in **Table 2.4-12**. The XRD dataset reports a slightly greater quartz component than the point-counting dataset, and this difference is recouped primarily by the slightly greater abundance of total clay in the point-counting dataset. As discussed in **Section 2.4**, XRD analyses of the separated clay-sized fraction was completed for all XRD samples, resulting in identification of clay mineralogy. Point-counting analyses are unable to differentiate clay mineralogy apart from some petrographically distinct clay minerals such as kaolinite and chlorite; therefore, a total clay component is presented in point-counting data, which is comparable to the total abundance of the clay-sized fraction reported in XRD samples.

Mineralogical variability within principal confining unit samples is dominated primarily by quartz-clay ratios, as quartz abundances within the unit vary from 24.5% to 67.7%, and total clay abundances vary from 17.4% to 66.3%. Individual samples also contain significant carbonate components (sample 2Va contains 25.7% calcite and 14.9% siderite), although these instances of

⁸⁶ Point-count and XRD data cannot be directly compared as point-count data yields observed mineral abundances in percentages and includes pore space and lithic fragments whereas XRD data yields individual mineral abundances in weight percentages.

sizable carbonate abundances are infrequent and likely represent carbonate-cemented localities which are not representative of the unit as a whole. Generally, abundances of feldspar minerals (plagioclase and potassium feldspar), as well as abundances of carbonate minerals and pyrite, are comparable between the two datasets. The consistency between the two datasets allows for both datasets to be easily incorporated into the solid-phase component of geochemical models for the confining unit.

Injection Zone

Mineral identification results for injection zone samples are provided in **Table 2.4-11**. Thin section point-count results presented in **Table 2.4-11** have been normalized to remove observed components of rock fragments and trace minerals. These components are included in the analytical reports provided in **Appendix 2D**.

General trends within the injection zone XRD and point-count data are very similar. Both datasets indicate comparable components of quartz and feldspar minerals (plagioclase and K-feldspar). These three minerals comprise the majority of the mineral assemblage in the sampled interval. The two datasets also contain very similar average abundance values for carbonate minerals calcite, dolomite, and siderite, as well as similar abundance values for pyrite and the combined clay-sized component. The similarities of these values indicate that the two datasets align with regards to the total clay component. The consistency between the two datasets allowed for both datasets to be easily incorporated into the solid-phase component of geochemical models for the injection zone.

2.8.1.2 Aqueous Geochemistry

Formation water samples were collected from eight depth intervals within the Palo Alto RPN-S #1 stratigraphic test well to inform the aqueous component of geochemical compatibility modeling. Formation water samples were collected from the following depths (in feet [measured depth]):

- 6,355.98
- 6,762.47
- 7,577.99
- 8,326.00
- 9,163.00
- 9,801.10
- 10,189.14
- 10,914.03

The samples were collected between June 23 and June 25, 2023. Formation water samples were analyzed for a variety of chemical parameters, including major cations (calcium, magnesium, sodium, and potassium) and anions (chloride, sulfate, and alkalinity $[\text{CO}_3 + \text{HCO}_3]$), pH, resistivity, conductivity, specific gravity, total dissolved solids (TDS), and a suite of additional cations and anions (barium, copper, iron, lead, manganese, mercury, nickel, silicon, strontium, vanadium, zinc, arsenic, borate, bromide, iodide, nitrate, sulfide, and total organic carbon [TOC]).

Results of aqueous analyses which were incorporated into geochemical modeling efforts are summarized in **Table 2.7-5**.

The formation water samples were collected within the depth range associated with the injection zone. All formation water samples were collected from the Palo Alto RPN-S #1 stratigraphic test well; therefore, the dataset comprising the aqueous geochemical component of geochemical compatibility modeling does not fully address the potential spatial variability within the injection zone. However, formation water samples were collected throughout the entirety of the injection zone depth range, so the dataset addresses the potential depth variability within the unit.

Injection zone formation water samples display consistent geochemical facies regardless of sampling depth, indicating a high degree of geochemical conformity within formation waters throughout the entirety of the injection zone vertical interval. Major ion chemistry of these waters is dominated by sodium and chloride, as illustrated by the Piper diagram on **Figure 2.8-1**. The findings of the Piper diagram are consistent with and further illustrated by the Stiff diagrams on **Figure 2.8-2**. Each Stiff diagram represents the major ion chemistry for an individual sample. The shape of the diagram corresponds to the relative proportion of major cations and major anions. The general major ion chemistry of each sample can be compared across the samples by comparing the shapes of each diagram. All Stiff diagrams have nearly identical shapes, and all samples plot in a tight cluster on the Piper diagram, meaning that major ion chemistry is nearly identical across the entire depth range.

Formation water samples contained measured TDS concentrations ranging from 134,375 milligrams per liter (mg/L) to 141,526 mg/L, with an average TDS value of 138,315 mg/L and a standard deviation of 2,146 mg/L. These TDS values are very similar, providing further evidence that injection zone formation water chemistry is geochemically consistent regardless of depth. The average TDS value of injection zone formation water is classified by the United States Geological Survey (USGS) as hypersaline. Formation water pH values are consistent across the eight samples, with pH values ranging from 6.20 standard units (SU) to 6.93 SU, with a standard deviation of 0.21 SU. These pH measurements indicate that injection zone formation water chemistry is slightly acidic. High TDS concentrations measured in the formation water samples correspond to high specific gravity values for water samples. The average specific gravity of injection zone formation water samples is 1.0931 grams per cubic centimeter (g/cm³) (**Table 2.7-5**).

Sampling methodologies for each analysis are indicated in the laboratory EDD. The EDD does not indicate the presence of data qualifiers or data quality issues. Acceptable data quality was confirmed by calculating the charge imbalance error associated with each formation water sample. Charge imbalance error calculations are commonly used to assess the general data quality of natural water samples. Sampling methodology and analytical uncertainty associated with analytical methods may result in minor variations in calculated charge balance values. Charge imbalance error within +/- 10% is typically considered to be an acceptable balance, although +/- 5% is ideal for brine solutions. Calculated charge imbalance error values are provided in **Table 2.7-5**. The reported samples have a charge imbalance error below 5%, indicating that the data are of high quality. The usage of high-quality data in geochemical modeling efforts is important to minimize error and uncertainty which may otherwise be propagated due to the iterative calculations involved in the models.

Injectate Gas Composition

The composition of the gas stream for injection is anticipated to be 99.7% CO₂. Impurities are not expected to significantly interact with injection zone minerals at present concentrations and were therefore not included in model inputs.

2.8.2 Geochemical Modeling Setup

Geochemical modeling was conducted using two approaches: thermodynamic considerations only (equilibrium modeling), and thermodynamic + kinetic considerations (reaction pathway modeling), with the purpose of evaluating the reactivity of the solid-liquid-gas system following CO₂ injection. The goals of the geochemical modeling effort included the following:

- Identify geochemical reactions thermodynamically favored to occur following gas injection;
- Evaluate geochemical and mineral mass changes associated with whole-system thermodynamic equilibrium following gas injection; and
- Evaluate the magnitude of geochemical changes, mineral mass changes, and physical impacts to porosity over an operationally relevant time duration immediately following gas injection, based on kinetic mineral reaction rates.

Multiple model cases were generated to evaluate geochemical interactions expected to occur in the target injection zone and at the principal confining unit interface. Multiple pressure/temperature conditions were evaluated for both systems, described in greater detail in subsequent sections. Equilibrium modeling was conducted using the USGS software package PHREEQC (Parkhurst and Appelo, 2013), and reaction pathway modeling was conducted using Geochemist's WorkbenchTM (GWB)⁸⁷.

Mineralogical data spanning the entire depth ranges of the target injection zone and the principal confining unit, and aqueous geochemical data collected from the entire depth range of the target injection zone, were evaluated to characterize geochemistry and inform the geochemical compatibility modeling of injectate gas with the system.

2.8.2.1 Mineralogy Model Input

The target injection zone consists primarily of subarkose, quartzarenite, and sublitharenite sandstones comprised of mostly quartz and feldspar minerals (plagioclase and K-feldspar) with variable clay components, some carbonate cement and grains (calcite, dolomite, and siderite), and small amounts of pyrite, barite, and halite (**Table 2.8-1**). Although most injection zone samples are quartz-dominant sandstones, numerous samples of the injection zone were found to contain more than 50% clay minerals. These zones include local baffles and internal confining layers described in **Section 2.4.1.2**. Of the 123 mineralogical samples analyzed from the injection zone, 13 samples were found to consist of more than 50% clay minerals (eight XRD samples and five point-count samples). Due to the variability in quartz-clay abundances within injection zone, the samples were separated into distinct mineralogical inputs during geochemical modeling to evaluate geochemical interactions in both sandstone-dominated and shale-dominated components. Injection zone mineralogy samples were separated into two groups: greater than 50% total clay component

⁸⁷ Bethke, C.M., 1998. The Geochemist's Workbench Users Guide. University of Illinois.

(denoted in modeling efforts as ‘shaley’ samples) and less than 50% total clay component (‘sandy’ samples).

The principal confining unit consists primarily of quartz and clay minerals with some feldspar and small amounts of carbonate minerals and pyrite. While some degree of mineralogical variability was observed in confining unit samples, the 23 samples were averaged to generate a single representative model input to define the confining unit in geochemical modeling efforts.

Three mineralogical inputs were prepared for use in model runs: principal confining unit, injection zone sandy lithology, and injection zone shaley lithology. Mineralogical inputs for each of the three groups were generated by calculating the mean abundances of each mineral from the XRD and point-counting datasets. Point-count mineral abundance averages were normalized to 100% to remove the contributions of lithic fragments and trace minerals. XRD samples were analyzed for clay mineralogy and, thus, individual clay mineral abundances were directly averaged. In contrast, point-count samples reported a total clay component, a kaolinite component, and a chlorite component. The kaolinite and chlorite components were directly averaged. Since both kaolinite and chlorite are clay minerals, average abundances of these minerals were subtracted from the average total clay component, and the resulting value represents the sum of illite, smectite, and mixed-layer illite/smectite (I/S). The average percentage of smectite in I/S was measured in XRD samples (**Appendix 2D**) and was found to be approximately 85% smectite and 15% illite. This ratio was applied to XRD data to calculate a smectite:illite ratio for each model group which was then applied to define the total clay component of point-count results. The average mineral compositions from both XRD and point counting analyses were then weighted for the number of samples and normalized to 100%.

Total mineral abundance values were then converted to units of moles per liter using a total bulk density value of 2.64 g/cm³ for injection zone samples and 2.43 g/cm³ for principal confining unit samples based on laboratory density testing (**Appendix 2F**). This process resulted in one mineral assemblage for use in geochemical modeling for each of the three model input groups. These inputs are provided in **Table 2.8-1**.

2.8.2.2 Aqueous Model Input

Eight formation water samples were collected from the injection zone of Palo Alto RPN-S #1 stratigraphic test well, as described in **Section 2.8-1**. The chemical composition of each of these samples was sufficiently similar to allow one representative formation water sample to define aqueous geochemistry of the injection zone formation water in geochemical modeling efforts. The compositions of these eight samples were averaged to generate a representative sample of injection zone formation water (**Table 2.8-2**). This representative sample contained a calculated charge imbalance error of 1.32%. A charge imbalance error of +/-5% is conventionally considered high quality data for brine solutions, and thus, the representative sample was not expected to cause computational problems.

Aluminum is a necessary input parameter for geochemical modeling of aluminosilicate minerals (feldspars and clays). No formation water sample collected from RPN-S #1 contained aluminum concentrations above the method detection limit of 0.01 mg/L. To arrive at a plausible aluminum concentration for the representative formation water composition, an equilibrium model run was generated in PHREEQC with aluminosilicate minerals manually set to equilibrate with the injection zone representative water sample. The aluminum component in the model output was

0.00181 mg/L, which is reasonable for a sandstone aquifer at approximately neutral pH⁸⁸. This value was used as the aluminum concentration in the representative composition.

No formation water samples were collected from the principal confining unit because of its very low permeability. The aqueous geochemical input for the principal confining unit model case was generated by equilibrating the injection zone representative formation water with the mineralogical input of the principal confining unit. This technique has been applied to estimate pore-water chemistry of argillaceous rocks in multiple academic studies⁸⁹. This equilibrium calculation was completed using PHREEQC. Results of this calculation were provided as the aqueous geochemical input for principal confining unit model runs and are provided in **Table 2.8-3**.

2.8.2.3 Additional Model Considerations

Geochemical model runs were set up using the previously described inputs for formation water and mineralogy. A representative total porosity value of 31.6% (based on total porosity values obtained through routine core analyses of the injection zone samples, **Appendix 2F**) was used to define injection zone pore space (effective porosity) in injection zone sandy and shaley lithologies model cases. A representative effective porosity value of 1.20% (based on nuclear magnetic resonance analyses; **Appendix 2F**) was used to define principal confining unit pore space in principal confining unit model cases.

The target injection zone spans a depth range of approximately 6,610 ft. This depth range is associated with a range of pressure and temperature conditions. Injection zone model runs were evaluated at pressure/temperature conditions associated with the principal confining unit/injection zone interface (believed to occur at approximately 4,500 ft MD) and the deepest depth of the injection zone unit for which reservoir condition pressure/temperature data was available (10,914 ft MD). These depths are associated with the following conditions:

- Approximate injection zone/principal confining unit interface: 4,500 ft MD, 2025.34 pounds per square inch (psi), and 122.81°F.
- Base of injection zone: 10,914 ft MD, 4,996.98 psi, and 181°F.

Geochemical model runs for injection zone sandy and shaley lithologies were completed under both sets of pressure/temperature conditions (referred to as ‘shallow’ and ‘deep’ conditions). In total, five model runs were completed under current reservoir (base) conditions: principal confining unit, shallow injection zone sandy lithology, shallow injection zone shaley lithology, deep injection zone sandy lithology, and deep injection zone shaley lithology.

In all models, the reservoir-injectate-fluid system was modeled as one cubic meter of rock fully saturated with brine in the defined effective pore space. The dynamic CO₂ plume model predicts a 69% maximum gas saturation within the reservoir and no CO₂ (0% saturation) at the top of the injection zone below the upper confining layer. The same 69% maximum gas saturation is assumed in the geochemical model. This saturation value was incorporated into calculations using the ideal

⁸⁸ Oehman, L., 1988. Equilibrium and structural studies of silicon (IV) and aluminum (III) in aqueous solution. 17 stable and metastable complexes in the system H⁺-Al³⁺-Citric acid: Inorganic Chemistry, v.27, p.2565-2570.

⁸⁹ Gaus, I., Azaroual, M., and Czernichowski-Lauriol, I., 2005. Reactive transport modelling of the impact of CO₂ injection on the clayey cap rock at Sleipner (North Sea): Chemical Geology, v.217, p.319-337.

gas law to calculate the number of moles of CO₂ and O₂ introduced to the modeled systems (**Table 2.8-4**). These values were supplied as model inputs, and CO₂ solubility within formation water was calculated in both modeling software programs based on temperature, pressure, and compositional inputs using a Henry's Law approach^{90,91,92}.

Following methods proposed in Tremosa et al.⁹³ for modeling geochemical compatibility of geologic carbon sequestration, geochemical modeling efforts employed a batch reactor modeling approach where the geochemical system comprised of minerals, formation water, and injectate gas is assumed to be a perfectly mixed reactor with homogenous distribution of every chemical compound and reactant.

Geochemical modeling software packages use databases of laboratory-generated thermodynamic data to calculate mineral solubility relative to aqueous solutions. The Lawrence-Livermore National Laboratory (LLNL) thermodynamic database was used in the geochemical model to best represent RPS's storage complex with regards to mineralogy and pressure/temperature conditions. The LLNL database contains the most robust assemblage of thermodynamic information for the mineral system comprising the injection zone and was, therefore, used for this evaluation. The LLNL database contains thermodynamic information at pressure/temperature conditions applicable to RPS system for all minerals which were included in the geochemical modeling effort. The Pitzer database was also considered based on the observed TDS concentrations of the water, but this database did not contain thermodynamic information on many of the minerals observed in large abundances in the system, such as all aluminosilicate minerals (feldspars and clay minerals), barite, siderite, and pyrite. Selecting the LLNL database instead of the Pitzer database represents a source of potential uncertainty in modeling calculations associated with the deviation in ion behavior from dilute conditions with increasing ion activity; however, this uncertainty is expected to be outweighed by the potential impact of excluding many relevant minerals from modeling, as would be required by usage of the Pitzer database.

For certain groups of closely related minerals, a mineral species required specification in the model: albite, chamosite-7A, and smectite (high-Fe,Mg) were the mineral species chosen from the plagioclase, chlorite, and smectite groups, respectively. Albite was selected to best represent the plagioclase feldspar mineral group based on the expected dominant mineralogy of the geologic provenance, as XRD and point-count evaluations did not specify the exact distribution of plagioclase feldspar variants. Chamosite-7A was selected as the closest approximation to chlorite in the LLNL database. High-Fe,Mg smectite was selected as the smectite composition used in modeling efforts to ensure that iron (Fe) and magnesium (Mg) were incorporated into a clay phase. The respective mineral formulas for all model input minerals are provided in **Table 2.8-1**.

⁹⁰ Bethke, C.M., 1998. The Geochemist's Workbench Users Guide. University of Illinois.

⁹¹ Gundogan, O., Mackay, E., and Tood, A. 2011. Comparison of numerical codes for geochemical modeling of CO₂ storage in target sandstone reservoirs: Chemical Engineering Research and Design, v.89, p.1805-1816.

⁹² Parkhurst, D.L., and Appelo, C.A.J., 2013. Description of input and examples for PHREEQC version 3: a computer program for speciation, batch-reaction, one-dimensional transport, and inverse geochemical calculations: U.S. Geological Survey Techniques and Methods, Book6, Chapter A43.

⁹³ Tremosa, J., Casillo, C., Vong, C.Q., Kervevan, C., Lassin, A., and Audigane, P. 2014. Long-term assessment of geochemical reactivity of CO₂ storage in highly saline aquifers: Applications to Ketzin, In Salah, and Snohvit storage sites: International Journal of Greenhouse Gas Control, v.20, Issue 1, p.2-26.

2.8.2.4 Equilibrium Modeling

Geochemical equilibrium calculations were completed to evaluate predicted changes in mineral masses and aqueous traits resulting from three-phase (mineralogy, formation water, injectate gas) system equilibrium. Equilibrium modeling was completed for each of the five previously defined model cases by adding mineral inputs calculated from analytical data into the model (**Table 2.8-1**) and manually fixing individual mineral saturation indices (SIs) to a value of zero in the presence of the formation water and injectate gas. A mineral SI is a conventionally used measure of mineral-water thermodynamic equilibrium specific to a particular mineral which represents the deviation between the ion activity product (IAP) and the mineral solubility product (K_{sp}), which is an analytically determined constant for each mineral at a particular pressure and temperature value. A mineral SI is calculated using the equation:

$$SI = \log_{10}\left(\frac{IAP}{K_{sp}}\right)$$

where the IAP is a calculated value which expresses how a particular concentration of that species behaves in a solution of a particular ionic strength, and the K_{sp} is defined in the thermodynamic database. Aqueous activities are conventionally considered to be equivalent to concentration values in dilute to near-dilute solutions. Activities deviate from aqueous concentrations as ionic strength increases.

If a mineral SI is greater than zero, precipitation of the mineral out of solution is thermodynamically favored. If a mineral SI is less than zero, dissolution of the existing mineral into solution is thermodynamically favored. If a mineral SI is approximately zero, then the mineral is in thermodynamic equilibrium with the solution and no precipitation/dissolution reactions are expected to occur. A mineral is functionally considered to be in thermodynamic equilibrium with pore fluid if the mineral SI is within +/- 0.2 of zero. Manually fixing the SI of a mineral to a value of zero forces chemical equilibrium within the model by forcing aqueous activity changes within the formation water, allowing changes in mineral mass and aqueous concentrations resulting from liquid-mineral-gas interactions (e.g., mineral precipitation/dissolution reactions) to be quantified.

Equilibrium modeling was completed in PHREEQC. Equilibrium model results are representative of the final equilibrated state of the system, unconstrained by mineral kinetic considerations.

2.8.2.5 Reaction Pathway Modeling

Reaction pathway modeling was completed by inputting known system components into the model and calculating the responses of mineralogy and aqueous geochemistry to the presence of the injectate gas as a function of both thermodynamic and kinetic mineral considerations over a prescribed time interval. Reaction pathway modeling was completed in React module of The Geochemists Workbench™ (GWB) software package.

As with equilibrium modeling, reaction pathway modeling assumes a batch reactor approach. Mineral reaction rate constants from Palandri and Kharaka⁹⁴ and mineral surface area values from

⁹⁴ Palandri, J.L., and Kharaka, Y.K. 2004. A compilation of rate parameters of water-mineral interaction kinetics for application to geochemical modeling. US Geological Survey Open File Report 2004-1068, 64 p.

Beckingham et al.⁹⁵ were applied to the model to assess reaction progress based on thermodynamics and precipitation/dissolution kinetics. Data for kinetic reaction rates and mineral surface areas of barite and siderite are not available in the previous references, so kinetic values from Zhen-Wu et al.⁹⁶ and Tang and Martin⁹⁷ were used for barite and siderite, respectively. Mineralogy, aqueous geochemistry, and injectate composition were provided as inputs, and the model was set to calculate resulting reactions over time based on the provided kinetic rates and mineral surface areas. Reaction pathway modeling was completed for all five model cases. Each model was set to run for an initial period of 30 years during which injectate gas was introduced into the system in units of moles at the associated pressure/temperature conditions, and a subsequent period of 50 years in which no additional gas was introduced into the system, for a total model runtime of 80 years. This model setup is intended to represent the predicted thermodynamic/kinetic reactions associated with a 30-year period of gas injection followed by a 50 year period of post-injection re-equilibration. Results of the initial 30-year runs were supplied directly as inputs to begin the subsequent 50-year runs.

2.8.2.6 Pressure/Temperature Sensitivity Assessment

Base case model input conditions were described in the above sections. These pressure/temperature conditions are associated with current reservoir conditions, which are expected to change as a result of the gas injection process. Injectate gas temperature is predicted to be 35°C at the time of injection. The continual addition of injectate into the hotter subsurface is expected to cool the surrounding injection zone, thus altering thermodynamic relationships and mineral reaction rates. The continued injection of gas into the injection zone is also expected to increase total pressure in the immediate vicinity of the injection zone. The maximum anticipated downhole pressure resulting from gas injection in the RPS project area based on injection pressure constraints is approximately 2,272 psi at the injection zone-principal confining unit interface (versus approximately 2,210 psi pre-injection), and 4,767 psi at the base of the injection zone (versus approximately 4,715 psi pre-injection).

In addition to the base case reservoir condition model runs, equilibrium and reaction pathway modeling was completed for each of the five previously described model input cases using pressure/temperature sensitivity conditions to evaluate the predicted impact of the gas injection process on geochemical interactions. All sensitivity condition model runs used 35°C as the temperature input value. Sensitivity condition model runs for the principal confining unit and the shallow portion of the injection zone used a pressure value of 3,200 psi, and model runs for the deeper portion of the injection zone used a pressure value of 5,200 psi.

⁹⁵ Beckingham, L.E., Steefel, C.I., Swift, A.M., Voltolini, M., Yang, L., Anovitz, L.M., Sheets, J.M., Cole, D.R., Kneafsey, T.J., Mitnick, E.H., Zhang, S., Landrot, G., Ajo-Franklin, J.B., DePaolo, D.J., Mito, S., and Xue, Z. 2017. Evaluation of accessible mineral surface areas for improved predictions of mineral reaction rates in porous media: *Geochem. et. Cosmo. Acta*, v.205, p.31-49.

⁹⁶ Zhen-Wu, B.Y., Dideriksen, K., Olsson, J., Raahauge, P.J., Stipp, S.L.S., and Oelkers, E.H. 2016. Experimental determination of barite dissolution and precipitation rates as a function of temperature and aqueous fluid composition: *Geochem. et. Cosmo. Acta*, v.194, p.193-210.

⁹⁷ Tang, Y., and Martin, S.T. 2011. Siderite dissolution in the presence of chromate: *Geochem. et. Cosmo. Acta*, v.75, p.4951-4962.

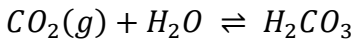
All other inputs of equilibrium and reaction pathway models were held constant for the sensitivity assessments.

2.8.3 Geochemical Modeling Results and Discussion

2.8.3.1 General Discussion of Modeling Results

Two types of geochemical models were used - 1) static equilibrium modeling including only thermodynamic considerations, and 2) reaction pathway modeling incorporating kinetic considerations in addition to thermodynamic considerations. These combined modeling approaches were used to assess expected geochemical reactions and gauge the impact of those reactions on mineral masses and aqueous geochemistry wholistically and over a time duration associated with gas injection operations. The two resulting output datasets reflect whole-system equilibrium conditions with no consideration of reaction rates (1), and geochemical reaction progress constrained by mineral kinetics (2).

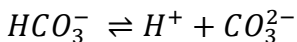
The primary mechanism driving geochemical change in the modeled systems is the dissolution of CO₂ injectate gas into formation waters. When CO₂ reacts with water, a component of the CO₂ will dissolve into the formation water until equilibrium between the two is reached. This process proceeds following the reaction below:



which yields carbonic acid. Carbonic acid in natural waters will typically dissociate into hydrogen and bicarbonate phases following the reaction:



which then may further dissociate into the carbonate species under particular geochemical conditions following the reaction:



These reactions simultaneously increase the concentrations of hydrogen ion and bicarbonate (or carbonate) in the aqueous phase (formation water). The result of these reactions is a decrease in pH and an increase in total alkalinity of the formation water, as total alkalinity consists in part of bicarbonate and carbonate concentrations. Changes in pH (decrease) and alkalinity (increase) resulting from the above reactions will alter the solubilities (and consequently, saturation indices) of minerals comprising the reservoir. These changes impact the thermodynamic stability of these minerals, which will either dissolve or precipitate out of the formation water to attempt to reach a state of thermodynamic equilibrium. Each mineral reaction further adjusts the geochemical composition of the formation water, potentially causing other minerals in the system to react in response.

These mineral reactions are constrained in their timing by kinetic reaction rates. Given an unlimited amount of time the system will continue reaction progress until whole-system equilibrium is achieved; however, the time scale of some of these reactions is on the order of geologic time (i.e., thousands to millions of years). For this reason, a gas injection system is appropriately modeled using both a thermodynamic static model setup as well as a kinetic model setup over an operational relevant time duration. Results of thermodynamic modeling alone are

Application Number: 45054
Plan Revision: December 2025

not realistic to express expected reactions/impacts resulting from injection processes over the course of operations because they represent an equilibrated end-stage of mineral reactions. Kinetic modeling alone is not appropriate to thoroughly define geochemical impacts because the reaction rates of some relevant minerals are too slow to be captured in computationally feasible model durations.

The confining unit and injection zone both contain observable quantities of carbonate minerals as cements and distinct grains. Carbonate minerals are the most sensitive to pH changes and would be expected to function as buffers to pH decreases, initially dissolving into formation water as pH levels drop. Geochemical modeling has demonstrated that calcite follows this behavior, with calcite predicted to completely dissolve in most equilibrium models, and a large decrease in calcite mass is predicted in reaction pathway models immediately following initial pH decreases. However, continual dissolution of CO₂ into formation waters also increases aqueous alkalinity concentrations. Equilibrium and reaction pathway modeling results demonstrate that formation water alkalinity concentrations increase to the point that precipitation of carbonate minerals dolomite, siderite, and in some instances, dawsonite becomes thermodynamically favorable for the confining unit and injection zone. Reaction pathway modeling results demonstrate this to a degree, as dolomite and siderite precipitation is evident within the model time duration despite the precipitation not fully offsetting the initial dissolution through 80 years. Precipitation of these minerals constitutes CO₂ mineral trapping mechanisms which, based on equilibrium modeling results, are expected to remain stable and contribute to long-term mineral mass increase and porosity decrease within all modeled systems.

The principal confining unit and injection zone are comprised dominantly of quartz. Quartz is conventionally considered a geochemically inert mineral which is not significantly reactive. Equilibrium and reaction pathway modeling predict that quartz precipitation following gas injection is ubiquitous throughout the entire injection/confining system. Equilibrium modeling results indicate that quartz precipitation accounts for the largest component of total mineral mass increase expected in injection and confining units. However, kinetic modeling results demonstrate that while quartz precipitation is ubiquitous, the kinetic reaction rates are slow, and the effects of quartz precipitation on mineral mass and total porosity are minimal over an operationally relevant time duration. Kinetic modeling results for total mineral mass changes differ from equilibrium modeling results for this reason.

Dissolution of feldspar minerals is predicted in nearly all model cases resulting from pH decreases. Dissolution is predicted in both equilibrium and reaction pathway modeling results, with feldspar dissolution expected to occur at steady rates over the kinetic model duration. Dissolution of feldspar would result in the contribution of calcium, sodium, potassium, aluminum, and silica to formation water. Equilibrium modeling results suggest that the sodium and aluminum components of dissolved feldspars likely contribute to the precipitation of dawsonite (NaAlCO₃(OH)₂), with some component of aluminum and silica likely contributing to the precipitation of kaolinite.

Feldspar alteration to dawsonite and kaolinite are both well documented processes^{98,99,100,101}. Dissolution of feldspar grains would constitute an increase of primary porosity within the injection zone and confining unit, but the associated precipitation of dawsonite and kaolinite would likely offset much, if not all, of the total mineral mass and associated porosity changes.

Illite and smectite clays are predicted to dissolve in nearly all equilibrium model cases as a result of pH decreases, with the exception of predicted illite precipitation in the injection zone shaley lithology shallow depth conditions. This tendency towards dissolution is reflected in reaction pathway results, as illite and smectite exhibit steady dissolution within the model time duration in nearly every case. Illite and smectite contain aluminum, iron, and magnesium, which likely contribute to the precipitation of carbonate minerals dolomite, siderite, and dawsonite. For this reason, equilibrium modeling predictions of total mineral mass increases are the greatest for the shaley lithology of the injection zone, as these model cases contained the greatest component of smectite and illite clays, which likely resulted in increased precipitation of carbonates. These carbonate precipitation reactions were not reflected in reaction pathway modeling results for the shaley lithology, suggesting that the reaction kinetics associated with these processes are too slow to observe within the model time duration.

Dawsonite was predicted to precipitate at notable quantities in equilibrium modeling efforts. Dawsonite reaction kinetics are the subject of active research, but kinetic considerations were not included in reaction pathway modeling for this assessment due to the underdeveloped study of the topic and lack of consensus on appropriate input values. It is likely that dawsonite precipitation will occur following gas injection based on equilibrium modeling results, but the timing of this reaction is not evaluated in the kinetic models.

Sensitivity assessments of pressure/temperature conditions were included in the modeling effort to evaluate the impact of gas injection processes on expected mineral reactions. The pressure values used in sensitivity assessments are estimations of an upper bound of pressure achievable through injection at the confining unit-injection zone interface and at the base of the injection zone, and temperature values used in the sensitivity assessments represent the temperature of injectate gas. The temperature values provide a lower bound for potentially achievable temperatures, considering burial conditions apply to the injection zone which result in base reservoir temperatures well above those of the injectate gas. The results of the sensitivity condition model runs reflect the greatest degree of expected deviation from base reservoir conditions; therefore, actual conditions and subsequent geochemical reactions expected to occur with gas injection are bounded by the base and sensitivity modeling results. As indicated in the results discussions provided above, sensitivity conditions are expected to have a limited impact on geochemical reactions over the time duration of the kinetic reaction pathway modeling (**Table 2.8-5**). A greater impact of sensitivity conditions on model results is evident in equilibrium modeling efforts (**Table**

⁹⁸ Benzeth, P., Palmer, D.A., Anovitz, L.M., and Horita, J. 2007. Dawsonite synthesis and reevaluation of its thermodynamic properties from solubility measurements: Implications for mineral trapping of CO₂. *Geochem. et. Cosmo. Act.* v.71, Issue 18, p.4438-4455.

⁹⁹ Hellevang, H., Pham, V.T.H., and Aagaard, P. 2013. Kinetic modeling of CO₂-water-rock interactions. *International Journal of Greenhouse Gas Control*, v.15, p.3-15.

¹⁰⁰ Blatt, H. 1979. Diagenetic processes in sandstones, in Scholle, P.A., and Schluger, P.R., eds., *Aspects of Diagenesis*, SEPM Special Publication 26, p.141-157.

¹⁰¹ Hurst, A., and Irwin, H. 1982. Geological modelling of clay diagenesis in sandstones. *Clay Minerals*, v.17, p.5-22.

2.8-6). Formation water pH values are influenced by sensitivity conditions for each model case, with the greatest difference between a base reservoir and sensitivity condition pH output being 0.69 SU (principal confining unit model runs). While equilibrium modeling does not have the capability to assess total porosity of the model system, results provide an assessment of total mineral mass changes associated with equilibrium. Sensitivity conditions had a limited impact on total mineral mass for the sandy lithology of the injection zone, but a notable impact on total mineral mass for the principal confining unit and the shaley lithology of the injection zone (**Table 2.8-6**).

Both types of models indicated that a set of geochemical reactions are expected to occur as a result of gas injection. These reactions are as follows:

- CO₂ dissolution into formation water;
- Carbonic acid dissociation into bicarbonate;
- Dissolution of plagioclase feldspar;
- Precipitation of barite;
- Dissolution of calcite;
- Dissolution of chlorite;
- Precipitation of dawsonite (in some model cases);
- Initial dissolution and subsequent re-precipitation of dolomite;
- Dissolution of halite;
- Precipitation or dissolution of illite;
- Precipitation or dissolution of K-feldspar;
- Precipitation or dissolution of kaolinite;
- Dissolution of pyrite;
- Precipitation of quartz;
- Initial dissolution and subsequent precipitation of siderite; and,
- Dissolution of smectite.

Full stoichiometry for each of the above listed chemical reactions are provided as **Appendix 2G**. Overall, decreases in pH values of formation water, decreases in total mass of formation water, and increases in total mineral mass are expected for both the principal confining unit and the target injection zone following interaction with injectate gas. Net mineral mass increases of 26.6 to 34.0% are predicted to occur within the confining unit based on equilibrium modeling results. Net mineral mass increases of 10.8 to 36.8% are predicted to occur within the injection zone based on equilibrium modeling. However, the majority component of the injection zone consists of sandstone, which is predicted to experience mineral mass increases of 10.8 to 12.4%. Further,

equilibrium modeling results constitute an upper bound of mineral reactivity and represent equilibrium conditions without a consideration for the timing of these reactions. All modeled increases in mineral mass are driven primarily by quartz precipitation, which is kinetically slow.

A more reasonable assessment of the impact of geochemical reactions over an operationally relevant time duration is provided by reaction pathway modeling. Reaction pathway model results indicate that porosity changes to both the principal confining unit and the target injection zone should not exceed 0.1% of total porosity (0.1% in porosity units) during the 80-year kinetic model duration. These results also support the prediction that quartz precipitation will occur and contextualize the immediate impact of the quartz precipitation as being nearly negligible in the near future.

Mineralogical and aqueous geochemical data from the Palo Alto RPN-S #1 stratigraphic test well were used to inform a series of geochemical models to evaluate the geochemical compatibility of the confining unit-injection zone system with gas injection. Results of geochemical modeling indicate that multiple geochemical/mineralogical reactions are predicted to occur, but many of these reactions are largely offsetting or kinetically slow, culminating in a predicted total porosity change of <0.1% (in porosity units) over an 80-year period. These modeling results represent a range of mineralogical and pressure/temperature conditions which are believed to provide bounds on the actual geochemical reactions. Considering assessments of porosity (effective porosity in the case of the principal confining unit and total porosity in the case of the injection zone) for the units involved in the geochemical modeling effort range from 0.2 to 3.4% for the principal confining unit and 23.6 to 38.0% for the injection zone, the maximum predicted porosity change is not considered significant enough to warrant incorporation of geochemical reactions into the AoR modeling effort.

Theoretically the low pH of the system could mobilize heavy metals. However, the degree of mobilization is difficult to quantify. XRD and SEM analyses collected in the Palo Alto RPN-S #1 did not indicate the presence of heavy metals within the injection or confining zones. The majority of heavy metals in solid phases, if present, would be contained within trace minerals at abundances less than those detectable via XRD and SEM analyses or coprecipitated with detected mineral phases at undetermined proportions. The lack of applicable solid-phase metals data renders metals mobilization modeling efforts subject to multiple assumptions which would impact the confidence of modeling results.

RPS assesses the occurrence of heavy metals at such low concentrations and likely focused in the low-permeability intervals with limited CO₂ interaction such that heavy metals mobilization will not be a concern.

2.8.3.2 Equilibrium Modeling

Predicted changes in pH of formation water, mass of formation water, and total percentage of mineral mass for all equilibrium model runs are provided in **Table 2.8-6**. Predicted mass changes to individual minerals are provided for each base reservoir pressure/temperature model run in **Tables 2.8-7** through **2.8-11**. Results for sensitivity condition model runs are provided as **Tables 2.8-12** through **2.8-16**. Changes in aqueous geochemical conditions would occur as a result of gas dissolution into formation waters and subsequent mineral precipitation/dissolution reactions which would be initiated in response to the initial geochemical changes.

Table 2.8-6 indicates predicted decreases in formation water pH for all model runs, resulting from dissolution of CO₂ into formation waters. The total mass of the formation water is predicted to decrease following equilibration of the system with injectate gas in every model case. The total mineral mass is predicted to increase in every model case, as the net precipitation of mineral mass removes aqueous components from the formation water. Under all modeled conditions for the principal confining unit and the two modeled lithologies of the injection zone, net mineral precipitation is expected. This mineral precipitation is variable, with the largest total percentage mineral mass increases expected for the shale lithology of the injection zone at sensitivity pressure/temperature conditions (34.4% and 36.8% for shallow and deep conditions, respectively), and the least net mineral precipitation predicted within the sandy lithology of the injection zone at base case reservoir pressure/temperature conditions (10.8% and 11.6% for shallow and deep conditions, respectively).

The conditions of the batch modeling approach for equilibrium modeling can lead to results that represent the upper bound of reactivity within the modeled system. Modeling results represent the upper bound because the equilibrium modeling approach assumes that pore fluids have access to the entire surface area of minerals comprising the geologic unit and reactions are allowed to proceed to thermodynamic equilibrium without time constraints. In natural systems, pore fluids have access to a much smaller mineral surface area that is limited to the pore-rock interface and is strongly influenced by pore shape, mineralogy of the interface, and pore system continuity. The limited surface area exposure in actual natural systems will both restrict and slow dissolution and precipitation rates when compared to model outputs using only thermodynamic considerations.

Principal Confining Unit Equilibrium Modeling Results

Under base case reservoir conditions, plagioclase, calcite, chlorite, illite, pyrite, and smectite are predicted to dissolve, while dawsonite, dolomite, K-feldspar, kaolinite, quartz, and siderite are predicted to precipitate. Discussion of the anticipated dissolution and precipitation timing is discussed below in **Section 2.8.3.3** with reaction pathway modeling results. Much of the predicted mineral mass changes are offsetting, as dissolved components of minerals frequently become incorporated into precipitation reactions of other minerals. The primary driver of net mineral mass gain following gas injection within the confining unit is the precipitation of quartz, which is the largest component of the confining unit's mineral assemblage.

Calcite dissolution is predicted as a result of initial carbonate buffering of pH decreases following CO₂ dissolution into formation water. CO₂ dissolution also results in an increase in aqueous alkalinity, which typically facilitates the precipitation of carbonate minerals. Carbonate minerals dolomite and siderite are predicted to precipitate in equilibrium modeling of the confining unit. Precipitation of these minerals constitute CO₂ mineral-trapping mechanisms.

Dawsonite (NaAlCO₃(OH)₂) was not reported in current mineralogical samples but is expected to precipitate following interaction with injectate gas. Dawsonite precipitation in highly saline

sandstone aquifers following carbon sequestration efforts is well studied¹⁰², and this reaction constitutes an additional CO₂ mineral-trapping mechanism.

Most of the same mineral reactions predicted in base case reservoir conditions are expected to occur within the principal confining unit under sensitivity pressure/temperature conditions. Plagioclase, calcite, chlorite, illite, K-feldspar, pyrite, and smectite are predicted to dissolve, while dawsonite, dolomite, kaolinite, quartz, siderite, and smectite are predicted to precipitate. This suite of reactions is identical to the reservoir condition model run, with the exception of K-feldspar, which is predicted to precipitate in reservoir conditions and dissolve in sensitivity conditions. While the directions of individual mineral reactions (minerals proceeding to precipitate or dissolve) are nearly identical between the two sets of pressure/temperature conditions, the magnitude of the reactions is predicted to differ slightly. The principal confining unit is predicted to experience a net mineral mass increase of 34.0% under sensitivity conditions, compared to an increase of 26.6% under reservoir conditions.

The predicted net mineral mass increase of 34.0% from sensitivity condition modeling results represents a maximum upper bound on potential mass change along the confining unit-injection zone interface. The actual observed mass gain is expected to be below this upper bound. The results of equilibrium modeling can be interpreted as wholistic final reaction progress over a timescale associated with the reaction rates of kinetically slow minerals such as quartz, which dominates the net mass change in this system. The timescale associated with achieving these upper bound results is on the order of geologic time (i.e., thousands to millions of years), rather than anthropogenic time (i.e., tens to hundreds of years). Reaction pathway modeling was completed in part to assess expected changes to mineral mass over an anthropogenic timescale.

Injection Zone (Sandy Lithology) Equilibrium Modeling Results

Under base shallow (principal confining unit-injection zone interface depth) pressure/temperature conditions, plagioclase, calcite, chlorite, halite, illite, K-feldspar, kaolinite, pyrite, and smectite are predicted to dissolve, while barite, dawsonite, dolomite, quartz, and siderite are predicted to precipitate (**Table 2.8-8**). None of these mineral reactions are predicted to differ at deeper base pressure/temperature conditions (**Table 2.8-13**). Similar to principal confining unit equilibrium modeling results, much of these mineral mass changes are offsetting. Formation water pH levels are predicted to decrease in all model cases, with shallow base condition pH predicted to be 4.40 SU, and deep base condition pH predicted to be 3.90 SU following gas interaction. The models predict decreases in formation water mass (-6.60 kg under both shallow and deep pressure/temperature conditions), and subsequent total mineral mass increases of 10.8% under shallow conditions and 11.7% under deep conditions. The primary drivers of the net mineral mass increases are quartz and dawsonite.

Calcite dissolution is predicted as a result of initial carbonate buffering of pH decreases following CO₂ dissolution into formation water. Carbonate minerals dawsonite, dolomite, and siderite are

¹⁰² Benezeth, P., Palmer, D.A., Anovitz, L.M., and Horita, J. 2007. Dawsonite synthesis and reevaluation of its thermodynamic properties from solubility measurements: Implications for mineral trapping of CO₂. *Geochem. et. Cosmo. Acta*, v.71, Issue 18, p.4438-4455.

predicted to precipitate in equilibrium modeling. Precipitation of these minerals constitutes CO₂ mineral-trapping mechanisms.

Calcite, chlorite, halite, illite, and smectite are predicted to dissolve until absent under final equilibrium conditions. The chemical components of these minerals are predicted to be incorporated into the precipitation of additional minerals mentioned above.

All mineral reactions mentioned above are expected to occur within the sandy lithology portion of the injection zone under both current reservoir conditions and sensitivity pressure/temperature conditions. The magnitude of these reactions differs between base case reservoir and sensitivity conditions. With respect to model results using base reservoir conditions, formation water pH values decreased slightly under sensitivity conditions within the shallow model case, and pH values increased slightly under sensitivity conditions within the deep model case. Across both shallow and deep conditions, formation water is predicted to experience a greater mass decrease under sensitivity conditions compared to base reservoir conditions, and an associated greater increase in net mineral mass change was predicted under sensitivity conditions (**Table 2.8-6**). The differences in net mineral mass change between base case and sensitivity conditions within the sandy lithology are relatively small (10.8% under base conditions compared to 12.4% under sensitivity conditions for the shallow model cases; 11.6% under base case conditions compared to 12.3% under sensitivity conditions for the deep model cases).

The relatively minimal difference in geochemical changes between base case reservoir and sensitivity pressure/temperature conditions indicate that predicted geochemical changes within the sandy portion of the injection zone are well-constrained. Given that the sizable majority of mineralogical samples collected from the injection zone are classified as sandy lithology samples (110 samples out of 123 collected from the injection zone), these model results represent expected geochemical reactions within the majority of the injection zone.

As mentioned above, equilibrium modeling results using only thermodynamic considerations constitute an upper bound of reactivity. Similar to geochemical modeling results for the principal confining unit, quartz comprises the largest component of net mineral mass change in this system. Quartz has slow kinetic reaction rates; therefore, the mineral mass changes predicted as upper bounds in equilibrium modeling can be interpreted as wholistic final mass change values, rather than those achievable within an anthropogenic timescale.

Injection Zone (Shale Lithology) Equilibrium Modeling Results

Within the injection zone shale lithology under base case shallow pressure/temperature conditions, plagioclase, calcite, chlorite, K-feldspar, kaolinite, pyrite, and smectite are predicted to dissolve, while barite, dawsonite, dolomite, illite, quartz, and siderite are predicted to precipitate (**Table 2.8-9**). Under base case deep pressure/temperature conditions, plagioclase, calcite, chlorite, illite, pyrite, and smectite are predicted to dissolve, while barite, dawsonite, dolomite, K-feldspar, kaolinite, quartz, and siderite are predicted to precipitate (**Table 2.8-11**). Many of these mineral reactions are offsetting, although the shale lithology of the injection zone has more predicted precipitation reactions than other model cases. Formation water pH levels are predicted to decrease in all shale injection zone model cases at internal confining zone interfaces, with shallow base case condition pH predicted to be 6.59 SU, and deep base case condition pH predicted to be 5.13 SU following gas interaction (**Table 2.8-6**). These pH decreases are less than those observed in the principal confining unit and the sandy lithology of the injection zone. The shale lithology of

the injection zone was predicted to experience a decrease in formation water mass for both shallow base case reservoir pressure/temperature conditions (-0.10 kg) and deep base case reservoir pressure/temperature conditions (-12.9 kg), which is associated with net mineral mass increases of 18.5% for shallow conditions and 25.5% for deep conditions (**Table 2.8-6**). The primary drivers of the observed mineral mass increases are quartz, dawsonite, and siderite precipitation, with siderite observed to precipitate in greater abundances than other lithologic model cases.

Calcite dissolution is predicted as a result of initial carbonate buffering of pH decreases following CO₂ dissolution into formation water. Carbonate minerals dawsonite, dolomite, and siderite are predicted to precipitate in equilibrium modeling. Precipitation of these minerals constitutes CO₂ mineral-trapping mechanisms.

Plagioclase, calcite, chlorite, and kaolinite are predicted to dissolve until absent under final equilibrium conditions for both shallow and deep base conditions, and illite is also predicted to dissolve until absent under deep base conditions. The chemical components of these minerals are predicted to be incorporated into the precipitation of additional minerals mentioned above.

The directions of each mineral reaction mentioned above are generally similar under sensitivity conditions (**Tables 2.8-9, 2.8-11, 2.8-14, and 2.8-16**). In both shallow and deep sensitivity cases, plagioclase, calcite, chlorite, illite, pyrite, and smectite are predicted to dissolve, while barite, dawsonite, dolomite, K-feldspar, kaolinite, quartz, and siderite are predicted to precipitate. Formation water pH values were predicted to decrease more than the equivalent base case model runs for both the shallow and deep depth cases. Across both shallow and deep cases, formation water experienced a greater mass decrease under sensitivity conditions compared to base case reservoir conditions, and an associated greater increase in net mineral mass change was predicted under sensitivity conditions (**Table 2.8-6**).

Net mineral mass change relative to present conditions increased the most in injection zone shaley lithology sensitivity condition model runs out of all model runs completed. This is primarily due to the significant predicted precipitation of dawsonite and siderite, two carbonate minerals whose precipitation provides mechanisms of CO₂ mineral-trapping. The prevalence of precipitation of these minerals in shaley injection zone model runs is likely associated with the relatively high abundances of smectite and illite comprising the mineralogical input. These clay minerals are predicted to dissolve completely in equilibrium modeling in most shaley lithology model runs, creating a sizeable source of aqueous sodium, aluminum, hydroxide, and iron which, when combined with alkalinity provided by CO₂ dissolution and dissociation, can facilitate the precipitation of dawsonite and siderite.

As mentioned above, equilibrium modeling results using only thermodynamic considerations constitute an upper bound of reactivity. As with all other model cases quartz comprises the largest component of the net mass change in this system. Quartz has slow kinetic reaction rates; therefore, the mineral mass changes predicted as upper bounds in equilibrium modeling can be interpreted as wholistic final mass change values, rather than those achievable within an anthropogenic timescale.

While mineral reactivity and net mineral mass changes within the shaley lithology of the injection zone were predicted to be notably greater than the sandy lithology of the injection zone, the shaley interval comprises a much smaller proportion of the injection zone (13 samples out of 123 collected

for the injection zone). This proportion, and the sporadic depths of these samples, suggests interbedded shaly laminations within a predominantly sandstone formation. Therefore, the most accurate assessment of mineral reactivity of the injection zone following gas injection achievable using the existing Palo Alto RPN-S #1 stratigraphic test well dataset is obtained by interpolating the results of the lithological end-member model cases, weighting the results of the sandy lithology modeling more heavily due to the greater number of samples.

2.8.3.3 Reaction Pathway Modeling

Kinetic reaction pathway modeling uses mineral reaction rates and mineral surface area values to constrain the progression of mineral/geochemical reactions that are determined by thermodynamics. These kinetic considerations allow for assessment of the timing of geochemical changes, and mineral surface area inputs allow for the calculation of porosity changes within the system based on the initial defined porosity and the rates of mineral precipitation/dissolution. Predicted mass changes of individual minerals for each model case at base reservoir conditions, predicted formation water pH changes for each model case at base reservoir conditions, and predicted net mineral mass changes and associated total porosity changes for each model case at base reservoir conditions are shown on **Figures 2.8-3** through **2.8-17**.

Reaction pathway modeling was also completed using sensitivity pressure/temperature conditions indicated in the above sections. Results of base reservoir and sensitivity pressure/temperature condition model runs are provided in **Table 2.8-5**.

Principal Confining Unit Reaction Pathway Modeling Results

Kinetic reaction pathway modeling results for the confining unit indicate that formation water pH is expected to decrease to 6.32 SU from 6.72 SU over the 80-year model duration, with an initial sharp decrease followed by a subsequent rapid increase prior to stabilizing (**Figure 2.8-5, Table 2.8-5**). Total mineral mass is predicted to decrease slightly, with the net mass decrease driven primarily by dissolution of the total clay mineral component as well as some dissolution of the total carbonate component (**Figure 2.8-3**). Quartz is predicted to continually precipitate at a comparatively slow rate (**Figure 2.8-3**).

Kinetic modeling of the principal confining unit under sensitivity pressure/temperature conditions yielded similar results as base reservoir conditions (**Table 2.8-5**). All mineral reaction directions (precipitation or dissolution) are predicted to remain the same in base and sensitivity conditions.

A small net mineral mass decrease is expected within the first 80 years following gas injection, associated with a small increase in porosity (by 0.003% [porosity units]). This porosity increase is likely to reverse to a net porosity decrease over a longer time duration, indicated by the steady increasing trend of quartz precipitation (**Figure 2.8-3**), as well as results from equilibrium modeling.

Injection Zone (Sandy Lithology) Reaction Pathway Modeling Results

Kinetic reaction pathway modeling results for the sandy lithology of the injection zone indicate that pH is expected to decrease from 6.72 SU to within a range of 5.60 to 6.29 SU depending on pressure/temperature condition inputs over the 80-year model duration (**Table 2.8-5**). Results from both depth conditions indicate that an initial sharp decrease in pH is expected within the first 2 years following gas injection (**Figure 2.8-8** and **2.8-14**). This pH decrease results in a decrease in calcite mass, which drives an increase in total porosity during this time period (**Figures 2.8-7** and

2.8-13). Mineral reactions proceed more gradually following this period. Total mineral mass is predicted to decrease within the sandy lithology over the model duration regardless of pressure/temperature conditions. This net mineral mass decrease is associated with a small increase in total porosity (between 0.049 and 0.054% [in porosity units] depending on pressure/temperature conditions) (**Table 2.8-5**). This mass decrease is driven by dissolution of clay and carbonate minerals. In all model cases within the sandy lithology, quartz is predicted to steadily precipitate at a comparatively slow rate.

Sandy lithology kinetic reaction pathway modeling results using sensitivity conditions are generally similar to those observed using base reservoir conditions (**Table 2.8-5**). Individual mineral reaction rates are similar throughout the model duration, as are total mineral mass, porosity, and formation water pH trends.

Porosity is expected to increase minimally (less than 0.1% [porosity units]) over the 80-year model duration within the sandy lithology. This porosity increase is driven by the faster mineral reaction kinetics associated with carbonate and clay minerals compared to quartz. Quartz remains the primary driver of equilibrium mineral mass increases, which are expected to occur over a longer time duration. This is evident from kinetic modeling efforts, as quartz is predicted to steadily precipitate at slower rates over the entire model duration (**Figures 2.8-6** and **2.8-12**). Precipitation of quartz will eventually overtake the net mineral dissolution that was observed in kinetic modeling results over the 80-year time duration.

Injection Zone (Shaley Lithology) Reaction Pathway Modeling Results

Kinetic reaction pathway modeling results of the injection zone shaley lithology indicate that formation water pH values are predicted to decrease over the 80-year model duration from 6.72 SU to a range of 5.21 to 5.88 SU depending on pressure/temperature conditions (**Table 2.8-5**). As with other model cases, results of both depth conditions indicate that a sharp pH decrease is expected immediately following gas injection (**Figures 2.8-11** and **2.8-17**). This decrease is associated with dissolution of CO₂ gas into the formation water. pH values then stabilize and gradually decrease around year 52 of the model duration. In both depth conditions, mineral mass is predicted to sharply decrease initially in response to the pH decrease, associated with dissolution of calcite (**Figures 2.8-10** and **2.8-16**). The mineral mass decreases result in initial increases in porosity. Following this initial period, total mineral mass is predicted to steadily increase over the model duration. Individual mineral trends are generally similar between shallow and deeper depth conditions (**Figures 2.8-9** and **2.8-15**).

Shaley lithology kinetic reaction pathway modeling results using sensitivity conditions are generally similar to those observed using base reservoir conditions (**Table 2.8-5**). Individual mineral reaction rates across base and sensitivity conditions are similar throughout the model duration, as are total mineral mass, porosity, and formation water pH trends.

Unlike the sandy lithology portions of the injection zone, the shaley lithology is predicted to experience a net mineral mass increase across all pressure/temperature conditions (**Table 2.8-5**). Despite this net mineral mass increase over the 80-year time duration, porosity is predicted to increase slightly (less than 0.1% [porosity units] in all model cases). The simultaneous increase in both total porosity and total mineral mass is attributable to the surface area differences of the reaction mineral assemblages. As the injection zone consists of both sandy and shaley lithologic intervals (predominantly sandstone with interbedded shale), the actual expected impact of gas

injection on the overall formation porosity and mineral mass is anticipated to be bounded by the results of the two sets of model cases. Over the 80-year kinetic modeling time duration, the predicted mineral mass decreases within the sandy lithology and increases within the shaley lithology will partially offset for the injection zone as a whole.

2.9 Other Information (Including Surface Air and/or Soil Gas Data, if Applicable)

At the time of this application, there is no potential endangerment to USDWs within the AoR; however, as a precaution, additional testing and monitoring for surface air and soil gas will be conducted in compliance with LAC 43:XVII.3625.A.8 and 40 CFR 146.90(h) to detect any potential leaks of CO₂ outside of the storage complex.

At the time of this application, no baseline data on surface air or soil gas composition has been collected. These baselines will be established at least one year before the start of injection and will inform the monitoring frequency and spatial distribution of the surface air and soil gas monitoring network for operational testing and monitoring. The testing program will be robust enough to distinguish between natural fluctuations of CO₂ and other gas/gas ratios and leakage signals within the AoR. Descriptions of the monitoring plans with specifications are given in **Attachment F**.

2.10 Site Suitability [LAC 43:XVII.3615 and 40 CFR 146.83]

The following subsections describe how the proposed injection site meets the suitability requirements set forth at LAC 43:XVII.3615 and 40 CFR 146.83, supported by references to sections of the detailed site characterization above. The findings of the site characterization demonstrate that the injection zone can accommodate the total anticipated carbon dioxide volume and that the confining zone has sufficient integrity to contain the proposed injected volume and any displaced fluids.

2.10.1 Distribution of Lithological Facies

The RPS Project targets a sand-rich Miocene sediment fairway in Southeast Louisiana for CO₂ sequestration. The target storage complex consists of stacked successions of deltaic and fluvial sands deposited from the Lower Miocene through the Early Pliocene interbedded with shale layers, which presents an appropriate setting for long-term storage of carbon dioxide. At the injection site, the stratigraphic sequence of sedimentary units consists of intermingled saline reservoirs and shale layers underlain by a basal confinement. The depth, areal extent, and thickness of the injection and confining zones have been evaluated based on available well logs from 176 wells across the region and seismic survey data, which were used to develop RPS's 3D Geomodel.

The total injection interval sediment package, from the base of the Pliocene shale, which forms the upper confining layer, to the top of the Marg. 'A' shale, which forms the basal confining layer, is approximately 6,000 feet thick with an average of 3,100 feet of net injectable sands interbedded with silts, clay, and mudstone within the North Fairway area. The gross injection interval has been subdivided into gross sand and shale packages based on regional depositional episodes and bounded by interpreted flooding surfaces. In total, the injection zone contains 11 sand packages and 10 shale packages. Within the RPS North Fairway, the thickness of the gross injection interval increases to the southwest towards the Napoleonville Dome. Within the AoR, fluctuations in sediment thickness vary from layer to layer caused by paleo-source direction and paleo-

accommodation space at the time of deposition, as well as differential compaction-related variability in net sand.

The proposed injection zone sand packages are continuous across the RPS North Fairway. Variations occur in the thickness and extent of each sand package caused by variations in local accommodation space, bed thickness, and environment of deposition, and by processes such as stacking and erosion. The primary (Pliocene shale) and basal (Marg. 'A' shale) confining units also both exhibit lateral continuity across the entire RPS North Fairway. As with the reservoir sands, local variations in accommodation space, and variations in the occurrence and continuity of individual sand beds, drive both trends and localized fluctuations in the thickness of each layer. The ten internal shale packages identified as internal baffles are interpreted to be continuous across the AoR and beyond and will aid in staged injection by sealing and compartmentalizing the injection interval at RPN-1-INJ. Detailed description of the geometry of the injection and confining zones is provided in **Sections 2.2 and 2.4**.

2.10.2 Sealing Capacity and Integrity of the Confining Zone

Key characteristics of sealing formations for successful confinement of CO₂ are large thickness, low permeability, and absence of fractures or other conduits. The primary upper confining zone (the Pliocene shale) and the basal confining zone (the Marg. 'A' shale) are expected to be suitable confining layers based on their thickness, areal extent, permeability, and resistance to fracturing. Both are continuous over the entire AoR and broadly continuous across the region. The primary confining zone ranges in thickness from 580 to 765 feet in the vicinity of the AoR, with an average thickness of 670 feet. The basal confining zone ranges in thickness from 185 to 255 feet in the vicinity of the AoR, with an average thickness of 215 feet. Detailed discussion of the geometry of the confining layers for the RPS Project is provided in **Sections 2.2 and 2.4**.

The primary upper and basal confining zones are interpreted as low permeability, low porosity claystones. Estimated porosity of the primary upper confining zone averages 22.5%, and the basal confining zone averages 18%. Estimated median permeability values in the primary confining unit and basal confining unit are 0.001 mD and 0.0088 mD respectively, which are considered to be low. Detailed discussion of the porosity and permeability of the confining zone is provided in **Section 2.4.2**.

Analysis of the shale samples from the confining units by high pressure mercury injection (HPMI) and the threshold entry pressure (TEP) testing support a conclusion that the primary upper and basal confining zones are suitable to successfully confine the injected CO₂. Mercury entry pressures from the primary upper and basal confining zones were estimated to generally range between 100 and 1,000 psi using HPMI. Based on the TEP testing, the CO₂ threshold entry pressures in the primary upper and the lower confining zones vary from 400 to > 1,000 psi and the calculated CO₂ column heights in these confining zones range from approximately 2,500 ft to >8,000 ft. Detailed discussion of the capillary entry pressures of the confining zones is provided in **Section 2.4.2.4**.

The characteristics of natural fractures in geologic materials, including frequency, size, and level of openness, are a function of the mineralogic and geomechanical properties of the formation. Formations with high ductility tend to have lower compressive strength and are able to deform without fracturing. Formations with high clay content, particularly smectite, kaolinite, and

montmorillonite will tend to behave more ductilely and are consistent with competent sealing formations. RPS evaluated the ductility of the primary confining layer by calculating the brittleness index (BRI) following the methodology of Ingram and Urai¹⁰³ and Dobson and Houseworth.¹⁰⁴ Calculated average BRI values for the primary upper confining layer in the Palo Alto RPN-S#1 ranged from 1.21 to 1.69 (see **Table 2.5-5**). Following their method, Ingram and Urai concluded that $BRI < 2$ were characterized as ductile rocks that would not maintain open fractures. The calculated brittleness values indicate the primary upper confining layer is ductile and resistant to dilatancy (see **Section 2.5.3**). This is supported by both the low compressive strength observed in the Triax tests and the presence of smectitic clays in the XRD analysis, as well as by the lack of Mode 1 fracturing observed in the Palo Alto Core and image log data (see **Section 2.3.2**). Investigation of seismic discontinuity and curvature attributes on the Smoke Bend 3D revealed no apparent faults or fracture zones across the upper confining layer within the AoR.

2.10.3 Geochemical Reactions

Expected geochemical reactions within the confining and injection units following gas injection can be evaluated using mineralogical and aqueous geochemical data collected from stratigraphic test wells combined with geochemical modeling approaches. The primary mechanism driving geochemical changes within the system is the dissolution of CO₂ injectate gas into formation waters. This reaction yields carbonic acid which will then undergo a dissociation reaction yielding aqueous bicarbonate and hydrogen. The increase in hydrogen concentrations lowers the pH of formation water. The simultaneous increase in aqueous bicarbonate and decrease in pH of formation water will alter the solubilities of the minerals comprising the reservoir and confining units which will react to attempt to achieve thermodynamic equilibrium with the new aqueous geochemical composition. These individual mineral reactions further alter the geochemical composition of the formation water, potentially triggering additional mineral reactions and subsequent changes in aqueous geochemistry. In theory, mineral-water interactions will proceed until whole-system thermodynamic equilibrium is attained. In practice, kinetic reaction rates of individual minerals will govern which reactions occur and the rate by which they proceed. These reactions can be predicted using geochemical modeling.

The full suite of geochemical reactions expected to occur following gas injection are discussed in detail in **Section 2.8**. CO₂ dissolution into formation water and subsequent dissociation to bicarbonate are predicted. These processes are predicted to trigger a suite of mineral precipitation/dissolution reactions. Generally, most feldspar minerals, most clay minerals, halite, and pyrite are predicted to dissolve, while barite, some carbonate minerals, some clay minerals, and quartz are predicted to precipitate. Carbonate minerals (calcite, dolomite, siderite, dawsonite) are predicted to initially dissolve in response to formation water pH decreases, but dolomite, siderite, and dawsonite are predicted to reprecipitate under various model conditions due to the abundance of aqueous bicarbonate provided from CO₂ dissolution. The precipitation of these minerals constitutes CO₂ mineral-trapping mechanisms.

Formation water chemistry will change depending on mineral reactions, but formation water pH levels are predicted to drop to values between 3.90 to 6.59 SU depending on lithology, aqueous

¹⁰³ Ingram and Urai, “Top-seal leakage,” 1999.

¹⁰⁴ Dobson and Houseworth, “Inventory of shale formations,” 2013.

Application Number: 45054
Plan Revision: December 2025

geochemistry, and pressure/temperature conditions. The overall brine mass is predicted to decrease in all model cases to reflect predicted net mineral mass increase. Two types of geochemical models were generated: (1) equilibrium models, which assess final thermodynamic equilibrium conditions of each modeled system given unlimited time for reactions to proceed, and (2) kinetic reaction pathway models, which evaluate geochemical reactions over an operationally relevant time duration. Equilibrium modeling efforts predict net mineral mass increases of 26.6 to 34.0% within the confining unit due to mineral precipitation (predominantly quartz) and net mineral mass increases of 10.8 to 36.8% within the injection zone due to mineral precipitation (predominantly quartz). The range of model output values accounts for variability in mineralogy and pressure/temperature conditions. Kinetic reaction pathway modeling efforts predicted that changes in total porosity of both the principal confining unit and the target injection zone should not exceed 0.1% (porosity units) during the 80-year kinetic model duration. All modeling results represent a range of mineralogical and pressure/temperature conditions, which provide bounds on geochemical conditions, including conservative assumptions intended to evaluate maximum bounds on system reactivity.

RPS believes that CO₂ injection does not pose a risk of compromising the integrity of the confining unit or adversely impacting the reservoir quality of the target injection zone because of 1) the predicted net mineral precipitation within the principal confining unit and 2) predicted minimal impacts to total porosity over operationally relevant time periods within both the principal confining unit and target injection zone. The geochemical modeling results indicate that geochemical reactions will have an insignificant impact on injection zone and confining zone performance. Therefore, RPS does not plan to integrate geochemical reactions in the reservoir flow models.

The well design parameters for RPN-1-INJ consider and include injection rates, injection volumes, fluid properties, and chemical properties of the injectate. The well is designed to withstand the corrosiveness that the injectate may have on the metallurgy of the well components, including casing, tubing wellhead equipment, and downhole tools. The design also considers the cement used in the well. The cement design and products used to cement the well are designed to fill the annulus to create good bonding between the casing and formations and withstand the corrosive nature of the injectate. Additional discussion and documentation of well design details are provided in **Section 5** and **Attachment D**.

2.10.4 Storage Capacity and Injectivity of the Injection Zone

RPS conducted reservoir characterization and numerical flow simulation of its North Fairway storage complex to assess its suitability for at least 260 MMt of CO₂ through five injection wells. Reservoir modeling results indicate that the injected CO₂ will remain trapped in the injection interval during injection and post-injection periods. Commercially available 2D and 3D seismic data, well interpretations, and relevant publications on the geologic setting of the Gulf Coast Louisiana show the Pliocene shale as a regionally extensive seal.¹⁰⁵ Low permeabilities of approximately 0.001 mD and estimated average porosity of 17.5%, along with ductile nature of

¹⁰⁵ Galloway et al., "Cenozoic depositional history," 2000.

the shale, makes the Pliocene shale a reliable seal. Hydrocarbon accumulation in this region is evidence of the Pliocene shale's sealing effectiveness.

The storage capacity of the RPS storage complex was evaluated using its detailed geologic characterization model and volumetric displacement efficiency values as described by the following equation.

$$G_{CO_2} = V_p(1 - S_{wirr})\rho E_v \quad (1)$$

V_p is the total modeled pore volume of sand-prone intervals (injection intervals) within the five AoRs of the RPS North Fairway (1.93×10^{11} ft³). S_{wirr} is the irreducible water saturation, estimated as the average minimum water saturation value (0.20) achieved in the four direct relative permeability tests described in **Section 2.4.2.2**. ρ is the CO₂ density at reservoir conditions (20.7 in kg/ft³). E_v is a volumetric displacement efficiency term that represents the combined fraction of immediate volume surrounding an injection well that can be contacted by CO₂ and fraction of net thickness that is contacted by CO₂ because of the density difference between CO₂ and in situ water. Storage capacity was calculated using both 10 percent (P10 = 0.16) and 90 percent (P90 = 0.39) probability values for volumetric displacement efficiency published by Goodman et al.¹⁰⁶. Using this method, the storage capacity of the five North Fairway AoRs (a total area of approximately 7,200 acres) is estimated to be between P10 (high confidence of exceedance): 512 MMt and P90 (low confidence of exceedance): 1,247 MMt. The large range of estimated storage capacity is due to the uncertainty in the volumetric displacement efficiency term.

RPS's site characterization and numerical modeling uses field-specific data and conservative assumptions, where applicable, to provide a better understanding of the storage capacity and containment. The simulation model is developed specifically to address the commercial design and not to solve for maximum capacity, which is to model the annual injection of 10 MMt of CO₂ through five injection wells. RPS holds additional pore space rights nearby the five proposed injection locations that RPS has not yet considered for potential development.

Seismic and log interpretation of the Miocene formation indicate that both the upper primary confining layer and the injection zone are continuous without large scale pinchouts. The numerical simulation model was developed based on the assumption of laterally continuous formation by applying pore volume multipliers gradually increasing and gradually decreasing transmissibility multipliers over four grid cells next to the grid boundary. Simulation results indicate a limited pressure buildup, mostly around the injection wells. Because of the high rock permeability at the injection interval, the injected CO₂ tends to migrate upward toward the top of the sand interval due to buoyancy effects. However, this upward migration of CO₂ is reduced by the internal shale baffles with very low permeability compared to the sand layer permeability.

Reservoir injectivity of the North Fairway storage complex is supported by the detailed geologic characterization of the Miocene Sands of the injection zone provided in **Section 2.4**. Characteristics of the proposed injection zone including areal extent, porosity, permeability, and geochemistry indicate site suitability.

¹⁰⁶ Goodman et al., A., et al., "U.S. DOE methodology," for the development of geologic storage potential for carbon dioxide at the national and regional scale", 2011. International Journal of Greenhouse Gas Control 5 (2011) 952-965

Application Number: 45054
Plan Revision: December 2025

2.10.5 Secondary Confinement

Within the RPS North Fairway there are four USDWs. The lowermost USDW, where present, is separated from the proposed primary confining layer by over 2,700 feet TVDSS as described in detail in **Section 2.2.3**. Although the thickness and integrity of the primary upper confining layer, and the vertical separation between the storage complex and the lowermost USDW, are likely sufficient to isolate the USDWs from injected CO₂, the USDWs are further isolated from the proposed injection zones by two secondary confining layers: Second Upper Confining 1 (2nd_Upper_Conf_1) and Second Upper Confining 2 (2nd_Upper_Conf_2), which provide an additional regional seal above the proposed injection zone. Further discussion of proximal USDWs is included in **Section 2.2.5**, and regional USDW details are included in **Section 2.7**.

Application Number: 45054
Plan Revision: December 2025

3. AREA OF REVIEW AND CORRECTIVE ACTION

The Area of Review and Corrective Action Plan is provided in this permit application as **Attachment B**. The Computation Modeling Approach section describes in detail how the simulation model was set up in CMG-GEM to meet the LAC 43:XVII.3615.B.3 and 40 CFR 146.84(c) requirements. RPS followed the guidelines set by the EPA to delineate the AoR to meet the LAC 43:XVII.3607.C.2.1 and LAC 43:XVII.3615.B.2 /40 CFR 146.82(a)(13) and 146.84(b). The AoR delineation is described in Computational Modeling Results and the AoR Delineation sections of the Area of Review Delineation and Corrective Action Plan.

Application Number: 45054
Plan Revision: December 2025

4. FINANCIAL RESPONSIBILITY

The Financial Responsibility Demonstration, uploaded to SharePoint as **Attachment C**, describes how River Parish Sequestration, LLC (RPS), will meet the requirements for 40 Code of Federal Regulations (CFR) 146.85 and Louisiana Administrative Code (LAC) 43.XVII.3609. The financial assurance for Class VI projects consists of four components: Corrective Action, Injection Well Plugging and Abandonment (P&A), Post-Injection Site Care (PISC) and Site Closure, and Emergency and Remedial Response Plan (ERRP). The Financial Responsibility Demonstration discusses the methodology used to determine the costs for each of the four components, the financial responsibility instrument to be used, and the frequency with which the financial assurance will be reassessed.

5. INJECTION WELL CONSTRUCTION

RPS will construct a new injection well RPN-1-INJ, one of seven new injection wells in the RPS Project and the subject of this application. The RPN-1-INJ area will include a monitoring network of four new wells, consisting of one above-confining-zone monitoring well (RPN-1-AZ), and three shallow USDW monitoring wells (RPN-1-WS1, RPN-1-WS2, and RPN-1-WS3), all within the AoR (**Figure 2.2-2**). The monitoring wells will track the CO₂ plume and pressure front evolution and help detect potential CO₂ migration out of the injection zone. Upon receipt of authorization to construct, RPS will drill and complete RPN-1-INJ with Class VI compliant material, as discussed in **Section 5.4**. Additional construction specifications for the RPN-1-INJ and the RPN-1 monitoring wells can be found in **Attachment D**. Testing and monitoring details for these wells can be found in the Testing and Monitoring Plan (**Attachment F**).

5.1 Introduction

The design, construction, and operation of injection wells fall under the jurisdiction of the Louisiana UIC Program. The Class VI injection well was established by the federal requirements under the UIC Program for Carbon Dioxide Geologic Sequestration wells (75FR 77320, December 10, 2010) and codified in the U.S. Code of Federal Regulations (40 CFR 146.81 et seq.). Class VI injection wells are designed for the sole purpose of injection and storage of CO₂ safely targeted in injection zones and contained within those zones to ensure protection of USDWs.

The requirements for both the design and the safe operation of a CCS Class VI well are described in the following sections. Summarized details for Class VI injection wells are provided in the attached well construction document (**Attachment D**).

5.2 Engineering Design

The primary concern for the design of a Class VI well is to ensure the protection of the USDW from any CO₂ injectate contamination. The design parameters for the well consider and include injection rates, injection volumes, fluid properties, and chemical properties of the injectate.

The injected CO₂ can react with brine in the injection formation to produce carbonic acid. The near-wellbore area may be a corrosive environment. The well is designed to withstand the corrosiveness that the injectate may have on the metallurgy of the well components, including casing, tubing, wellhead equipment, and downhole tools. The design also considers the cement used in the well. The cement design and products used to cement the well are designed to fill the annulus to create good bonding between the casing and formations and withstand the corrosive environment.

The well will be completed and injection will commence starting in the deepest sand interval, thereafter moving upward towards the surface. The deepest level will be perforated and injected into for two years, as described in **Attachment B**. The CO₂ plume will be monitored during and after injection to ensure that the CO₂ plume and pressure front remains in the delineated AoR. Details on monitoring are presented in **Attachment F**.

Once RPS has injected sufficient CO₂ to use the available pore space within the AoR in a given injection zone, the well will be mechanically plugged back to isolate that zone. The next sand

interval(s) above that zone will then be perforated. The injectate will then be injected and stored into that new zone until the predetermined amount of time or the adjusted time has been reached. The above process will be repeated until the uppermost injection layer below the upper confining layer is reached. Additional details regarding the operations and plugging of the well through different injection intervals are described in **Sections 7 and 9**.

The wellbore design, discussed in **Sections 5.3 and 5.4**, with specifications provided in **Attachment D**, is intended to minimize the equipment needed on location and reduce the potential damage to the wellbore during recompletion operations. This will help protect the integrity of the well and increase efficiency of zone recompletion. The design is such that the packer and tubing will not need to be pulled out of the hole and instead, once installed, will stay in place throughout the lifecycle of recompletion. The plugging of the lower zone and recompletion of the next zone will be done with a wireline unit. The design will allow for the continuous monitoring of the casing and tubing annulus to ensure wellbore mechanical integrity is maintained.

The stacked recompletions of injection intervals design may not have been contemplated during the drafting of the Class VI Guidance Documents for Class VI injection wells. The design for injection well RPN-1-INJ has been intentionally chosen by RPS for the following reasons:

- Unexpected failure of the well integrity below the tubing would fail within the confining layer or injection intervals and not the USDW, further protecting the USDW.
- Decreased risk of well malfunction as only one injection string is used as opposed to a new injection string for each injection interval.
- Fiber-optic monitoring equipment, installed along the production string, will continuously monitor structural integrity through the lifecycle of the well.
- The well design reduces the risk of damaging the tubing string by eliminating the need to remove the tubing and packer before each recompletion.

5.3 Construction Procedures [LAC 43:XVII.3607.C.2.k and 40 CFR 146.82(a)(12)]

Summarized construction procedures for RPN-1-INJ are provided below to meet the requirements of LAC 43:XVII.3607.C.2.k and 40 CFR 146.82(a)(12). Additional specifics for each component of the injection well are provided in **Section 5.4** and **Attachment D**.

A 20-inch outer diameter (OD) drive pipe will be used to maintain hole integrity during the initial drilling of the well. The drive pipe will be driven to refusal or ~200 blows per foot of advancement.

A surface casing will be set below the deepest USDW formation to protect the fresh-water aquifers during the drilling process. This casing will be cemented from total depth (2,800 feet) to surface.

The production, or long-string, casing will be set in a tapered “mono-bore” design, with a 9-5/8-inch casing set in the upper confining layer ~50 feet above the top of the injection interval. A CO₂-resistant, 9-5/8-inch x 7-inch OD crossover casing will connect the upper portion of the production casing to a lower 7-inch OD casing that will run to total depth, ~250 feet into the lower confining layer. The top of the 7-inch OD portion of the production casing will have a polished bore receptacle (PBR) just below the 9-5/8-inch x 7-inch OD crossover; a seal assembly at the base of the 7-inch OD injection tubing will be stung into the PBR. A “Scout” liner top permanent

production packer will be located ~50 feet above the seal assembly as a double barrier for the production string and injection tubing annulus.

Each casing string will be cemented from total depth of the respective string to the surface. The lower portion of the production casing, including the injection zone and upper confining layer, will be cemented with acid-resistant material (discussed in **Attachment D** and **Appendix 5A**)—total well depth to 3,606 feet true vertical depth (TVD). Portland cement will be used for the remainder of the production casing—3,606 feet TVD to the surface.

The injection tubing tieback, packer, and PBR system is designed to allow for up to 20 feet of movement by the injection tubing string. All parts of the well, including the production casing and injection tubing, are made of CO₂-resistant material to ensure cement integrity in case of CO₂/brine mixture exposure.

A fiber optic cable will be installed on the outside of the production casing to monitor the structural integrity of the casing. Distributed temperature and acoustic sensing data, along with discrete pressure data, will be collected from the injection well throughout the injection operation. This data will be used to monitor the pressure and temperature profiles along the wellbore and act as receivers for time-lapse vertical seismic profile monitoring.

A positive pressure differential valve will be imposed on the casing-tubing annulus to, along with the annulus fluid level, ensure external mechanical integrity of the tubing string.

The construction procedures for monitoring wells are similar to procedures for the injection well. The differences include perforation intervals in the appropriate zones to be monitored, and smaller outer diameter tubing will be used if the tubing inner diameter is large enough to allow running wireline logging tools and downhole sampler equipment that are planned to meet periodic monitoring requirements as required by LAC 43:XVII.3617.A.1 and 40 CFR 146.86(a)(2).

5.4 Discussion of Injection Well Design

RPS plans to inject 2 MMtpa of CO₂ annually into RPN-1-INJ. This translates to an average daily rate of 103.6 MMscf/day at standard conditions. The tubing design, including size, weight, and grade is based on the properties of the injectate, rate of injection, and injection pressures determined during the detailed reservoir modeling.

Taking into consideration calculated pipe friction losses, exit velocities, compression requirements, and economic evaluations, a tubing design sensitivity analysis was run. From detailed reservoir engineering model runs, a bottom hole injection pressure (BHP) was calculated (**Figure 5.4-1**). The data below identifies when the maximum BHP occurs during the life of the project and the resulting maximum flowing pressure at surface, and allows for the proper design of the casing, tubing, and wellhead configurations.

The chemical composition of the modeled injection stream represents the anticipated injection stream's constituents available in CMG-GEM, normalized to 100%. These constituents represent 99.9782% of the anticipated injection stream. The modeled injection stream is 99.734% CO₂, 0.021% H₂O, 0.025% N₂, 0.219% H₂, and 0.001% CH₄. The constituents in the anticipated injection stream that CMG-GEM does not have in its component library are all less than 0.01%. Additional details on the anticipated injection stream are discussed in **Section 7.2**.

Based on the inputs and model results, it was determined that a 7-inch OD tubing was the most optimal sized tubing to move the desired volumes of supercritical CO₂. Modeling also verified that the CO₂ would remain in supercritical state in the wellbore during injection.

As mentioned in the previous engineering design section (**Section 5.2**), due to the multiple recompletions that will be performed over the duration of RPN-1-INJ, a tapered 9-5/8-inch x 7-inch casing design will be used. This casing design will provide both a safe injection environment, as well as an efficient, and more economical, “mono-bore” completion design that will not require the packer and tubing to be pulled out of the hole when recompleting the new injection interval. The “mono-bore” design provides for a wireline unit to be used to complete the recompletion work. The “mono-bore” design and wireline unit used in the completion design will safely contain injected CO₂ within each injection interval and minimize risk to the USDW.

Based on appropriate bit size selection, pipe clearance considerations, and recommended annular spacing to assure proper cementing, it was determined that the following casing sizes are appropriate to accommodate the 7-inch injection tubing:

- 20-inch OD drive pipe
- 13-3/8-inch surface casing
- 9-5/8-inch x 7-inch production string

Additional details regarding each casing, and additional key design elements of the injection well, are provided in the following sections.

5.4.1 Drive Pipe

Due to the loose, unconsolidated, nature of the immediate sediments found beneath the waterline, a drive pipe will be necessary to ensure that hole integrity can be maintained during the initial drilling of the well. A 20-inch OD drive pipe will be used to accommodate this need. The 20-inch pipe will be driven to refusal by a hydraulic ram, or ~200 blows per foot of advancement.

The drive pipe size was selected to facilitate the desired bit size for drilling of the surface casing borehole. With an inner diameter (ID) of 18.73 inches, a 17.5-inch bit can be used for development of the next section of the well. Once the drive pipe is established, the inner portions of the pipe can be flushed out and evacuated to allow for drilling.

5.4.2 Surface Casing

The surface hole will be drilled with a 17.5-inch bit and casing set ~2,800 feet; the exact depth will be determined based on the USDW’s maximum depth and hole stability calculations, as assessed during installation. A string of 13-3/8-inch casing will be run and cemented with the casing being centered in the open hole via centralizers. Being centralized, the size of the annulus chosen will provide a consistent thickness of cement between casing and open hole, which will help ensure quality cement bonding and two solid barriers between the USDW formation and wellbore during the remaining drilling operations. Cement will be circulated to the surface and a top job will be provided if needed should the cement level fall after cement has been circulated to surface. After cementing, a cement bond log will be run to evaluate and verify good bonding

throughout the surface hole. Upon completing the production casing and cementing, four solid barriers will be present between the USDW formation and the wellbore.

To ensure cement returns to the surface are achieved, a 100% excess of open hole volumes are assumed.

5.4.3 Production Casing

The production casing, or long-string casing, is the final permanently cemented string of casing installed in the well. The production casing will run from surface to total depth and will be cemented back to surface. Cement details and volume calculations are detailed in **Attachment D** and **Appendix 5A**. There are six key design criteria for the long string:

- 1) A “mono-bore” tapered casing design to accommodate multiple recompletions over the life of the well.
- 2) The use of 25 chromium material from above the upper confining layer through the injection interval to total depth.
- 3) The use of fiber-optic and electric cables along the exterior of the casing.
- 4) Integration of tools, such as a galvanic crossover, stage tool, PBR, float equipment, and centralizers.
- 5) The use of acid resistant cement systems from 500 feet above the upper confining layer through the injection interval to total depth.
- 6) The use of a DV tool (staging tool) placed ~500 feet above the upper confining layer to ensure good acid resistant cement throughout the upper confining layer, plus ~500 feet above the upper confining layer. Portland cement will be used from that point to surface.

As discussed previously, the production casing will be set in a tapered design with a 9-5/8-inch casing set in the upper confining layer with a 9-5/8-inch x 7-inch crossover CO₂-resistant casing connecting the upper portion of the production string to a lower 7-inch OD portion of the production string that will run to total depth. The casing design accounts for downhole stresses and loads expected during drilling and injection with high safety factors; the lowest safety factor is 1.26 for the production casing collapse. The storage interval has a normal pressure of 0.457 psi/feet (pressure gradient) with temperatures from 102°F at the shallowest perforation, to 172°F at the deepest perforation. The 25-chromium production casing (at the injection zone) is rated to meet these temperature and pressure conditions. The 25-chromium production casing will both prevent corrosion and downhole or surface failures should any fluids enter the wellbore from the reservoir. The injectate will be considered sweet and will not be corrosive itself. Additional details of the CO₂ injectate are provided in **Section 7.2**.

The production string will be cemented with acid-resistant cement from total depth to ~500 feet above the upper confining layer to provide a good barrier across the upper confining layer and the top of the injection level. This will protect the cement in the annulus from carbonic acid damage and help prevent channeling. As a result, it will help maintain good bonding between the formation and casing, preserving well integrity and help maximize the life of the well. The second stage of the cement job will be cemented from the DV tool depth back to surface with a Portland-type

Application Number: 45054
Plan Revision: December 2025

cement. See the wellbore schematic for an illustration of the wellbore construction details (**Attachment D**).

The completion strategy for the well will be designed to start injecting at the lowest sand interval selected. The CO₂ injectate will be injected for the predetermined amount of time derived from the reservoir injection plume modeling. When that interval has reached that predetermined time (or beforehand if conditions warrant), a corrosion-resistant bridge plug will be set above the injection interval and 50 feet of acid-resistant cement will be placed on top of the bridge plug. This work will be done with a wireline unit without having to pull the packer and tubing.

The next injection zone above the zone that has been safely plugged will be perforated and now used for the injection of the CO₂ injectate. This will be an efficient and economic method for performing the work as a workover rig will not need to be used to perform the work. This process will continue to be repeated throughout the life of the well until the uppermost sand interval has completed its designated duration.

A fiber-optic wire continual monitoring system will be in place and used throughout the life of the well. The system will be able to measure and record downhole temperatures and downhole pressures in the injection interval as well as perform vertical seismic profile surveys of the CO₂ plume. This is done by running a fiber-optic and electric cable sensor package as the production string is being run into the hole; it is then cemented into place when the casing cementing job is performed. The system can monitor all the data from both zones that have been plugged with corrosion resistant bridge plugs, as well as each new injection zone that will be completed.

The engineering and design parameters for the production casing are summarized in **Attachment D** and **Appendix 5A**.

5.4.4 Centralizers

A bow-spring centralizer design for the 13-3/8-inch surface casing will be set up to protect any shallow aquifer zones, per state regulations, and ensure a continuous and uniform column of cement is present throughout the 2,800 feet of the casing's 13-3/8-inch x 17-1/2-inch annular void. The recommended centralizer locations will be as follows, for a total of 18 centralizers:

- Above the shoe joint
- Above the float collar
- Subsequent five joints of casing
- Every 4th joint (160 feet) to surface

Centralizer placement for the production casing will be designed with the installation of the fiber-optic monitoring cable in mind; clamp centralizers and eccentric centralizers, of the same alloy as the production casing, will both be used to ensure the fiber-optic cable is not damaged. The recommended procedure will be as follows:

- Use two slide-on eccentric centralizers across a two-joint shoe track. A cable clamp will be installed above the top eccentric centralizer for cable security.

- Install clamp centralizers every 160 feet, or four joints, to surface with cable detection clamps every three to four joints
- Fiber module protectors every five to six joints

5.4.5 Injection Tubing

The injection tubing will be made up of the same 7-inch casing as used in the “mono-bore” tapered 9-5/8-inch x 7-inch casing system. It will be hung from the surface to a total depth of 4,620 feet TVD and will be installed with premium connections. Injection tubing design statistics are summarized in **Attachment D**.

As previously discussed in this section, the injection tubing size was selected based on injection volumes, rates, and injectate composition. Like the production casing string, it is important to consider the injectate and the potential for a corrosive environment. Although the injectate stream is anticipated to be dry, i.e., noncorrosive, the planned design allows for the possibility of a surface upset or invasion of connate water from the reservoir. Taking into consideration the possibility of a water and CO₂ mixture leading to the presence of carbonic acid, 25 chromium material will be used for the tubing string.

5.4.6 Top Liner Packer and PBR Discussion

A PBR will be run just below the 9-5/8-inch x 7-inch casing crossover when the production casing is run. When the 7-inch injection tubing is run, there will be an anchor latch seal assembly on the bottom of the string that will sting into the PBR. This will provide a pressure seal and barrier to protect the 9-5/8-inch x 7-inch casing annulus above the 7-inch casing string. A “Scout” liner top packer will be located ~50 feet above the seal assembly as a double barrier for the production string and injection tubing annulus. This is a dual-bore retrievable packer that uses V0-rated AFLAS packer elements with a maximum temperature rating of 350°F. Once the seal assembly is stung into the PBR, the liner top packer will be set and pressure-tested, verifying there is no connection between the 9-5/8-inch x 7-inch production string annulus and the 7-inch injection string set through below the target injection zone.

Before setting the packer at 4,620' TVD, the 7" tubing x 9-5/8" casing annulus will be filled with 113 bbls of corrosion inhibited brine solution or equivalent corrosion resistant packer fluid. Pressure will be maintained and monitored on the annulus to ensure casing and packer integrity.

5.4.7 Subsurface Safety Valve

A subsurface safety valve will be installed ~500 feet TVD in the 7-inch injection tubing. This valve will be able to be operated either hydraulically or pneumatically from the surface to aid in the running of logging and recompletion tools when necessary. The valve is designed to automatically close as a fail-safe when no flow is occurring. All emergency shutdown systems shall be fail-safe. RPS shall function-test all critical systems of control and safety at least once every six months. This includes testing of alarms, test tripping of emergency shutdown valves ensuring their closure times are within design specifications, and ensuring the integrity of all electrical, pneumatic, and hydraulic circuits. Test dates and results shall be documented and be available for inspection by an agent of the Office of Conservation.

5.5 Testing and Logging During Drilling and Completion Operations

5.5.1 Coring Plan

As discussed in **Attachment E**, core samples will be collected during drilling of the well in the primary upper confining layer, the first injection interval, and the basal confining layer.

5.5.2 Logging Plan

An extensive suite of electric logs will be run in the open hole sections and in each casing string. The details of the open hole and cased hole logging plan are discussed further in **Attachment E**.

5.5.3 Formation Fluid Testing

Before setting the production casing string, formation fluid samples will be obtained by running an open-hole fluid recovery tool through the open-hole. Recovery sections will be determined based on open-hole evaluations. Two samples will be taken per section. Detailed information on the formation fluid sampling is described in **Attachment E**.

5.5.4 Step-Rate Injectivity Test

After the initial injection interval is perforated, a step-rate injectivity test will be performed. The objectives of the step-rate injectivity test include the following:

- Perform a step-rate test to identify formation fracture pressure of the injection formation.
- Observe the injectivity of the injection formation.

Additional details are provided in **Attachment E**.

5.5.4.1 Regulatory Information

Injection wells in the State of Louisiana are regulated by C&E. A Form UIC-WH1 will be submitted to the C&E Injection and Mining Division at the conclusion of all tests, along with a report that includes an in depth analysis of the step-rate fall-off tests.

5.6 Proposed Stimulation Program [LAC 43:XVII.3607.C.2.h and 40 CFR 146.82(a)(9)]

RPS has no plan to stimulate the formation by way of hydraulic fracturing in order to enhance injectivity. However, RPS will submit a stimulation plan that describes steps that RPS will take to clean up the perforation debris after the perforation process by injecting a limited volume of acid, such as HCL.

Application Number: 45054
Plan Revision: December 2025

6. PRE-OPERATIONAL LOGGING AND TESTING

The Pre-Operational Testing Plan has been submitted to SharePoint as **Attachment E**. The plan describes the schedule and the type of open-hole and cased-hole logs that RPS will take at the injection well and all the monitoring wells, to collect pre-injection data and ensure cement bond quality and casing integrity. Methods to ensure internal and external mechanical integrity of the wellbore are described. The plan meets the LAC 43:XVII.3607.C.2.g and LAC 43:XVII.3617.B / 40 CFR 146.82(a)(8) and 146.87 requirements.

7. WELL OPERATION

The well operation procedures described in this section were designed using the injection and confining zone depths, thicknesses, and permeabilities (**Sections 2.2 and 2.4**), geomechanical properties of the reservoir (**Section 2.5**), well construction details (**Section 5**), and the injection volumes and rates (**Section 2.10**). These detailed procedures are provided to describe the steps that RPS will take to operate the injection well. **Table 7-1** includes the operating pressures, average injection rates, maximum injection rate, and the casing-tubing annulus pressure while injecting. These values are calculated based on information presented in **Section 2.10** and simulation results from **Attachment B**. A minimum positive annulus pressure differential of 200 pounds per square inch gauge (psig) will be maintained at the casing-tubing annulus of the injection well, directly above and across the packer, to ensure internal well integrity. The annulus fluid level will be monitored, and any fluid volume added to the annulus to maintain the pressure differential will be recorded. Monitoring details are presented in **Attachment F**.

7.1 Operational Procedures [LAC 43:XVII.3607.C.2.j and 40 CFR 146.82(a)(10)]

The injection well is designed to deliver 2 MMtpa of CO₂ into the storage zone through multiple stages. The 7-inch production casing provides the ability to inject the design rate while maintaining the injection pressure below maximum allowable pressure. To protect the USDW, injection will be through the 7-inch longstring casing, which is separated from the USDW by the surface casing. The casing string will be compatible with CO₂, as described in **Section 5**.

The RPS well RPN-1-INJ is planned to inject 2 MMtpa of CO₂. The CO₂ will be injected and remain in the supercritical phase through the life of the project. The largest anticipated increase in BHP is 650 psi. The reservoir properties of the Miocene sands (high porosity and high permeability) allow for a pseudo-infinite acting reservoir with the ability to accept the injected CO₂ and relieve pressure quickly. Consequently, RPS will limit the amount of CO₂ injected into a given injection zone such that the CO₂ will stay within the RPS's leased pore space.

The gross injection interval is expected to be 4,326 feet to 10,499 feet TVD, with an average injection rate of 5,479 Mt per day of CO₂ (103.6 MMscf/day). The maximum expected surface injection pressure will be 2,434 psi, and the minimum tubing/casing annulus pressure will be set at 200 psi higher than the tubing pressure directly above and across the packer.

Surface injection pressures will be limited such that BHP does not exceed 90% of the fracture pressure of the injection reservoir. Proposed operating conditions, including injection rate, calculated maximum and average BHP, and calculated maximum and average WHP, is shown in **Table 7.1-1**. The maximum bottomhole pressure is considered as 90% of the formation's fracture pressure estimated from the Eaton correlation. RPS estimated the fracture pressure utilizing Eaton's method with an overburden gradient of 0.86 psi/ft and a Poisson's ratio of 0.35. These parameters were determined based on evaluation of the Palo Alto elastic logs and associated 1D Mechanical Earth Model. (**Section 2.5** Geomechanical and Petrophysical Information discusses geomechanics in detail.) Pressures will be monitored continuously, as described in **Attachment F**, to meet the requirements of LAC 43:XVII.3621.A, and 40 CFR 146.88.

To maximize use of the available pore space, multiple injection intervals will be used. There will be discrete injection intervals used for a set period, and then abandoned (**Table 7.1-2**).

At the start of injection, RPS will follow a ramp-up schedule to gradually increase the CO₂ injection rate to the design rate while checking for potential issues that may be encountered during the operation. **Table 7.1-3** shows the ramp-up schedule for each perforation interval of RPN-1-INJ. This schedule is applied only the first time each perforation interval is put on injection until it reaches the full injection rate. The injection rate is expected to vary in response to variations on CO₂ stream availability, and well and reservoir monitoring, with the maximum injection rates expected at the beginning of the operation of each injection interval. Early on, when injecting in the deeper injection zones, a booster pump may be utilized to provide the higher injection pressures of approximately 2,150 psig. However, the need for the booster pump will be temporary, and injection pressure will drop below 2,000 psig.

Typical densities for the injectate range from 43 pounds per cubic feet (lb/ft³) in the shallowest injection interval to 47 lb/ft³ in the deepest injection interval. This is compared to 68 lb/ft³ for the connate brine in the same formation. This density difference and the high vertical permeability in the Miocene sands allows the CO₂ to migrate vertically to the top of each discrete injection interval and laterally under the confining layer of that injection interval.

The result is a “tongue” effect, as shown in figures in **Attachment B**. To maximize the use of pore space, discrete injection intervals were identified, as discussed previously.

Reservoir management is integral for injection wells drilled into thick, high-permeability, unconsolidated sand formations. The operating strategy for the RPN-1-INJ is as follows:

- The gross injection interval is broken into several discrete injection intervals.
- These injection intervals are then divided into seven discrete perforated completion intervals.
- The injectate fluids are injected into the discrete completions for a relatively short period of time—not less than one year, not greater than an estimated four years.
- Plume migration surveys are conducted on a schedule detailed in **Attachment F** to contrast actual plume development with the simulated plume model.
- Once the surveyed plume has reached the model results or has caused a sufficient change to cease injection, the interval is isolated and a recompletion to the next interval is performed.
- The completed subsection is then plugged with a duplex stainless steel (or equivalent) bridge plug. The bridge plug and casing is then evaluated to ensure a proper plug.
- The abandoned subsection remains open below the bridge plug to allow for continual monitoring of bottomhole pressures and temperatures in the abandoned formations.
- This process repeats until the entirety of the gross injection interval has been completed.

Figure 7.1-1 depicts this process in a general form. The injection intervals, injection time, injection rate, and injection volume can be found in **Table 7.1-3**.

Casing and cementing design details of the injection well are provided in **Attachment F** to satisfy the LAC 43:XVII.3617, and 40 CFR 146.86 requirements.

RPS will operate the injection well within the permit limits through automated surface monitoring and visual equipment inspections to avoid or identify early signs of integrity issues, as described in **Attachment F**. RPS will install aboveground automatic shutoff valves and alarms that will be triggered by pressures beyond permitted operating limits that occur either upstream or downstream of the valves, as well as check valves to prevent flow in a direction opposite to the intended design. RPS will maintain mechanical integrity of the injection well over the life of the project, as required by LAC 43:XVII.3627, and 40 CFR 146.89.

RPS will maintain isolation of CO₂ to the permitted injection zone by means of regular subsurface monitoring and logging, as described in **Attachment F**.

If signs of integrity issues or pressures beyond permit limits occur, RPS will initiate the shutdown procedures, described in detail in **Attachment I**.

RPS will notify the UIC Director and EPA in writing 30 days in advance of any planned well workover and any planned test of the injection well conducted by RPS.

7.2 Proposed Carbon Dioxide Stream [LAC 43:XVII.3607.C.2.f.iii and 3607.C.2.f.iv, and 40 CFR 146.82(a)(7)(iii) and (iv)]

The RPS Project is a CO₂ storage hub, which means there will be multiple sources and suppliers of CO₂ that will deliver CO₂ into a co-mingled stream that will be transported from source clusters to the RPS Storage Site by the RPS Pipeline System. RPS anticipates that the sources of CO₂ will evolve and grow over the life of the RPS Project.

All suppliers of CO₂ will comply with the gas specifications of the RPS Pipeline System. The RPS Pipeline will transport CO₂ in a dense, supercritical fluid phase. Required inlet pressures must exceed 1,400 psig. **Table 7.2-1** summarizes the minimum CO₂ purity requirements. With respect to the compositional range of stream constituents RPS is willing to accept and inject, **Table 7.2-1** represents the minimum amount of CO₂ and maximum amount of other constituents.

For the purposes of this Class VI Application, RPS analyzed the chemical and physical characteristics of the CO₂ stream, including as it relates to geochemistry in **Sections 2.8 and 2.10.3, Section 5** Construction Plan and Procedures, **Section 7** Well Operation, and **Section 8** Testing and Monitoring.

RPS uses the blended CO₂ stream in **Table 7.2-2**. The proposed CO₂ stream in **Table 7.2-2** represents a blend of five CO₂ streams from CO₂ RPS's contracted supplier plus four additional CO₂ sources from whom RPS anticipates receiving CO₂. RPS blended the CO₂ streams in the Promax model. The properties of the blended CO₂ stream are in **Table 7.2-3**. The relative constituents listed on the UIC-60 are taken from the blended CO₂ stream in **Table 7.2-3**.

ProMax is a process engineering simulation software used in the chemical, petrochemical, natural gas, and refinery industries. It has been used in the engineering field for several years and is one of the preferred modeling software programs of many that are in use today.

ProMax has a built-in library of chemicals, which includes all the chemical properties for each. The software also has several thermodynamic property packages that are specific for various types

Application Number: 45054
Plan Revision: December 2025

of chemicals. When a model is set up (or built), chemicals and the thermodynamic property are selected.

In the case of mixing gas streams to create a new composite gas stream, weighted averaging is done within the software taking all the chemicals and their properties under a set of conditions; (i.e., temperature/pressure/flowrate/concentrations) to be considered in each of the incoming streams.

The software considers the concentration of each chemical in each stream and creates a new composite or mixed stream with new concentrations and properties based on the mix of all the streams.

All CO₂ sources analyzed and integrated into models in this application—both contracted and future anticipated—are high purity pre-combustion streams with CO₂ concentrations greater than 99%. RPS's conclusions about geochemical and reservoir compatibility, well material suitability, operational compatibility, and testing method appropriateness would not change if future anticipated CO₂ streams were excluded.

To the extent there are changes to the proposed CO₂ stream that would change the conclusions above, RPS will supplement:

- the geochemistry analysis;
- construction procedures and materials;
- operating procedures;
- and the Testing and Monitoring Plan.

RPS will provide these supplements prior to construction, prior to the commencement of injection, and during injection as appropriate to reflect changes to the physical or chemical contents of the proposed or actual CO₂ stream that would have a material impact on the performance of the injection reservoir, the seal, or the storage facilities. In all cases, RPS will ensure the injection stream does not violate the permit conditions.

Application Number: 45054
Plan Revision: December 2025

8. TESTING AND MONITORING

The Testing and Monitoring Plan and its Quality Assurance and Surveillance Appendix are uploaded to SharePoint as **Attachment F**. RPS has followed EPA's guidance to satisfy minimum requirements for rules LAC 43:XVII.3603.A.3 and 3625.A, and 40 CFR 146.82(a) and 40 CFR 146.90. The monitoring network for RPN-1-INJ location includes one above-confining-zone monitoring well, and three USDW monitoring wells all within the AoR to monitor and track the CO₂ plume and pressure buildup evolution with time and to detect any potential migration of CO₂ out of the injection zone.

Application Number: 45054
Plan Revision: December 2025

9. INJECTION WELL PLUGGING

The Injection Well Plugging Plan is submitted to SharePoint as **Attachment G**. RPS will take appropriate procedures and materials to plug the injection well at the end of injection. The injection well will be recompleted seven times during its injection life to deliver CO₂ into the entire Miocene injection interval. As part of each recompletion stage, a CO₂-resistant plug will be set at the top of then-existing perforations followed by perforating new sand intervals.

Application Number: 45054
Plan Revision: December 2025

10. POST-INJECTION SITE CARE (PISC) AND SITE CLOSURE

RPS has submitted its PISC and Site Closure Plan to satisfy the LAC 43:XVII.3607.C.2.p and 3633.A.1, and 40 CFR 146.82(a)(17) and 146.93(a) requirements. The PISC and Site Closure Plan are uploaded to SharePoint as **Attachment H**.

Application Number: 45054
Plan Revision: December 2025

11. EMERGENCY AND REMEDIAL RESPONSE

RPS has submitted the Emergency and Remedial Response Plan (ERR Plan) to satisfy the requirements of LAC 43:XVII.3607.C.2.r and 3623.A.1, and 40 CFR 146.82(a)(19) and 146.94(a). The Emergency and Remedial Response Plan describes actions that RPS will take to address movement of the injection fluid or formation fluid in a manner that may endanger an USDW during construction, operation, or post-injection site care periods, as well as the actions that RPS will take if evidence of a potential endangerment to an USDW is found. The ERR Plan is uploaded to SharePoint as **Attachment I**.

Application Number: 45054
Plan Revision: December 2025

12. INJECTION DEPTH WAIVER AND AQUIFER EXEMPTION EXPANSION

No injection depth waiver is submitted for this permit application. RPS intends to inject and store CO₂ in the Miocene formation between depths of 4,300 and 12,000 feet, approximately 3,000 feet below the deepest USDW. No USDWs are below the injection interval.

Application Number: 45054
Plan Revision: December 2025

13. OPTIONAL ADDITIONAL PROJECT INFORMATION [LAC 43:XVII SUBPART 1-6 AND 40 CFR 144.4]

Several federal and state laws and regulations apply to the injection well. Table 13-1 identifies the applicable permits and authorizations required for the Class VI injection well and the anticipated submittal and receipt timing for each.

EPA notes four federal laws that are of particular interest regarding applicability to the proposed project. These four laws are as follows.

The Wild and Scenic Rivers Act, 16 U.S.C. 1273 et seq.

There are no wild and scenic rivers in the RPS North Fairway, so the Wild and Scenic Rivers Act would not be applicable to the project.

The National Historic Preservation Act of 1966, 16 U.S.C. 470 et seq.

Louisiana State Historic Preservation Officer (SHPO) issued a concurrence. Cultural resources surveys have been performed for RPN-1-INJ and a report was generated and sent to the SHPO. The surveys found no presence of cultural resources at the injection well location and the SHPO concurred with the report's findings in the 3rd Quarter of 2024.

The Endangered Species Act, 16 U.S.C. 1531 et seq.

Habitat surveys have been conducted for the RPS Project to comply with the Endangered Species Act. Based on the endangered and threatened species listed in the area and the lack of impacts to suitable habitats, project facilities will not have any impacts to endangered or threatened species or critical habitats.

The Coastal Zone Management Act, 16 U.S.C. 1451 et seq.

The injection well and monitoring wells are not located in the Louisiana Coastal Zone and are not subject to the Coastal Zone Management Act.

14. OTHER INFORMATION

This section provides additional information to support the application.

14.1 Environmental Justice Assessment

EPA defines Environmental Justice (EJ) as “the fair treatment and meaningful involvement of all people regardless of race, color, national origin, or income, with respect to the development, implementation, and enforcement of laws, regulations, and policies.” This section provides an EJ assessment for the North Fairway, which includes five injection wells (RPN-1-INJ, RPN-2-INJ, RPN-3-INJ, RPN-4-INJ, and RPN-5-INJ) across portions of Ascension, Assumption, and Iberville Parishes.

14.1.1 Analysis of Communities

The North Fairway injection wells are located in portions of the following three census tracts 22005030900, 22007050100, and 22047953000.

Figure 14.1-1 shows the locations of the census tracts in relation to the North Fairway injection wells.

Disadvantaged Communities Report

The U.S. Department of Energy (DOE) had a Disadvantaged Communities Report tool (energyjustice.egs.anl.gov) that provided an assessment census tracts and whether they were considered disadvantaged communities (DACs) based upon demographic data and burden indicators. Based on the DOE’s described methodology, to be considered a DAC a census tract must rank in the 80th percentile of the cumulative sum of 36 burden indicators and have at least 30% of households classified as low-income.

Table 14.1-1 presents a summary of the evaluation from the Disadvantaged Communities Report tool and provides the top 5 DAC burden indicators for each census tract. The data indicate that two of the three census tracts (the tracts in Ascension and Assumption parishes) are both considered DACs. The Iberville Parish tract is not considered a DAC. For all three census tracts, the top burden indicator is cancer risk.

14.1.2 Project Benefits and Impacts

Development and operation of the RPS Project will have numerous socioeconomic and environmental benefits in the local communities. A complete evaluation of project benefits and impacts is presented in a separate Environmental Impact Assessment. The text below summarizes some of the benefits to address the burdens and challenges identified in the analyses provided in the previous section:

- Direct and indirect socioeconomic benefits
 - Job creation and training: new, clean-energy jobs and job training by employing local workers for construction and operations.

Application Number: 45054
Plan Revision: December 2025

- Additional local tax revenue: ad valorem taxes will be paid based on the value of the assets, and sales taxes will be paid based on value of goods and services purchased.
- Workforce education: opportunities through investment of resources in River Parishes Community College.
- Local business revenue: RPS and workers at the project will spend in the local communities.
- Protect good-paying manufacturing jobs: The low-cost CCS solution for heavy industry facility operators will give the facilities in the region a competitive advantage in a low-carbon future at the base of the cost curve for CCS.
- Removal of CO₂ from the emissions streams at industrial facilities in the area will likely decrease environmental exposures and burdens in the communities by removing other harmful air pollutants.
- Long-term and widespread reduction of CO₂ emissions will also reduce climate hazards on a large scale.

RPS has developed a Community Benefits Plan that will provide investment into the local communities to address areas of need through a Community Benefits Fund based on the amount of CO₂ injected as part of the RPS Project. An advisory board, consisting of third-party community partners, will be established to solicit and vet appropriate investment opportunities in the local communities. The advisory board will prioritize projects that have direct positive benefits for the communities in the RPS North Fairway. Examples of community needs identified by local officials and community leaders in preliminary discussions include early childhood education centers and resources, workforce development opportunities, utility payment assistance, and improvements and resources to local schools. RPS believes that the communities in the project area will materially benefit from these investments.

RPS conducted a siting study to determine the construction and operational footprint of the RPS Project facilities, and the project has been designed to limit impacts to the environment (land use, wetlands, water quality, soils, air quality, wildlife habitat, cultural resources) and limit socioeconomic impacts on the local communities. Impacts that could occur from the project include the following:

- Increased noise during construction and operations (construction noise will be limited to daytime hours and will comply with local ordinances)
- Increased traffic, particularly during construction
- Impacts to sensitive environmental resources, such as wetlands, from construction of some RPS Project facilities
- Visual impacts from aboveground facilities on the rural landscape

RPS intends to minimize and mitigate these potential impacts by taking the following measures:

- Limiting construction noise impacts to daytime hours only whenever possible

Application Number: 45054
Plan Revision: December 2025

- Conducting a traffic study to evaluate and implement ways to minimize traffic impacts
- Minimizing facility footprints in wetlands and conducting compensatory mitigation for unavoidable impacts to wetlands
- Using visual screening barriers when project facilities may impact the landscape

Additionally, RPS intends to engage in public participation efforts within the local community. This process will be designed and conducted to gather project input from the local communities and to ensure that effective mitigation measures are identified and implemented on the project. Public participation efforts will include meetings held at locations and facilities that are local, convenient, and accessible to people with disabilities, low-income and minority communities, and vulnerable populations. Additionally, RPS will use plain language and visual representations in presentations and handouts and references to its website at www.blueskyinfrastructure.com.

14.2 Recordkeeping

In accordance with the requirements of LAC 43:XVII.3629.A.6 and 40 CFR 146.91(f), RPS will retain all data collected for and in support of this Class VI permit application throughout the life of the Project and for 10 years following site closure or as otherwise requested by the UIC Director and EPA. Further recordkeeping requirements are detailed in the Testing and Monitoring Plan, AoR and Corrective Action Plan, and the Post-Injection Site Care and Site Closure Plan.

FIGURES

Figures are provided separately as individual files

TABLES

Tables are provided separately as individual files

APPENDICES

Appendices are provided separately as individual files